The Separate Identification of Intrinsic and Reflexive Joint Impedance

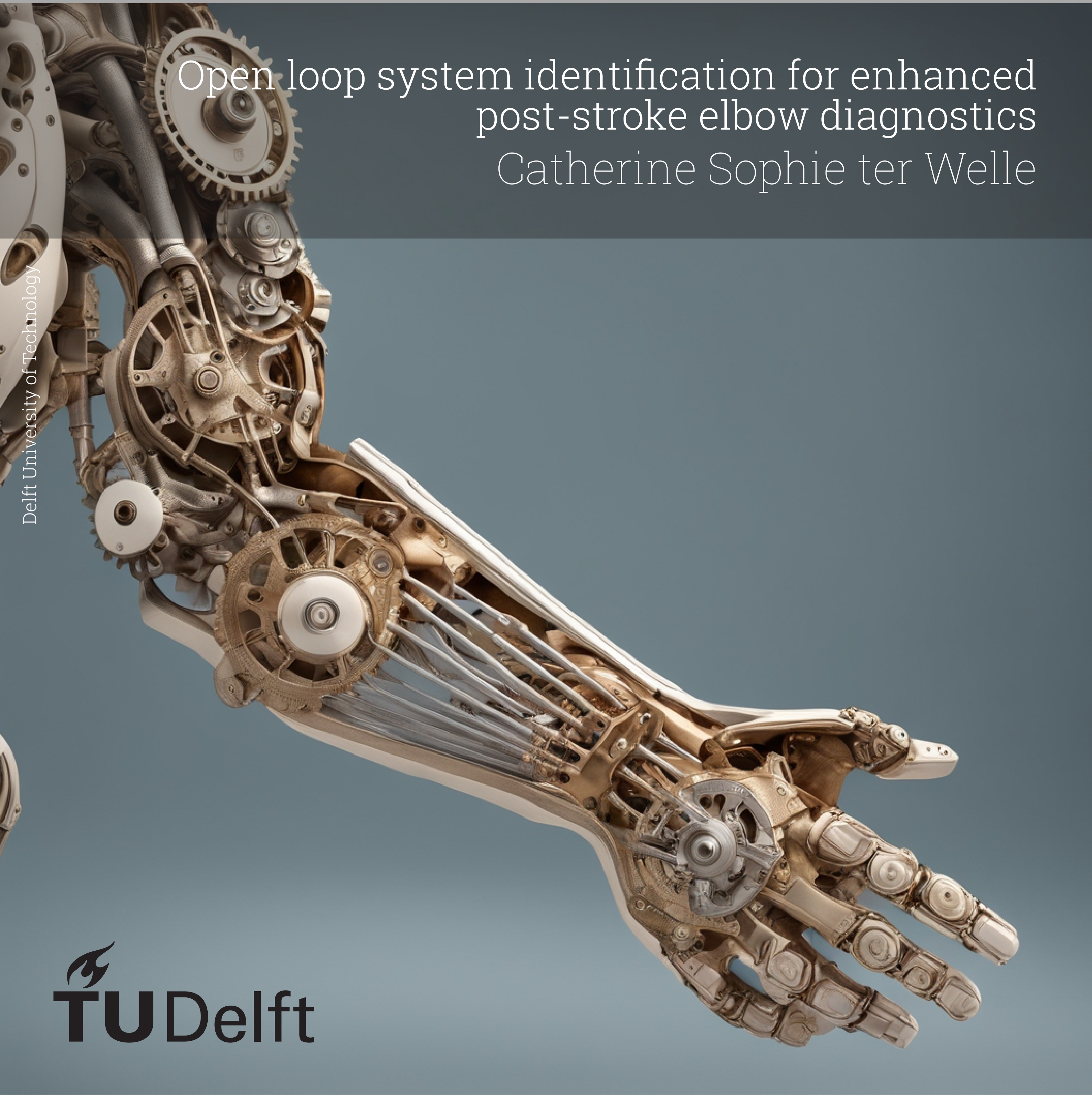

Open loop system identification for enhanced post-stroke elbow diagnostics

Catherine Sophie ter Welle

Delft University of Technology

The Separate Identification of Intrinsic and Reflexive Joint Impedance

Open loop system identification for enhanced post-stroke elbow diagnostics

by

Catherine Sophie ter Welle

to obtain the degree of Master of Science
at the Delft University of Technology,
to be defended publicly on Friday September 27 2024 at 11:00 AM.

Student number:	4670337	
Project duration:	January 1, 2024 – September 27, 2024	
Thesis committee:	dr. ir. M.L. van der Ruit,	TU Delft
	dr. ir. A.H.A. Stienen,	TU Delft
	prof. dr. ir. A.C. Schouten	TU Delft
	dr. ir. M. Jafarian	TU Delft

Cover: https://deepai.org/machine-learning-model/text2img

Preface

This master thesis marks the end of my journey as a student at the TU Delft. During my studies, which started with a bachelor's degree in Clinical Technology and now ends with a master's degree in Biomechanical Design, I have become increasingly interested in robotic technologies and their application in healthcare. I am grateful for TU Delft's opportunities to explore this field and shift my focus to the more technical aspects of rehabilitation robotics. This thesis assignment provided another chance to further this interest, by balancing a strong foundation in technical fundamentals with a large clinical relevance.

I first want to thank Mark and Arno for their supervision during this project. Arno, your enthusiasm for improving the care for those with motion disorders and your efforts to always find the connection to the clinical relevance are very motivating. Mark, thank you for your introduction into the world of system identification. I have enjoyed our insightful discussions and appreciate the fact that you encouraged me to stick to my own theories, even if you found them to be untrue.

Secondly, I want to express my appreciation for the other students at both the 'NMC lab' and 'Arm Hand Group'. The talks with you on the contents and the process of a graduation project have helped me feel supported throughout mine. Especially thanks to Jonathan, for always giving your (unrequested) opinion over (free) coffee. I look forward to continuing our discussions the coming years.

I also want to thank Matin Jafarian and Alfred Schouten for being part of my thesis graduation committee.

A big thank you to my friends and family for making the past 7 years enjoyable and allowing me a break once in a while. And lastly, I want to thank Anne, for listening to me up to the point of complete boredom and starting all over again the next day. I gain my energy from sharing my interests with you, and will continue to bore you for many years to come.

Karien ter Welle
Delft, September 2024

Summary

In Upper Motor Neuron Lesion (UMNL) following stroke, patients can experience increased joint impedance, resisting joint rotation and hindering functional movement. This heightened impedance in UMNL is driven by both exaggerated reflexes and increased intrinsic muscle activation through co-contraction, hypertonus, or synergies. The simultaneous presence of these mechanisms complicates clinical distinction, especially given their theorised interplay, where increased intrinsic activation would further heighten reflex responses. Separate quantification of this intrinsic and reflexive impedance and their interaction, can aid in further investigation of the pathophysiology of post-stroke joint impairment and its treatment.

This work presents the investigation of an Open Loop System Identification (OL-SID) protocol, to perform this separate quantification of intrinsic and reflexive impedance for the elbow joint. Perturbation experiments were performed with 16 healthy subjects, using multisine positional perturbations and measuring the elbow torque response. An impedance model consisting of both intrinsic and reflexive parameters was fit to the estimated frequency response function (FRF), relating perturbation angle to joint torque. It was assessed how background muscle activation, as well as the frequency and velocity of the perturbation signal, influenced the modelled intrinsic stiffness, intrinsic damping, and reflex velocity-gain.

For this, three different biceps muscle activation levels were requested from the participants in different trials; 0%, 10%, and 30% of Maximum Voluntary Contraction (MVC), as confirmed by online EMG measurements. Participants were requested to not actively resist perturbations, but only to comply with the requested biceps activation level. Furthermore, three rotational multisine perturbations with a max. amplitude of 2 degrees were applied; Wide Bandwidth ($0.2 - 10Hz$ bandwidth and $\sim 0.5\frac{rad}{s}$ avg. velocity), Narrow Bandwidth ($0.2 - 3Hz$ bandwidth and $\sim 0.2\frac{rad}{s}$ avg. velocity), and Wide Bandwidth Low Power ($0.2 - 10Hz$ bandwidth and $\sim 0.2\frac{rad}{s}$ avg. velocity). Cross-combination of biceps activation levels and perturbation signal resulted in 9 impedance quantifications per participant.

Increased biceps activation resulted in a significant increase of intrinsic stiffness, intrinsic damping, and the reflex-gain. This confirmed the expected relationship between muscle activation and intrinsic impedance, as well as the theorised relation between intrinsic activation and the reflex response. Unexpectedly, differences in used perturbation bandwidth or velocity showed no clear influence on identified reflex gain. This contradicts findings of reflex suppression during high-bandwidth force perturbations in tasks that require resisting these perturbations, as well as during high-velocity binary or unidirectional joint stretches. This discrepancy shows that joint system identification results are highly dependent on perturbation type and subject task, emphasising the need to align the experimental design with the clinical question at hand.

Despite some shortcomings regarding low coherence of the estimated FRFs, and necessary further research on perturbation signal properties and their effect on the reflex response, the results of this study are promising. The observed trends in fitted parameters with increased activation levels in line with physiological expectations, indicate the ability of this technique to validly identify reflexive and intrinsic joint impedance. This distinction is highly valuable for advancing investigation of the pathophysiology and clinical presentation of UMNL post-stroke, in the pursuit of adequate treatment for different patients.

Contents

List of Figures

List of Tables

1

Introduction

A cerebrovascular incident, or stroke, is the leading cause of adult disability in Europe [1]. Disruption of oxygen flow to the brain, whether from a haemorrhage or thrombus leading to ischaemia, can damage the upper motor neurons, resulting in upper motor neuron lesion (UMNL). UMNL causes a subsequent movement disorder and disability [2]. Shortcomings in the post-stroke rehabilitation process include subjective assessment and limited understanding of the complex clinical presentation of UMNL [3, 4]. Technological advancements in diagnostic robotics have attempted to solve these shortcomings over recent decades, but remain in the experimental stage without wide adoption in clinical practice [4].

The elbow joint is of particular interest in clinical diagnostics of UMNL. Its impairment greatly affects daily activities [5] and occurs frequently compared to other joints [6], with reported incidences of $\sim$ 57% [7] across all stroke cases. Its monoplanar motion makes it an ideal candidate for robotic assessment, as this simplifies the evaluation of joint properties [8]. Focusing on advancing robotic diagnostics for the post-stroke elbow is thus a strategic step towards increased clinical relevance and adoption of these techniques.

1.1. Post-stroke joint impedance

UMNL changes the dynamic properties of joints, hindering patients in interactions with their environment [9]. Clinical terms for distorted post-stroke joints (e.g. spasticity, hypertonia, and hypotonia) are often indefinite and used inconsistently in literature [10, 11]. The overarching term 'joint impedance' describes the dynamic torque resistance to a joint rotation in a general manner. The problem of post-stroke joints is twofold: decreased volitional joint impedance when functional for a task, and increased non-volitional joint impedance when attempting to relax [12, 13]. Clinical relevance lies in connecting UMNL pathophysiology to either increased or decreased joint impedance, referred to as 'positive' and 'negative' features respectively [2, 14]. The changes to joint impedance of a post-stroke joint are comprised of a combination of different mechanisms. These can be categorised into those affecting intrinsic impedance, through passive biomechanical changes or alterations in active muscle tension, and those affecting reflexive impedance (fig. 1.1).

Intrinsic active changes

UMNL initially presents with reduced joint impedance following reduced voluntary muscle tension, due to distorted muscle control [2, 13] or (fear of) pain in muscle activation [22, 23]. The ensuing upregulation of alternative motor pathways to replace the disrupted ones can cause a non-volitional increase in muscle activation [16]. This includes co-contraction [14], muscle hypertonia in rest [14], and synergistic activation patterns [16, 24, 25], presumably due to cortical overlap of the newly formed motor pathways [25].

Intrinsic passive changes

The disuse and immobilisation of musculature in UMNL changes the passive biomechanical properties of muscles and tendons. Reduced muscle mass and cross-sectional area can cause a decreased intrinsic muscle stiffness [19]. On the other hand, a reduction of the number of sarcomeres in series [18] and fibrosis of muscle and tendon structures [17] can increase passive joint stiffness [12, 13, 15]. Furthermore, joint damping can be increased through the formation of viscous oedemas [20, 21].

Reflexive changes

Patients with UMNL exhibit exaggerated 'spastic' spinal cord reflexes, involving a monosynaptic Ia afferent pathway that is activated by the stretch of velocity-sensitive muscle spindles [2, 13, 15]. While partly explained by hyperexcitable muscle spindles [13], the pathological increase in reflex response is also a secondary consequence of disturbed cortical influences. Decreased dorsal reticulospinal inhibition and

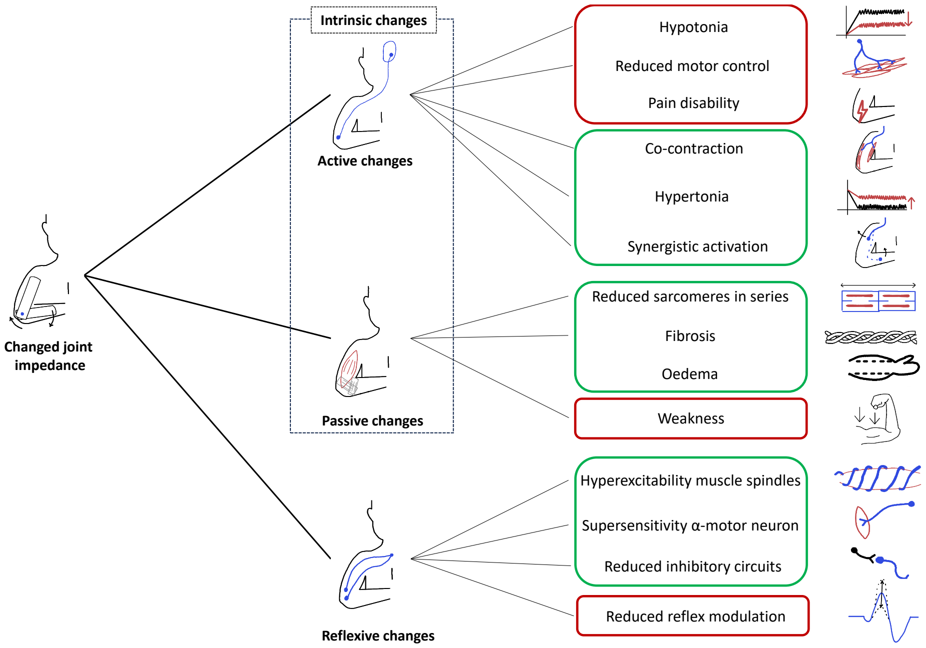

Figure 1.1: Overview of proposed causes of changed joint impedance post-stroke, as found in [2, 12, 13, 15–23]. Green and red color indicate increased non-volitional joint impedance ('positive') and decreased volitional joint impedance ('negative'), respectively.

'denervation hyperexcitability' of the α-motor neurons, both due to the absence of voluntary cortical control [13], contribute to a heightened reflex response [26].

While the exaggerated stretch reflex increases joint impedance, reflexes in UMNL show 'negative' characteristics as well. In cases where reflexes are functional for task performance, post-stroke patients show both decreased short- [12] and long-latency [15, 27, 28] reflexes compared to a healthy cohort. This is most likely explained by muscle weakness and the inability to upscale reflex gains when functional [12, 27].

Clinical interaction between joint impedance mechanisms

Intrinsic and reflexive joint impedance cannot be regarded as fully separate entities. Increased intrinsic activation would bring motor units closer to the firing threshold [29] and lead to larger motor unit recruitment in case of a reflex, according to the size-recruitment principle [30]. This causes a positive correlation between muscle activation and reflex response, referred to as 'gain scaling' [30–32]. A similar relationship is theorised in the post-stroke population between non-volitional intrinsic muscle activation and exaggerated spastic reflexes [24, 29]. In the elbow specifically, a relation can be observed between synergistic elbow flexor activation during shoulder abduction and elbow flexor reflexes [16, 24, 29]. However, this gain scaling phenomenon remains disputed. It is reportedly reduced or absent in stroke patients [15, 31, 33] and even absent in healthy cohorts [34] or only seen in long-latency reflexes [35].

Still, the simultaneous presence and interaction of increased intrinsic and reflexive joint impedance creates disagreement on the primary cause of the high non-volitional resistance to joint rotation observed in post-stroke patients. This hinders finding adequate treatment for the right patient population. Stretching should increase the extensibility of soft tissues and normalise muscle tone, but remains without consensus regarding its ability to reduce joint impedance [36]. Interventions with Botulinum Toxin do reduce joint impedance through presynaptic inhibition of reflexes [37], but remain without clear advantages in functional outcome [37] and appear effective for only specific patient populations [38]. Separate quantification of intrinsic and reflexive impedance and their interaction will aid in a further understanding of pathophysiology, assessment of specific treatment effects, and shaping therapies for UMNL [9, 39].

1.2. Quantification of joint impedance

Clinical evaluation

Clinically, increased joint impedance is assessed with the (Modified) Ashworth Scale (MAS) [40] or (Modified) Tardieu Scale (MTS) [41], consisting of a clinician extending a joint and rating the resistance on an ordinal scale. Both the MAS and MTS are criticised for low inter-rater reliability [41–43] and poor ability to specify the severity of spasticity due to only using 5 or 6 ordinal levels respectively [43]. A further drawback of these clinical examinations is the lack of discriminative ability. The MAS as a measure for ’spasticity’ is unable to differentiate between different causes of increased joint impedance and therefore of low validity to determine the presence of exaggerated reflexes rather than intrinsic impedance increase [10, 44]. This hinders providing treatment focused on individual UMNL presentation and assessing the effect of treatment on specific joint impedance mechanisms.

Robotic quantification of joint impedance

Over the past decades, there has been a rise of diagnostic devices and robotics, proving a useful tool in objective and precise measurements of post-stroke joint impedance [3, 4, 8, 45, 46]. The more simple forms of this robotic quantification use Ramp-and-Hold (RH) joint rotations [47, 48] and mimic the MAS examination. These continue to face difficulties in simultaneously and separately identifying intrinsic and reflexive contributions to joint impedance [49]. This could partly explain the low evidence for the clinical benefit of these techniques [4, 46, 50]. Increased attention to a proper model for joint impedance quantification [4, 45], with a focus on discriminating different contributions to joint impedance, could aid in clinical uptake [3]. A promising approach for this is the use of system identification, where the relation between input perturbations and the joints response, is fit to such a mechanical model. This allows for simultaneous, but separate, quantification of intrinsic, both passive and active, and reflexive joint impedance [31, 51–53].

One common approach is the use of continuous multisine torque perturbations and system identification in the frequency domain, combined with different task instructions. In a ’position task’ the participant is asked to resist perturbations and retain a fixed joint angle, effectively increasing their impedance [53, 54]. In a ’force task’, the participant is asked to minimise deviations of the force exerted on the perturbator, thus actively ’giving way’ to the perturbations and reducing their impedance [55]. These assignments mimic our natural interaction with the environment and assess the ability to voluntarily change our joint impedance [9]. The use of a multisine perturbation gives great control over its bandwidth, which is known to alter the nonlinear reflex response. More specifically, a perturbation bandwidth containing frequencies around or above the joints’ eigenfrequency would cause participants to reduce their reflex response [12, 53].

Conversly, when not the voluntary adjustment of joint impedance but the non-volitional joint impedance is of interest, another approach is common. Short rotational stretches or alternating binary switches of joint angle in Pseudo Random Binary Sequence (PRBS) perturbations [52, 56, 57] are often used in identifying the involuntary torque response to perturbation. The task instruction for the participant is often to fully relax or to match a specific constant muscle flexion, but not to react to perturbations. This approach more directly captures Ia-reflexes, as these respond to displacement rather than torque disturbance. The reflex response is especially sensitive to the velocity of this displacement, with both too low [47] and too high [52, 57] movement velocities theorised to reduce reflex magnitude.

1.3. Research goal

This work focuses on the joint impedance of the elbow, separating the reflexive and intrinsic contributions using system identification. With the ultimate goal of designing a system identification protocol to distinguish and quantify spastic reflexes, intrinsic synergistic activation, and their interaction as observed in the post-stroke elbow, a first step is made investigating a healthy cohort.

As the choice of task and perturbation type influence the identified joint behaviour [9, 58], these must be carefully considered regarding the clinical question at hand. With the focus on non-volitional reflexes and non-volitional (synergistic) muscle activation, a positional perturbation which is not actively resisted by the participants is chosen as a fitting experimental setup. A task instruction to match a requested level of biceps contraction is used to mimic synergistic activation, as this is not displayed in a healthy cohort [29]. To fully control both the bandwidth and velocity of perturbation, multisine rotational perturbations are used. Previous research on this specific perturbation type is limited, with little investigation into how perturbation properties influence identified joint impedance in these experiments [31, 33, 59, 60].

First, the effect of activation level is assessed, to understand its’ influence on both the identified intrinsic impedance and on the reflexive impedance through the gain scaling phenomenon. Secondly, it is assessed how varying perturbation velocity and bandwidth affect the identified impedance to determine which signal properties are most effective in either inducing or suppressing a reflex response. These assessments aid in validating and optimising the system identification approach used to quantify elbow impedance.

2

Methodology

2.1. Participants

16 healthy participants (ages 22-56), consisting of 6 males and 10 females, were recruited for the experiments. All participants had no history of elbow impairment and gave their informed consent prior to the experiments.

2.2. Perturbation device

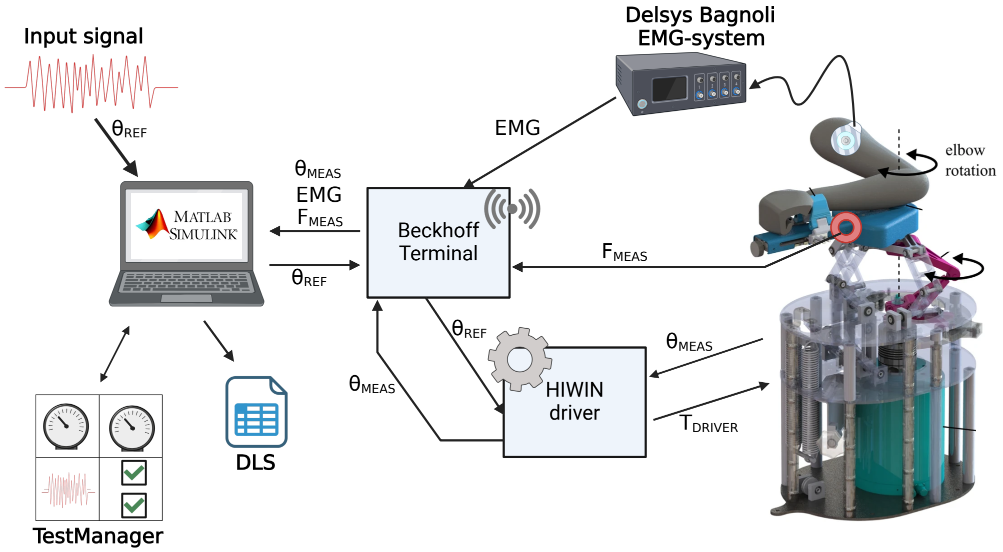

Figure 2.1: Overview of the full experimental setup, consisting of both hardware and software components that make up the Shoulder Elbow Perturbator (SEP) as used in this thesis. DLS = Data Logging System, 'meas' = measured, and 'ref' = reference. Technical drawing of the SEP is taken from [61].

2.2.1. Hardware and software

For the experiments, a diagnostic robotic device developed by Hankamp Rehab B.V., the Shoulder Elbow Perturbator (SEP), was used [61]. It features two primary diagnostic functionalities.

- **Assessing joint impedance through elbow perturbation.** A high torque rotary table (TMS3C, HIWIN, Taiwan), connected to a cantilever underarm support, rotates the elbow joint through alignment with the medial epicondyle of the elbow. The rotary encoder embedded in the rotary table measures the angular rotation of the elbow. A strain gauge load cell (LCM200, USA) connected in series to the cantilever beam measures the force between the arm and the lever, used to estimate elbow torque.
- **Assessing flexion synergy of the elbow through varying shoulder abduction support.** A Sarrus linkage mechanism is used to passively support the arm in shoulder abduction, of which the support force can be varied. This allows for studying the effect of own shoulder abduction efforts of a post-stroke subject on their elbow joint impedance through synergistic elbow flexor activation.

Two extra analogue input channels allow for connecting a surface electromyography (sEMG) measurement system (Bagnoli 16ch system, Delsys, USA). Data transfer and communication with a controller PC is performed through an ethernet module (EK1100, Beckhoff, Germany). On the PC, a controller algorithm in Simulink (MATLAB, 2014b) runs at 1000 Hz, which is compiled to C++-code before deployment through EtherLab. EtherLab Data Logging Service (DLS) can be used to acquire and save data corresponding to channels in the Simulink model at a sample frequency of 1000 Hz. The controller model can be commanded through TestManager software, which allows for control mode switches, initiating preset experiments and real time data monitoring.

2.2.2. Position controller

Rotational perturbations require a highly stiff perturbator control algorithm, to provide perturbation of the joint up to adequate bandwidth. Issues with inadequate sampling frequency and resolution of the rotary encoder data communicated to the controller PC, can destabilise position control. As within the motor servo controller itself (D1 Drive, HIWIN, Taiwan), more detailed encoder information is available, the internal velocity controller can be used to display higher controller stiffness without instability. This ensures adequate reference signal tracking in different loading conditions (stiff arm, slack arm, and no arm). The Simulink controller model is then used solely for preprocessing the rotation reference signal and activating the HIWIN velocity controller mode. Controller design efforts and comparisons of initial and final controller performance can be found in Appendix A.

2.2.3. Participant positioning

As the current experiment was conducted with a healthy cohort, the mechanism to analyse flexion synergy of the elbow was unused and put to ’maximum support’, allowing subjects to fully rest their elbow on the support. For elbow joint positioning, the medial epicondyle of the humerus was aligned with the centre of the rotary table. To properly transfer the perturbations to the elbow, a clamp at the end of the cantilever underarm support was fixated on the wrist as tight as possible without causing more than mild discomfort. The neutral elbow angle around which perturbations were applied was 90°. Dry electrodes for sEMG measurements were placed on the biceps brachii and the medial head of the triceps brachii, known as main elbow flexor and extensor muscles [62]. This completed the full experimental setup as shown in figure 2.1.

2.3. Task instruction

To mimic the effect of non-volitional intrinsic activation due to post-stroke synergies, different biceps flexion levels were requested from the healthy participants [29]. Participants were asked to match a specific activation level, instead of a flexion torque. As the relation between neurological muscle activation and force output can change due to fatigue [63], EMG signal was deemed a more direct indicator of muscle activation. Note the fundamental difference between the described task instruction and the often used ’force task’ [55]. In a force task the participant actively minimises force deviations by reducing joint impedance. In the current task, the participant ’ignores’ the perturbations and only focuses on maintaining the correct background muscle activation, not actively adjusting their joint impedance. This is referred to as an ’activation task’ in the remainder of this work.

Prior to the experiments, EMG signal during maximum voluntary contraction (MVC) of the biceps in neutral position (90°) was determined. All further EMG measurements were normalised with respect to the range between this MVC and a baseline rest EMG level, which is deemed an appropriate method for assessing voluntary activation levels [64]. Three biceps activation levels were requested during different perturbation trials. A 0% MVC level served as a baseline with no expected reflex, a 10% MVC level was expected to induce a reflex [65], and a 30% MVC level was used to evaluate if increased activation would further increase the reflex gain. Higher activation levels were anticipated to increase fatigue [34] without significantly affecting reflex gains, as the relationship tends to plateau [35, 59, 60].

Real-time visual feedback of EMG signal was provided to the participant to aid in maintaining the correct activation level. The signal was low-pass filtered at $\sim$ 0.2 Hz, as higher frequency feedback hindered maintaining steady background activation. A first-order Bessel filter was used to minimise phase lag and thus time delay, known for its linear phase response in the passband [66]. As a Bessel filter is not common in EMG signal analysis, an offline comparison was made between the Bessel filter and the more commonly used moving Root Mean Square (RMS) filter with a 1-second window [67], to assess the validity of the Bessel filter for EMG signal visual feedback. Online monitoring ensured that triceps activation levels remained below 3% of MVC, to prevent active resisting of perturbations through co-contraction.

2.4. Perturbation signals

For the perturbation trials, multisine rotational perturbations, with a maximum amplitude of 2° were used, comparable to other system identification experiments [56, 59, 68]. Larger amplitudes could cause nonlinearity in the estimated system, as joint impedance is known to vary for different joint angles [34, 60, 69]. The used multisine perturbations had a constant spacing of $0.2Hz$ between excited frequencies. This reduction in frequency resolution compared to a white noise perturbation, increases the power per frequency and thus the signal-to-noise ratio (SNR) in the analysis [70]. Three different multisine perturbation signals were designed by varying frequency and velocity content. These different properties were used to investigate their influence on the identified joint impedance, especially the nonlinear reflex response.

The natural frequency of the elbow ($\omega_n = \sqrt{\frac{k}{I}}$) is expected around $\sim$ 1 Hz in rest and $\sim$ 4 Hz in high activation, based on a reported inertia of 0.11 $\frac{\text{Nm}\cdot\text{s}^2}{\text{rad}}$ and a stiffness of 1-8 $\frac{\text{Nm}}{\text{rad}}$ in a relaxed state and 50 - 80 $\frac{\text{Nm}}{\text{rad}}$ in an activated state [59, 68, 71]. A Wide Bandwidth (WB) perturbation up to 10 Hz was expected to excite frequencies well above ω_n and capture the full system dynamics. A second Narrow Bandwidth (NB) perturbation up to 3 Hz was designed to only excite frequencies below ω_n of the activated elbow.

The desired velocities of the different perturbations were determined based on a comparison of other system identification literature (Appendix B) and achieved through cresting. The cresting of a multisine is a process of optimising the relative phase shifts to obtain a high velocity and high power signal. Added sinusoids with random relative phase create a multisine with a crest factor of $\sim$ 3 - 4, while an optimised signal for high velocity and power has a crest factor of $\sim$ 2 [70].

The slightly crested WB signal had an average velocity of above 0.5$\frac{\text{rad}}{\text{s}}$, theorised to suppress reflex response [52, 57]. The crested NB signal had an average velocity of 0.2$\frac{\text{rad}}{\text{s}}$, above the theorised lower bound for reflex induction [47, 48], but below the suppression velocity. A third perturbation signal (WB Low Power - WB LP) was designed to separate the effects of perturbation bandwidth and velocity, by using a wide bandwidth perturbation but an average velocity similar to the NB signal. This was achieved through more power at the low frequencies, a high crest factor, and a reduction of amplitude to max. 1.5°.

To increase the robustness of the analysis, the three perturbation signal types were realised in two variants that were expected to generate similar results. These differed in the random phase of the added sinusoids, without large changes in the bandwidth or velocity properties of the perturbation. This resulted in the 6 signals presented in table 2.1. Figure 2.2 shows the Power Spectral Density (PSD) of the three different perturbation signal designs.

Table 2.1: Velocity and frequency content of the different perturbation signals used in the experiments. RMS = Root Mean Square, WB = Wide Bandwidth, NB = Narrow Bandwidth, WB LP = Wide Bandwidth Low Power.

Perturbation	Bandwidth	RMS vel ($\frac{\text{rad}}{\text{s}}$)	Max vel ($\frac{\text{rad}}{\text{s}}$)	Crest factor
1. WB	0.2 - 10 Hz	0.56	1.75	2.68
2. WB	0.2 - 10 Hz	0.53	1.28	2.50
3. NB	0.2 - 4 Hz	0.21	0.45	1.89
4. NB	0.2 - 4 Hz	0.21	0.51	2.96
5. WB LP	0.2 - 10 Hz	0.23	0.83	3.18
6. WB LP	0.2 - 10 Hz	0.20	0.73	3.67

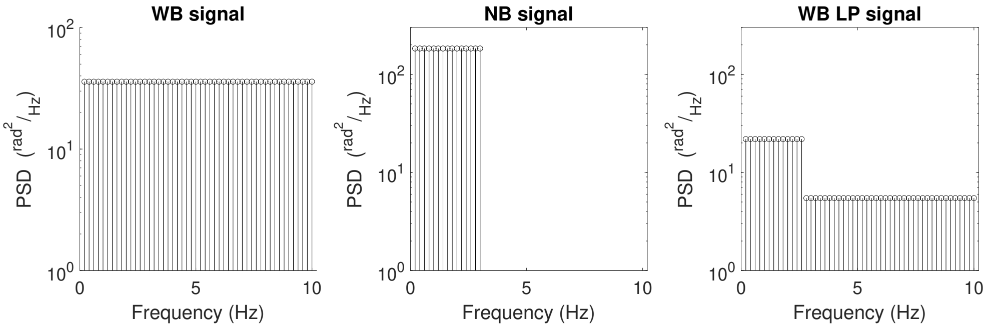

Figure 2.2: Power Spectral Density (PSD) of the used perturbations.

2.5. Protocol and recordings

Cross-combination of the six perturbation signals with the three activation level tasks, resulted in 18 trials per participant. The 0% MVC and 10% MVC trials had a duration of 210 seconds. To prevent fatigue, the 30% MVC trials were split into two segments of 110 seconds. To further prevent the effects of fatigue on the outcomes, the perturbation types were applied in random order, while the activation levels were always in the order of 0%, 10%, 30% MVC. As a control, the full perturbation experiment was also performed without a participant, to assess the impedance of the unloaded arm support.

For the system identification, joint angle and joint torque were recorded at a sample frequency of 1000 Hz. Joint torque was calculated by multiplying the force measurement with the 0.11 m moment arm between the sensor and center of rotation. The low-pass filtered sEMG measurements from the biceps musculature were not used for system identification, but recorded for offline assessment of adequate task execution from the participants.

The full experimental protocol, including safety measures, the SEP device report, and informed consent documentation can be found in Appendix C-Appendix F. Approval of this protocol was provided by the Human Research Ethical Committee of the Mechanical Engineering faculty of the TU Delft on June 6th 2024. The experiments were conducted between June 6th and June 26th.

2.6. Data analysis

2.6.1. Experiment assessment

Activation level assessment

Comparability of the results was deemed more important than exact biceps activation levels of 0%, 10%, and 30% of MVC. Therefore, the calculated mean (Act_{mean}) and standard deviation (Act_{SD}) of activation level across all participant trials were used for trial inclusion or exclusion, rather than thresholds based on exactly 0%, 10% and 30% MVC. Normal distribution of average EMG signal per activation level was confirmed with the Shapiro-Wilk test [72]. Subsequently, two criteria were used for the exclusion of a trial based on activation level.

- An average activation level outside of the $Act_{mean} \pm 2 \cdot Act_{SD}$ range.
- An activation level outside of the $Act_{mean} \pm 3 \cdot Act_{SD}$ range for a full signal period (5 seconds).

As during 0% MVC trials, negative readings occurred due to some EMG signal drift and not actual deviation from the target activation, it was decided to only exclude 0% MVC trials based on an upper boundary breach.

Perturbation signal assessment

To analyse the performance of the perturbator controller in tracking the desired perturbation signal over the different experiments, a comparison between the desired and actual perturbation angle was performed in both the time and frequency domain. For assessment in the time domain, the tracking root mean square error (RMSE) between desired and actual joint rotation was calculated. For assessment in the frequency domain, the frequency response function (FRF) from desired to actual joint rotation and its deviation from a magnitude of 1, was assessed.

2.6.2. Non-parametric Open Loop System Identification (OL-SID)

Figure 2.3a shows the used system identification setup. The rotation exerted by the perturbator results in a torque on the handle applied by the human. The perturbator is infinitely stiff compared to the joint, assuming adequate perturbator control and actuator stiffness. This results in Open Loop System Identification (OL-SID), where the torque exerted on the perturbator by the human, does not influence the angular rotation of the perturbator and the joint. For this OL-SID, an FRF relating the perturbation angle as input to the measured joint torque as output can be derived, based on a similar derivation for Closed Loop System Identification (CL-SID) described in the work by van der Helm et al. [53].

In the frequency domain, the Fourier transform of the human reaction torque T_{handle} and the handle angle θ_{pert} are related through a multiplication operation with the FRF $H_{T\theta}$. With the addition of the unmodeled $N(f)$ (noise or nonlinearity), the measured torque at the handle (T_{meas}) can then be derived as follows:

$$T_{meas}(f) = \theta_{pert}(f) \cdot H_{T\theta}(f) + N(f). \tag{2.1}$$

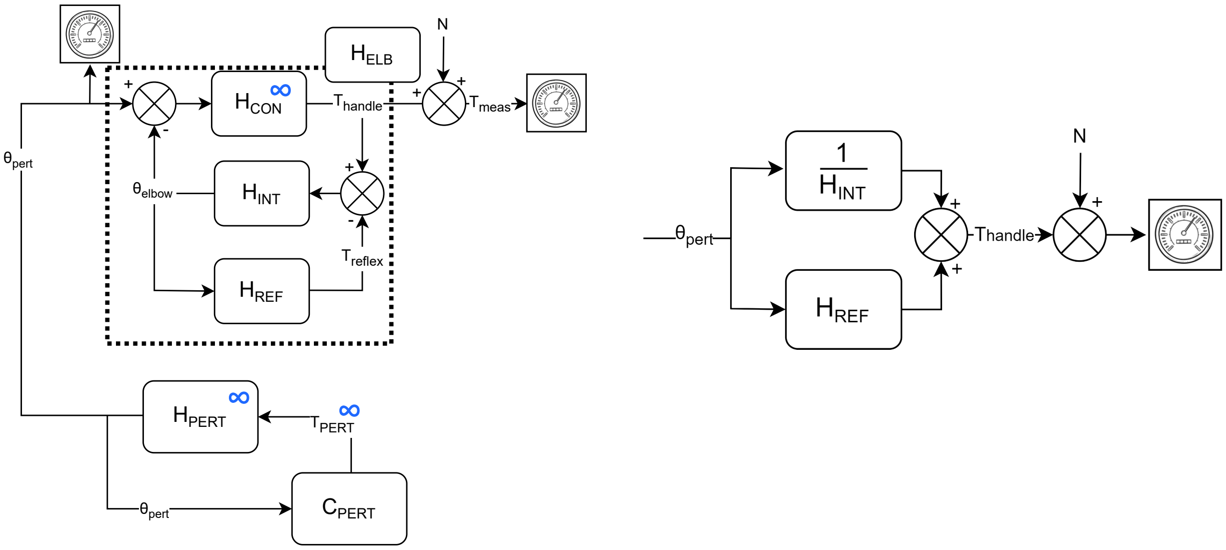

(a) Full overview OL-SID.

(b) Parallel configuration of OL-SID.

Figure 2.3: Block diagrams of Open Loop System Identification (OL-SID) setups.

By multiplying equation 2.1 with the complex conjugate transform of joint angle $\theta^*_{pert}(-f)$ and making use of the definition of the (cross-)PSD S_{xy}:

$$S_{xy} = E\{X(f) \cdot Y^*(-f)\}, \tag{2.2}$$

equation 2.1 changes to

$$S_{T\theta} = S_{\theta\theta} \cdot H_{T\theta} + S_{N\theta}. \tag{2.3}$$

Note that since calculating the true PSD requires an infinite number of data points, an approximation is often used instead. If the noise is assumed to be uncorrelated with the positional perturbation, the cross-PSD between $N(f)$ and θ_{pert} ($S_{N\theta}$) equals 0, resulting in the estimation for $H_{T\theta}$:

$$\hat{H}_{T\theta}(f) = \frac{\hat{S}_{T\theta}}{\hat{S}_{\theta\theta}}. \tag{2.4}$$

The coherence between in- and output gives an indication of of system linearity and measurement noise:

$$\gamma^2(f) = \frac{|\hat{S}_{T\theta}|^2}{\hat{S}_{\theta\theta} \cdot \hat{S}_{TT}}, \tag{2.5}$$

which ranges from 0 to 1, equalling 1 if the unmodelled noise and nonlinearity $N(f)$ equals 0 [53].

Prior to PSD approximation, the first 10 seconds of the acquired data for each trial were discarded to remove initial transient effects. Joint angle and torque data were low-pass (6th order, 11 Hz) and high-pass (2nd order, 0.1 Hz) filtered to reduce effects of drift and high-frequency noise. The remaining 200 seconds per trial (or 2x 100 s for the 30% MVC trials) were split into 40 segments containing one signal period of 5 seconds.

The (cross-)PSDs of perturbation angle (θ_{pert}) and measured joint torque (T_{meas}) were estimated using the Welch periodogram spectrum estimation method, averaging the estimated PSD of the 40 segments to reduce the effects of noise [73]. If one of the two 100 seconds 30% MVC trials was excluded due to the procedure described in 2.6.1, the remaining 20 segments were averaged in the Welch procedure to estimate the PSDs. The resulting PSDs were used to estimate joint FRFs and coherence according to equations 2.4 and 2.5 respectively. The FRF of the unloaded SEP was calculated using the same method.

2.6.3. Parametric model

The FRF relating perturbation angle and output joint torque can be estimated with a model for elbow joint impedance, H_{ELB}. Figure 2.3a shows three components of H_{ELB}. H_{CON} describes the viscoelasticity of the contact between the perturbator and the subject. H_{INT} is the intrinsic impedance of the joint, dictated by passive biomechanical properties and intrinsic muscle activation. Lastly, H_{REF} describes the reflex reaction to a rotation of the joint. Block diagram algebra for fig. 2.3a gives the full relationship between θ_{elbow} and T_{handle}, where the (f) indicating frequency dependence is omitted for legibility:

$$\begin{aligned} T_{handle} &= H_{CON} \cdot \theta_{pert} - H_{CON} \cdot \theta_{elbow} \\ &= H_{CON} \cdot \theta_{pert} - H_{CON}\left(\frac{T_{handle} \cdot H_{INT}}{1 + H_{REF} \cdot H_{INT}}\right) \end{aligned} \tag{2.6}$$

For OL-SID, it is assumed that the contact between the perturbator and the human limb is infinitely stiff, meaning the joint (θ_{elbow}) and perturbator (θ_{pert}) angle are equal [31, 52, 71]. This assumption is expected to hold up until $\sim$ 13 Hz [68] (Appendix H). The assumption of $H_{CON} = \infty$, allows rewriting of equation 2.6 into:

$$\frac{T_{handle}}{H_{CON}} = \theta_{pert} - \frac{T_{handle} \cdot H_{INT}}{1 + H_{REF} \cdot H_{INT}} = 0, \tag{2.7}$$

leading to

$$\frac{\theta_{pert}}{T_{handle}} = \frac{H_{INT}}{1 + H_{REF} \cdot H_{INT}}. \tag{2.8}$$

For the torque resistance of the elbow joint to the perturbation, described by the full elbow impedance H_{ELB}, equation 2.8 needs to be inverted:

$$\frac{T_{handle}}{\theta_{pert}} = H_{ELB} = \frac{1}{H_{INT}} + H_{REF}. \tag{2.9}$$

Note that the only difference between the actual exerted joint torque (T_{handle}) as used in equation 2.9 and the measured torque (T_{meas}) as used in the PSD estimation for equation 2.4, is the addition of noise and nonlinearity (N).

The derived equation 2.9 can be schematically depicted in a parallel configuration, seen in figure 2.3b. Here the output torque as a result of angular perturbation is an addition of the parallel intrinsic and reflexive paths, as often seen in OL-SID research [52, 56, 71].

The intrinsic joint impedance, consisting of both passive biomechanical and active muscle contributions, was modelled with the common mass-spring-damper model in rotation, depicted in the Laplace domain as:

$$H_{INT} \simeq \frac{1}{I \cdot s^2 + b_{int} \cdot s + k_{int}}, \tag{2.10}$$

where $s = j\omega$, I, b, and k are the Laplace operator, inertia, damping, and stiffness respectively [31, 51, 68].

Reflexive impedance in the most elaborate description is modelled as follows:

$$H_{REF} \simeq (k_a \cdot s^2 + k_v \cdot s + k_p) \cdot e^{-T_d \cdot s} \cdot H_{ACT}. \tag{2.11}$$

Here k_a, k_v, and k_p are the acceleration, velocity and positional reflex gain respectively, T_d is the reflex time-delay and H_{ACT} describes muscle activation dynamics [51, 53]. In this work, k_p and k_a were considered negligible, assuming reflexes mostly respond to perturbation velocity [13, 70]. Both the activation dynamics and time delay parameters were fixed based on related literature. For H_{ACT}, a first-order system with a time constant of 0.03 and thus a low-pass cut-off frequency of 5.3 Hz was used [53]. The time-delay of the reflex T_d was estimated at 40 ms [29, 74–76]. This resulted in a reflex model with only k_v as a free variable.

2.6.4. Parameter estimation

The parameters of the elbow impedance model were estimated to match the modelled impedance to the measured FRF. For this, parameter fitting was performed by using the MATLAB 'lsqnonlin' solver, with the gradient-based 'Trust-Region Reflective' algorithm [77], to minimise the error function:

$$L(p) = \sum_{f=0.4}^{f=BW} \frac{1}{1+f} \cdot |\ln \frac{\hat{H}_{T\theta}(f)}{\hat{H}_{ELB}(f)}|^2. \tag{2.12}$$

Here f is the analysed frequency, p the model parameter set, $\hat{H}_{\theta T}$ the measured FRF, and $\hat{H}_{ELB}$ the modelled elbow impedance [68]. As the 0.2 Hz content appeared to be distorted by both drift and the applied low-pass filter, the fits were performed for the frequencies from $f =$ 0.4 Hz up to bandwidth ($f = BW$), only evaluating frequencies present in the perturbation. A factor $(1 + f)^{-}1$ and use of the logarithmic error both prevent emphasis on high frequencies where larger errors occur due to large absolute impedance [68].

Elbow inertia was fit separately from the other parameters, as it was expected to be uninfluenced by perturbation signal type or activation level. The inertia was estimated for the 0% MVC trials of the WB and WB LP signals and averaged to yield one inertia estimation used in all other fits. The best inertia fit was sought by minimising the objective function shown in eq. 2.12 for frequencies between 4 - 7 Hz only, a range above the natural frequency of the elbow and well below the influence of contact dynamics. As only a small range of high frequencies was used, the correction factor $(1 + f)^{-}1$ was omitted.

The NB perturbation bandwidth was too limited to estimate the intrinsic damping parameter. The average of the damping estimations for the other perturbations (WB and WB LP) was thus used as a fixed damping value for NB fitting, as seen in other literature [53, 70].

Two models for H_{ELB} were fit to the measured FRFs. One consisting of only the intrinsic impedance (I-model, H_{INT}) and one consisting of both the intrinsic and reflexive impedance (IR-model, $\frac{1}{H_{INT}} + H_{REF}$). Both models were fit with the same initial and boundary values for the intrinsic parameters (Appendix G). The quality of both fits was assessed using the 'Variance Accounted For' (VAF) metric, which indicates how much of the data variance is explained by the fitted model (eq. 2.13). Measured ($T(t)$) and model predicted torque ($\hat{T}(t)$) were compared, with a VAF of 100% indicating a perfect fit.

$$VAF = (1 - \frac{\sum_{i=1}^{N}(T(t_i) - \hat{T}(t_i))^2}{\sum_{i=1}^{N} T(t_i)^2}) \cdot 100\% \tag{2.13}$$

2.7. Statistical analysis

The fitted parameters were averaged over the 2 different realisations of the same perturbation signal. If a trial with one of the realisations was excluded based on the procedure described in section 2.6.1, the fitted parameters of the single remaining realisation were used as the 'average'. This resulted in 1 value for each parameter per perturbation signal (WB, NB, WB LP) per activation level, averaged over all participants and used for statistical evaluation. Both the effect of activation level on intrinsic impedance parameters k_{int} and b_{int} as on reflexive parameter k_v were statistically evaluated. Only the fitted parameters of the IR-model were statistically compared, while the differences between the I- and IR-model were discussed qualitatively, to limit the number of statistical comparisons. For similar reasons, the effect of different perturbation signals on the quantified impedance, specifically the nonlinear reflex response, was also only discussed qualitatively.

Prior to statistical comparison, the normal distribution of the fitted parameters was assessed using the Shapiro-Wilk test [72]. A one-way Repeated Measures (RM) ANOVA statistical test [78] was performed to identify the influence of muscle activation level on the fitted parameters, with an additional Greenhouse-Geisser [79] correction in case a sphericity violation was determined with Mauchly's test for sphericity [80]. A posthoc analysis was performed for $0\% \rightarrow 10\%$, $0\% \rightarrow 30\%$, and $10\% \rightarrow 30\%$ MVC activation level steps using a paired t-test with Bonferroni correction. This is a good alternative to the Tukey Honest Difference test in the case of repeated measures with possible sphericity violations [81, 82]. Since an increase in fitted parameters with activation level was expected, a one-tailed t-test was used. For the three post-hoc comparisons, the significance level was adjusted to $\alpha = 0.05/3 = 0.0167$, to keep the family-wise error rate below 0.05. This same threshold was applied when assessing normality and sphericity prior to statistical comparison, ensuring the same correction across the three activation levels.

3
Results

3.1. Activation level assessment

Offline comparison of the MVC values obtained from EMG signals filtered with the commonly used moving RMS filter versus the Bessel filter revealed an average difference of approximately 5% (Appendix I). The first-order online Bessel filter was thus considered adequate for real-time feedback of muscle activation.

Using the Bessel-filtered EMG signals, the mean estimated biceps EMG level during MVC was 562.3 mV, compared to a mean EMG signal in the relaxed state of 47.9 mV. Some presence of drift in the EMG signal reading resulted in readjusting these normalisation values in between trials. Average EMG drift magnitude was 6.8% of the total range from relax to MVC (Appendix J).

The activation levels reached during trials were normally distributed over participants, as assessed with the Shapiro-Wilk test (Appendix K). Average activation levels were -0.08% [$\pm$2.3%] (negative due to slight EMG-drift), 10.82% [$\pm$1.0%] and 29.87% [$\pm$1.1%] of MVC for the 0%, 10% and 30% MVC trials respectively. Appendix L shows the exclusion based on the two criteria stated in 2.6.1. In total, 32 out of 375 completed trials were excluded based on muscle activation level (18 due to average, 14 due to 5 s deviation).

3.2. Perturbation signal tracking

The tracking of the desired perturbation signal by the SEP was adequate, but decreased slightly with increasing muscle activation and increasing perturbation velocity, as both require more control force. When comparing reference and actual perturbation signals in the time domain, the tracking RMSE was highest at 30% MVC for the WB signal, with an average of 0.16°.

In the frequency domain, the FRF from desired to actual joint rotation showed a slight overshoot around $\sim 7Hz$ with an FRF magnitude >1, while at the highest perturbated frequencies ($\sim$ 9 - 10 Hz), it dropped below 1. The highest average overshoot occurred at the WB signal and 30% MVC trial (FRF $=$ 1.42$\pm$0.10$)$) and the lowest FRF magnitude occurred at the WB LP signal and 10% MVC trial (FRF $=$ 0.46 $\pm$ 0.09). Tracking in both time and frequency domain is visualised in Appendix M, including listed RMSE and max. and min. FRF values for all activation levels and perturbation types.

3.3. Non parametric analysis

3.3.1. Frequency response functions

The average frequency response functions (fig. 3.1) resemble a second-order system for all activation levels and all signal types. While slightly less straightforward than in a regular mass-spring-damper model due to the added reflex, the transition of the stiffness dominated impedance to the mass dominated impedance will still be referred to as the natural frequency (ω_n). An increase in the standard deviation of the FRF magnitude and phase can be observed for higher activation levels. The FRF of the unloaded SEP identified using the different perturbation signals can be observed in Appendix N.

3.3.2. Coherence

At low frequencies, the coherence drops significantly, equalling almost 0 at the lowest excited frequencies (fig. 3.1). Coherence appears to increase simultaneously with the impedance increase beyond ω_n. As the activation level increases, ω_n increases, and the point where coherence improves is also shifted upwards. For the NB signals, coherence at low frequencies is slightly higher, not dropping below 0.2 as for the WB and WB LP perturbations.

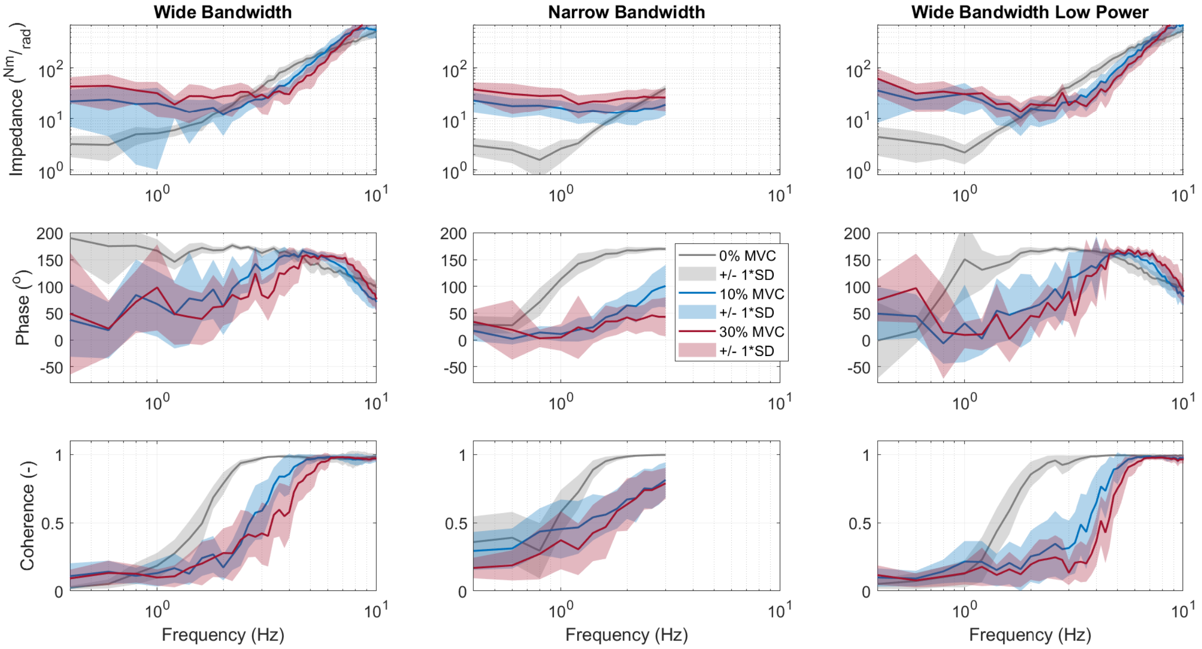

Figure 3.1: Results for non-parametric analysis. Top row shows the magnitude of the Frequency Response Function (FRF), middle row the phase of the FRF and bottom row the coherence between the input perturbation angle and output torque. Columns correspond to the different perturbation signals, and colors to the different activation levels.

3.4. Parametric analysis

3.4.1. Qualitative description

Figure 3.2 shows an exemplary fit of the IR-model for two trials at 0% and 30% MVC, best suited to show the reflex contribution to impedance. Exemplary fits for all signals types and activation levels can be found in Appendix O. At the 0% activation level, the fitted reflex component is minimal as the intrinsic model properly describes the FRF (fig. 3.2, left). As muscle activation level increases to 30% MVC, the total stiffness and ω_n increase. However, the increase in ω_n is larger than can be explained by only the increased stiffness, causing a mismatch unsolvable only by the intrinsic model (fig. 3.2, centre).

As the reflex is modelled as a velocity gain with a time delay, its main action can be observed up until and around the natural frequency of the system, between $\sim$ 1 - 4 Hz. The addition of the reflex model acts twofold:

- Reflexive impedance is added, resulting in a slightly lower estimate of intrinsic stiffness, added together with the reflexive impedance to match the FRF at low frequencies.
- Due to the reflexive and intrinsic impedance being out of phase in the 2-4 Hz region, the higher impedance caused by inertia in the intrinsic model is reduced by the reflexive response. This results in what appears as a longer flat 'stiffness line' in the FRF and postponing of ω_n, thus solving the mismatch in stiffness and ω_n. This is visible in the right column of figure 3.2.

These effects seen in the exemplary fits were further supported by the average fits of the I-model and IR-model (Appendix P), which overlapped for lower activation levels, but deviated as muscle activation increased. The average VAF of both fits can be seen in table 3.1. Overall VAF values were quite low, in line with the low average coherence, especially for the NB perturbation where only the low coherence frequencies were analysed. Despite the clearly improved FRF fit, only a slight increase in VAF could be observed when fitting with the IR-model instead of the I-model. The VAF increase was largest for the NB signals and the highest activation levels. A comparison of measured and modelled torque in the time domain, used to calculate the VAFs, is shown in Appendix Q.

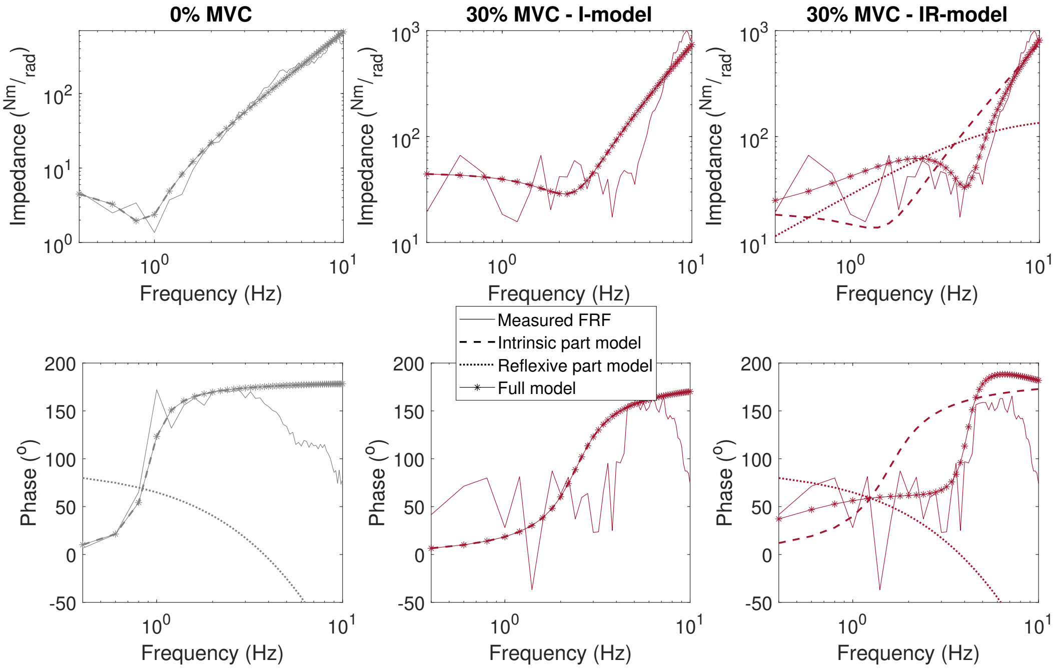

Figure 3.2: Example of fitting a joint impedance model to the measured FRF. The fitted model is a combination of intrinsic and reflexive impedance (IR-model). Left: A 0% MVC trial. Right: A 30% MVC trial.

Table 3.1: Variance Accounted For (VAF) [SD] for the intrinsic (I-model) and combined intrinsic and reflexive (IR-model) model fits, for different perturbation types and activation levels.

Perturbation	**Model**	**Activation level**		
		0% MVC	*10% MVC*	*30% MVC*
WB	*Int*	67.7% [14.7%]	75.1% [9.1%]	76.7% [2.5%]
	Int + Ref	67.4% [14.4%]	71.7% [8.4%]	79.7% [3.0%]
NB	*Int*	73.3% [6.6%]	26.1% [12.8%]	27.9% [11.8%]
	Int + Ref	80.7% [5.6%]	41.4% [12.5%]	35.4% [9.9%]
WB LP	*Int*	68.3% [9.6%]	65.8% [5.9%]	60.9% [8.0%]
	Int + Ref	65/6% [9.3%]	63.0% [11.2%]	70.2% [8.1%]

3.4.2. Fitted parameters

Averaging, normality, and distribution

Fits were performed separately for the two realisations of each perturbation signal. No statistical differences between the fitted parameters of the two realisations were found (Appendix R), supporting the choice to average all fitted parameters over the two signal realisations. This results in one value for each parameter per signal type (WB, NB, WB LP), per activation level, averaged over participants and shown in figure 3.3.

As the activation level increased, the difference between the fitted parameters of the I-model and IR-model increased, in line with the qualitative observations in section 3.4.1. All four fitted parameters for all nine trials were normally distributed over participants (Appendix S), except k_{int} at the WB 10% MVC trial due to two outliers and k_v at the WB 0% MVC trial due to equalling 0 for almost all participants. This was deemed adequate for a parametric analysis. Statistical comparisons were executed for the IR-model only. A complete overview of the statistical analysis, including all p-values, F-statistics, Greenhouse-Geisser correction factors for the ANOVA, and confidence intervals for the post hoc analyses, can be found in Appendix T.

Intrinsic parameters

For the inertia estimation for all activation levels and perturbation signals, the average of the inertia estimation from 0% WB and 0% WB LP was used. The average inertia estimation for the 0% WB ($0.155\frac{\text{Nm}\cdot\text{s}^2}{\text{rad}}$)

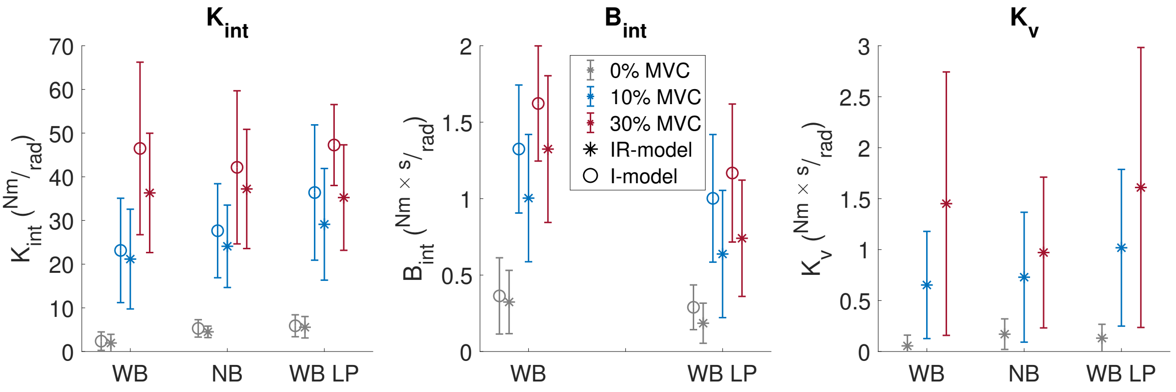

Figure 3.3: Average fitted parameters for all participants for different activation levels and signal types. Bars show $\pm 1 \cdot SD$. k_{int}, b_{int}, and k_v are intrinsic stiffness, intrinsic damping and reflex gain respectively. NB b_{int} parameters are not shown, as these were not fit separately but obtained through averaging WB and WB LP b_{int}.

and for the 0% WB LP ($0.173 \frac{\text{Nm} \cdot \text{s}^2}{\text{rad}}$) did differ significantly ($p < 0.001$). Averaging thus resulted in a slight over- and underestimation of inertia for WB and WB LP trials respectively.

The RM-ANOVA showed a significant increase in intrinsic stiffness ($p <$ 0.0001 for all perturbation types) and in intrinsic damping ($p <$ 0.0001 for all perturbation types) with increased activation level, as seen in figure 3.3. The post hoc analysis results were the same for intrinsic stiffness and damping. A significant increase of k_{int} and b_{int} was found for all increases in activation level ($p <$ 0.0167 for the $0\% \rightarrow 10\%$, $10\% \rightarrow 30\%$ and $0\% \rightarrow 30\%$ steps) for all perturbation types, except for the WB LP perturbation $10\% \rightarrow 30\%$ activation level step.

Visual inspection of figure 3.3 shows no large influence of perturbation type on the intrinsic stiffness estimations. For intrinsic damping, parameter estimation did change slightly with the perturbation signal, decreasing from WB to WB LP. For the NB perturbation damping is not presented, as it was not fitted separately.

Reflex gain

Just as the intrinsic parameters, the reflex gain increased significantly with increased activation level ($p <$ 0.001 for all perturbation types). The increase for the WB and WB LP perturbations appeared similar, whereas the increase for the NB perturbation appeared slightly smaller (fig. 3.3). This was confirmed by the post hoc testing. A significant increase of k_v was found for all increases in activation level ($p <$ 0.0167 for the 0% → 10%, 10% → 30% and 0% → 30% steps) for all perturbation types, except the 10% → 30% step for the NB perturbation.

The standard deviation for the fitted reflex parameter was large, especially at high activation levels, due to large inter-subject differences. Illustrative of the inter-subject variability is the considerable number of subjects that show no reflex response at all, even at high activation levels where the average reflex gain clearly increases. Table 3.2 shows the high number of trials where no reflex response was identified, which was especially large for the WB and WB LP perturbations.

Table 3.2: Number of trials for which a reflex gain of $k_v = 0 \frac{Nm \cdot s}{rad}$ was fit, for different activation levels and perturbation types.

Perturbation	**Activation level**		
	0% MVC	*10% MVC*	*30% MVC*
WB	26	6	8
NB	6	6	3
WB LP	14	4	6

4

Discussion

This study utilised OL-SID with an activation task and multisine perturbations at different bandwidths and velocities for system identification of the elbow joint. The goal was to fundamentally assess the influence of both activation level and perturbation signal properties on the identified intrinsic and reflexive contributions to joint impedance. This could lead to an experimental protocol to quantify and distinguish the impedance contributions of spastic reflexes and non-volitional muscle activation through synergies, as seen in the post-stroke elbow. The reported findings are promising for reaching this objective. The voluntary activation task to mimic non-volitional synergistic activation was executed well with aid of visual EMG feedback, and the perturbation trials with the SEP produced consistent results. The used impedance model distinguished intrinsic and reflexive impedance. The increase of both with increased activation level suggests proper quantification, aligning with physiological expectations. The unexpected limited influence of perturbation type on the nonlinear reflex response forms a starting point for further research.

4.1. Effect of activation level on fitted parameters

4.1.1. Intrinsic parameters

Both intrinsic stiffness (k_{int}) and damping (b_{int}) increased with activation level. This is in line with other experimental research [31, 34, 57, 59, 83] and can be explained physiologically by an increased number of recruited cross-bridges in activation [83]. These exhibit both stiff behaviour when stretched and viscous damping behaviour due to cyclic-turnover [84]. The increase from 0% to 10% MVC appears larger than that from 10% to 30%. This 'flattening' of the relationship between muscle activation and intrinsic impedance has been previously reported [57, 59, 60]. The assumption occasionally made that intrinsic parameters are linearly dependent on the level of muscle activation might thus be overly simplistic [54] .

The large spread in intrinsic parameters can be explained by differences in strength of participants [59], confirmed by the increased standard deviation with activation level. The average values of the fitted intrinsic parameters correspond to other literature on the elbow joint, with reported ranges for elbow stiffness and damping at different activation levels being 0-75$\frac{\text{Nm}}{\text{rad}}$ and 0.3-3$\frac{\text{Nm}\cdot\text{s}}{\text{rad}}$ respectively [34, 59, 68].

4.1.2. Reflex gain

The reflex gain is shown to increase with activation level, confirming the theorized 'gain scaling' relationship, consistent with findings in most literature investigating this at both neurological [24, 29, 30, 33] and neuromechanical [31, 33, 59] level. The opposing claim in the work of Mirbagheri *et al.* that reflex gain decreases with intrinsic muscle activation, could be explained by the used model [34]. Mirbargheri *et al.* use the bandwidth of muscle activation dynamics as a free parameter in the reflex model, seeing it increase with muscle activation. This could result in a similar increased reflex response as observed with the increased k_v value in the current work. Found average values for reflex gain of the elbow are in the same order of magnitude as in related literature, ranging from 0 to 2$\frac{\text{Nm}\cdot\text{s}}{\text{rad}}$ [31, 59, 71].

The distribution of reflex gain for different subjects has a large standard deviation, and results show a relatively large number of subjects with trials with $k_v = 0\frac{\text{Nm}\cdot\text{s}}{\text{rad}}$ values, even at higher activation levels. This large inter-subject variation can be seen in other studies using OL-SID with background activation tasks as well [34, 83]. This task does not let reflexes contribute to performance, causing less homogeneous group behaviour [34]. Another explanation could be a local minimum for the gradient-based solver of the error function in equation 2.12. To remain conservative in adding reflex action to the model, low initial values ($k_v = 0.1\frac{\text{Nm}\cdot\text{s}}{\text{rad}}$) for the reflex gain were used for the solving algorithm, possibly converging to a local minimum at $k_v = 0\frac{\text{Nm}\cdot\text{s}}{\text{rad}}$ for some trials.

4.2. Effect of perturbation signal on fitted parameters

4.2.1. Intrinsic parameters

The inertia parameter for the WB LP signal was significantly larger than that of the WB signal. This is a remarkable finding which can only be explained by noise or unmodelled dynamics, as arm inertia is independent of perturbation type. Further investigation is required to ensure valid identification of elbow inertia with the SEP.

The influence of perturbation type on the intrinsic stiffness (k_{int}) and damping (b_{int}) appears minimal as is often assumed [53, 70] and demonstrated [52, 57] in literature. However, the WB LP signal shows a slightly lower damping across all activation levels, possibly due to the 25% reduction in perturbation amplitude (sec. 2.4) for this signal. The muscle response to stretch generally consists of an initial stretch of the attached cross-bridges, followed by their cyclic turnover, displaying viscous damping [85]. Reducing stretch length could decrease the relative contribution of damping, resulting in the witnessed change for the WB LP perturbation [83]. While the difference is small and sensitive to noise, it does imply that assuming all intrinsic parameters independent of perturbation type may be overly simplistic.

4.2.2. Reflex gain

Effect of perturbation bandwidth

The current work shows no reflex suppression by any of the perturbations, with bandwidths of WB and WB LP perturbations well over the natural frequency (ω_n) of the elbow. Conversely, in most CL-SID research with a position task, the reflex gain decreases if the perturbation bandwidth contains the joints ω_n. Around ω_n, a reflex response and its time delay cause instability and large position deviations. As position deviations reduce task performance, the reflex gain is thus scaled down [12, 53, 70].

This confirms that reflexes assessed in a context where they are functional for task performance (as with CL-SID and a position task) should be considered separate from those in the current context where the presence of reflexes is unrelated to task performance [58]. While previous OL-SID research with relax or activation tasks does not specifically investigate the effect of perturbation bandwidth on the reflex response, higher bandwidth perturbations encompassing joint ω_n [31, 52, 59] are utilized. The largest reflex contribution to impedance is even seen around this ω_n [52].

As in this work, the largest reflex contribution is also seen around the joints natural frequency (2-4 Hz range), including this in the perturbation spectrum could even improve reflex estimations. This reasoning might partly explain the lower estimated reflex activity for the NB perturbation, as ω_n was not within the analysed spectrum.

Effect of perturbation velocity

Unexpectedly, the different perturbation velocities do not greatly induce or suppress the modelled reflex gains either. The discrepancy regarding the interaction between perturbation velocity and reflex gain in related literature confirms the complexity of this relation. From the overview of used perturbation velocities in literature in Appendix B, it can be observed that the relationship between perturbation velocity and reflex suppression is highly dependent on the type of perturbation signal used.

In most OL-SID research with small amplitude perturbations, k_v ($\frac{\text{Nm}\cdot\text{s}}{\text{rad}}$) is used as a main reflex parameter; a velocity gain of the reflex that itself will decrease when perturbation velocity increases [52, 59, 83]. However, disagreement remains on which specific velocities induce or suppress a reflex (Appendix B), warranting consideration of other perturbation properties. One key difference is the movement pattern of the different perturbation types: small amplitude ramp-and-hold stretches rotate $\sim$ 0.15 rad at a constant velocity, PRBS perturbations involve high-velocity binary switches ($\sim$ 0.03 rad) with rest periods, and multisine perturbations alternate directions with variable velocities. These patterns also affect acceleration content of the perturbation, which is known to influence reflex response independently of velocity [86].

Reflex responses are highly nonlinear, influenced by muscle spindle nonlinearity [57, 85], presynaptic inhibition during fast joint rotation or high-frequency vibration [87], and nonlinear muscle activation dynamics [52]. As these nonlinearities could be sensitive to different movement patterns and perturbation accelerations, comparing velocity effects across different perturbation types may not be feasible. In this study, perturbation velocities were close to those expected to alter the reflex response in PRBS but lower than used in other multisine studies (Appendix B). This suggests that 'high-velocity' perturbations may not have been sufficient to cause reflex suppression, indicating a need to further consider perturbation signal differences.

4.3. Methodological considerations

4.3.1. Used reflex model

To reduce model fit complexity, the reflex response was assumed to consist only of a positive velocity gain k_v, with the lower bound for fitting set at 0. This forces the reflexes in the current research to be an excitory response only to the perturbation velocity, exiting musculature to resist the perturbation. This neglects other possible contributions to reflexes, such as positional and acceleration gains [51, 59], force feedback reflexes through Golgi Tendon Organs (GTO) [55], and inhibitory Ia-reflexes with a negative k_v value [55]. While addition of more components can make the model more complete, the physiological implication of the fitted parameters must be considered.

The velocity sensitivity of muscle spindles grounds the assumption that k_v is the primary contributor to the Ia-reflex response [13]. Inhibitory negative k_v feedback and inhibitory GTO feedback, are not often identified, typically only in tasks where subjects actively aim to reduce joint impedance. Since participants in this experiment were not instructed to reduce their impedance, inhibitory Ia- and GTO-feedback were omitted from the model fits. An additional analysis allowing k_v to fall below 0 (Appendix U) revealed inhibitory negative reflex fits in some trials, even at high activation levels without the task to reduce impedance. This indicates that while a model may converge to a solution, deviations from physiological expectations require cautious interpretation of the results.

The fitted reflex response in this study (fig. 3.3) aligns with physiological expectations. For the 0% MVC trials, the I-model and IR-model fit overlap, conform the absence of a reflex response for a healthy relaxed biceps muscle. As muscle activation increases, so does the IR-model's reflex response, consistent with the 'gain scaling' phenomenon [29, 30]. At higher activation levels, intrinsic impedance is higher for the I-model than the IR-model fits, as the reflex response in the IR-model partly replaces this intrinsic impedance [59]. The IR-model's better fit for the FRFs translates to slightly higher VAF values at higher activation levels. While VAF generally increases with model complexity [59], the observed trends, consistent with neuromuscular control theories, further support confidence in the fitted reflex response. However, a more detailed reflex model could enhance the analysis. Specifically, including k_a could better address the complex relationship between perturbation velocity and reflex gain, which is also acceleration-dependent [86].

4.3.2. Coherence

A caveat in the analysis is the low coherence for the FRFs at low frequencies. This may be due to noise or drift in the torque signal, caused by inconsistent biceps contractions of participants, when matching requested activation levels. At low frequencies, impedance is minimal, making the torque output relatively small compared to this noise (Appendix V), resulting in a low SNR, low coherence, and low VAF values for the fit [70]. This explanation is supported by the rise of coherence as the impedance increases due to inertia beyond ω_n. Low coherence at low frequencies caused by drift is shown and discussed in other research using OL-SID with position perturbations [33, 59]. However, the issue does not appear for CL-SID with torque perturbations with the SEP [68]. This difference may arise because the dependency of coherence on joint impedance as seen in the current OL-SID is not present in CL-SID coherence, as derived in Appendix W.

Low coherence does not necessarily indicate incorrect joint impedance estimation. The Welch-averaging of 40 segments in he current analysis reduced the noise effects in the PSD estimation [73]. To evaluate this averaging, the analysis was also conducted with half the data (100s, 20 segments), of which results are shown in Appendix X. The 100s and 200s measurement analysis resulted in very similar PSDs, FRFs, and average fitted parameters. This similarity suggests convergence to the 'true' PSD and FRF, with noise adequately averaged out. However, individual fitted parameters per trial showed larger variations between the 100s and 200s measurements, highlighting their sensitivity to noise and number of averaged segments. Since the low-coherence and low-frequency region does remain an important part of the parameter estimation, the fitting error function was not weighted by coherence to avoid reducing the influence of low coherence frequencies on the fit, as seen in other research [68].

4.3.3. Contact and attachment dynamics

The high-frequency region of the FRFs (fig. 3.1) showed some deviation of the common inertia +2 slope in magnitude and +180° in phase, possibly related to contact dynamics. For OL-SID, the contact dynamics must be 'infinite', assuming the same rotation angle for the perturbator as the joint. An estimation based on previous research with the SEP [68] (Appendix H) showed validity of this assumption up to $\sim$ 13 Hz, while the the measured FRFs showed contact dynamics effects up from $\sim$ 7 Hz. To reduce the influence of contact dynamics on the parameter estimations, the inertia was fit only using frequencies up to 7 Hz. Further research should aim at increasing contact stiffness, to increase the frequency up untill which the 'infinite' stiffness is valid. Alternatively, perturbation signal frequencies above 7 Hz should be omitted if not essential for adequate inertia estimation, as this could increase power at other lower frequencies.

The impedance of the cantilever attachment securing the forearm was expected to consist of only a small inertia component, consistent across perturbation signals. The estimated joint impedance was thus lumped with this 'attachment impedance', as in other OL-SID research [59]. Note that the attachment impedance does not contain motor impedance, as the torque measurement is taken from a sensor between the rotary table and the attachment, not from the motor drive. Unexpectedly, the attachment impedance FRF differed for the different perturbation signals, showing some stiffness for the WB and WB LP perturbations (Appendix N). This inconsistency could be due to oscillations of the SEP during experiments, adding varying SEP structural dynamics to the FRF, with shaking increasing from NB to WB LP to WB perturbations. While these differences are small, they ask for further investigation and careful consideration of results. Especially at 0% MVC trials, where human joint impedance is relatively low compared to this inconsistency.

4.4. Future work

4.4.1. Experimental design

For further research, the issue of decreased coherence at low frequencies must be addressed by increasing low-frequency SNR. This can be achieved by reducing the number of excited frequencies to increase the input power per frequency [70], as demonstrated by the NB perturbation showing slightly higher low-frequency coherence than the WB and WB LP perturbations (fig. 3.1). When reducing the perturbation spectrum, the discussed advantage of keeping the joints ω_n within this spectrum (sec. 4.2.2) should be kept in mind. A reduction in frequency resolution could increase SNR further. Alternatively, CL-SID experiments with torque perturbations could be used to mitigate the low coherence issue, adding a virtual environment to prevent drift during the activation task [88].

In the current work, overall averaged parameter fits and trends appeared adequate, even in the presence of low coherence and SNR. However, fitting procedures for individual participants were unpredictable, susceptible to signal noise, and had divergent results with large standard deviations. More consistent fitting procedures in the presence of noisy measurement data should be further investigated. For instance, Kearney et al. demonstrate an iterative fitting procedure that effectively increases SNR in a fit [52].

Furthermore, investigation is needed into the effect of perturbation velocity on reflex response and how this differs per perturbation type. Special attention must be paid to comparing the effect of instantaneous velocity, average velocity, acceleration, and direction switch patterns. For more 'instantaneous' switches of higher acceleration between joint angles, controller performance would need to improve. The current SEP controller is sufficient for a 10 Hz bandwidth and 2°-amplitude multisine rotational perturbation (Appendix A), but signals approaching PRBS perturbations require higher controller performance. Enhancing hardware with a higher resolution encoder could help meet these demands.

4.4.2. Clinical use and applicability

The current system identification protocol shows promising results in clinically separating (spastic) reflexes from (synergistic) background activation. To enhance its clinical relevance, further steps are needed to improve the protocol's applicability.

EMG measurements are a burden in fast assessments and should thus be replaced. If the mimicking of non-volitional synergistic activation is still desirable for subjects where this does not show naturally, a level of biceps flexion torque could be requested instead [29]. To aid in matching a constant background biceps flexion level, visual feedback of a severely low-pass filtered ($\sim$ 0.2 Hz) torque signal could be used. The low-pass filtering is crucial, to prevent subjects from adjusting their joint torque in response to perturbation, actively decreasing their admittance as in a 'force task' [55].

Further clinical applicability can be reached by consolidating the protocol. Given the minimal effect of perturbation bandwidth on identified impedance, a single perturbation signal with a bandwidth of $\sim$ 5-6 Hz may suffice for the analysis. Future research should investigate the optimal perturbation velocity to induce a reflex response allowing for optimal quantification, and explore the minimal measurement time needed for accurate FRF estimation using Welch averaging [73].

5

Conclusion

This thesis presents the design and evaluation of an OL-SID protocol with multisine rotational perturbations, for simultaneously quantifying intrinsic and reflexive impedance. Both the effect of increased background activation and the effect of different perturbation signal properties on the identified impedance parameters was assessed.

Intrinsic and reflexive impedance both significantly increased with increased activation level, in line with related literature and physiological expectations. This demonstrates the ability of this technique to reliably differentiate and quantify both intrinsic and reflexive impedance. The investigation of different perturbation bandwidths and velocities on the identified impedance parameters brought little-discussed findings to light. First, excitation of the joint natural frequency does not suppress reflex responses in the current experimental setup. Second, the effect of perturbation velocity on reflex suppression is complex and cannot be directly extrapolated from other OL-SID research with PRBS or ramp-and-hold perturbations. Further research is needed to thoroughly investigate this effect and determine the optimal perturbation velocity for reflex induction.

Overall, the separate identification of both intrinsic and reflexive impedance and their change with activation level is a promising result regarding post-stroke research. Clinical separation of these two phenomena could aid in seeking consensus on what is the most prominent problem of post-stroke motion disorder, in pursuit of adequate treatment. Are patients mostly hindered by excessive spastic reflexes in rest [31, 47] or by distorted gain scaling of the reflex due to non-volitional intrinsic muscle activation [12, 29, 33]? Or is the biggest hindrance formed by a change in passive biomechanical impedance, unrelated to reflexive or intrinsic muscle activation at all [18]?

Reference list

[1] C. F. Prendes *et al.*, "Burden of Stroke in Europe: An Analysis of the Global Burden of Disease Study Findings From 2010 to 2019," *Stroke*, vol. 55, no. 2, pp. 432–442, Feb. 2024, Publisher: American Heart Association. DOI: `10.1161/STROKEAHA.122.042022`.

[2] M. C. Emos and S. Agarwal, "Neuroanatomy, Upper Motor Neuron Lesion," in *StatPearls*, Treasure Island (FL): StatPearls Publishing, 2024. [Online]. Available: `http://www.ncbi.nlm.nih.gov/books/NBK537305/`.

[3] Y. Cha and A. Arami, "Quantitative Modeling of Spasticity for Clinical Assessment, Treatment and Rehabilitation," *Sensors (Basel, Switzerland)*, vol. 20, no. 18, p. 5046, Sep. 2020, ISSN: 1424-8220. DOI: `10.3390/s20185046`.

[4] R. de-la Torre, E. D. Oña, C. Balaguer, and A. Jardón, "Robot-Aided Systems for Improving the Assessment of Upper Limb Spasticity: A Systematic Review," *Sensors (Basel, Switzerland)*, vol. 20, no. 18, p. 5251, Sep. 2020, ISSN: 1424-8220. DOI: `10.3390/s20185251`.

[5] O. A. Anakwenze, S. Namdari, J. E. Hsu, J. Benham, and M. A. Keenan, "Myotendinous lengthening of the elbow flexor muscles to improve active motion in patients with elbow spasticity following brain injury," *Journal of Shoulder and Elbow Surgery*, vol. 22, no. 3, pp. 318–322, Mar. 2013, ISSN: 1532-6500. DOI: `10.1016/j.jse.2012.10.043`.

[6] J. Wissel, L. D. Schelosky, J. Scott, W. Christe, J. H. Faiss, and J. Mueller, "Early development of spasticity following stroke: A prospective, observational trial," *Journal of Neurology*, vol. 257, no. 7, pp. 1067–1072, Jul. 2010, ISSN: 1432-1459. DOI: `10.1007/s00415-010-5463-1`.

[7] A. Doussoulin *et al.*, "Prevalence of Spasticity and Postural Patterns in the Upper Extremity Post Stroke," *Journal of Stroke and Cerebrovascular Diseases*, vol. 29, no. 11, p. 105 253, Nov. 2020, ISSN: 1052-3057. DOI: `10.1016/j.jstrokecerebrovasdis.2020.105253`.

[8] D. E. Wood *et al.*, "Biomechanical approaches applied to the lower and upper limb for the measurement of spasticity: A systematic review of the literature," *Disability and Rehabilitation*, vol. 27, no. 1-2, pp. 19–32, Jan. 2005, ISSN: 0963-8288. DOI: `10.1080/09638280400014683`.

[9] C. G. M. Meskers, J. H. de Groot, E. de Vlugt, and A. C. Schouten, "NeuroControl of movement: System identification approach for clinical benefit," *Frontiers in Integrative Neuroscience*, vol. 9, p. 48, 2015, ISSN: 1662-5145. DOI: `10.3389/fnint.2015.00048`.

[10] A. Pandyan *et al.*, "Spasticity: Clinical perceptions, neurological realities and meaningful measurement," *Disability and Rehabilitation*, vol. 27, no. 1-2, pp. 2–6, Jan. 2005, ISSN: 0963-8288. DOI: `10.1080/09638280400014576`. [Online]. Available: `https://doi.org/10.1080/09638280400014576` (visited on 07/23/2024).

[11] S. Malhotra, A. D. Pandyan, C. R. Day, P. W. Jones, and H. Hermens, "Spasticity, an impairment that is poorly defined and poorly measured," *Clinical Rehabilitation*, vol. 23, no. 7, pp. 651–658, Jul. 2009, ISSN: 1477-0873. DOI: `10.1177/0269215508101747`.

[12] C. G. M. Meskers *et al.*, "Muscle weakness and lack of reflex gain adaptation predominate during post-stroke posture control of the wrist," *Journal of Neuroengineering and Rehabilitation*, vol. 6, p. 29, Jul. 2009, ISSN: 1743-0003. DOI: `10.1186/1743-0003-6-29`.

[13] C. Trompetto *et al.*, "Pathophysiology of spasticity: Implications for neurorehabilitation," *BioMed Research International*, vol. 2014, p. 354 906, 2014, ISSN: 2314-6141. DOI: `10.1155/2014/354906`.

[14] N. H. Mayer and A. Esquenazi, "Muscle overactivity and movement dysfunction in the upper motoneuron syndrome," *Physical Medicine and Rehabilitation Clinics of North America*, vol. 14, no. 4, pp. 855–883, vii–viii, Nov. 2003, ISSN: 1047-9651. DOI: `10.1016/s1047-9651(03)00093-7`.

[15] V. Dietz and T. Sinkjaer, "Spastic movement disorder: Impaired reflex function and altered muscle mechanics," *The Lancet. Neurology*, vol. 6, no. 8, pp. 725–733, Aug. 2007, ISSN: 1474-4422. DOI: `10.1016/S1474-4422(07)70193-X`.

[16] A. J. C. McMorland, K. D. Runnalls, and W. D. Byblow, "A neuroanatomical framework for upper limb synergies after stroke," *Frontiers in Human Neuroscience*, vol. 9, p. 82, 2015, ISSN: 1662-5161. DOI: `10.3389/fnhum.2015.00082`.

[17] T. A. H. Järvinen, L. Józsa, P. Kannus, T. L. N. Järvinen, and M. Järvinen, "Organization and distribution of intramuscular connective tissue in normal and immobilized skeletal muscles. An immunohistochemical, polarization and scanning electron microscopic study," *Journal of Muscle Research and Cell Motility*, vol. 23, no. 3, pp. 245–254, 2002, ISSN: 0142-4319. DOI: `10.1023/a:1020904518336`.

[18] N. J. O'Dwyer, L. Ada, and P. D. Neilson, "Spasticity and muscle contracture following stroke," *Brain: A Journal of Neurology*, vol. 119 (Pt 5), pp. 1737–1749, Oct. 1996, ISSN: 0006-8950. DOI: `10.1093/brain/119.5.1737`.

[19] V. Azzollini, S. Dalise, and C. Chisari, "How Does Stroke Affect Skeletal Muscle? State of the Art and Rehabilitation Perspective," *Frontiers in Neurology*, vol. 12, p. 797 559, 2021, ISSN: 1664-2295. DOI: `10.3389/fneur.2021.797559`.

[20] P. Wanklyn, A. Forster, J. Young, and G. Mulley, "Prevalence and Associated Features of the Cold Hemiplegic Arm," *Stroke*, vol. 26, no. 10, pp. 1867–1870, Oct. 1995, Publisher: American Heart Association. DOI: `10.1161/01.STR.26.10.1867`.

[21] H. G. M. Boomkamp-Koppen, J. M. A. Visser-Meily, M. W. M. Post, and A. J. H. Prevo, "Poststroke hand swelling and oedema: Prevalence and relationship with impairment and disability," *Clinical Rehabilitation*, vol. 19, no. 5, pp. 552–559, Aug. 2005, ISSN: 0269-2155. DOI: `10.1191/0269215505cr846oa`.

[22] A. Rahmatian, A. Karbasfrushan, and F. Modara, "Relationship Between Pain and Disability Among Stroke Patients," *Anesthesiology and Pain Medicine*, vol. 13, no. 3, May 2023, ISSN: 2228-7523. DOI: `10.5812/aapm-136330`.

[23] A. K. Treister, M. N. Hatch, S. C. Cramer, and E. Y. Chang, "Demystifying post-stroke pain: From etiology to treatment," *PM & R : the journal of injury, function, and rehabilitation*, vol. 9, no. 1, pp. 63–75, Jan. 2017, ISSN: 1934-1482. DOI: `10.1016/j.pmrj.2016.05.015`.

[24] J. G. McPherson, A. H. Stienen, J. M. Drogos, and J. P. Dewald, "The relationship between the flexion synergy and stretch reflexes in individuals with chronic hemiparetic stroke," *IEEE ... International Conference on Rehabilitation Robotics : [proceedings]*, vol. 2011, p. 5 975 516, 2011, ISSN: 1945-7898. DOI: `10.1109/ICORR.2011.5975516`.

[25] J. Yao, A. Chen, C. Carmona, and J. P. Dewald, "Cortical overlap of joint representations contributes to the loss of independent joint control following stroke," *NeuroImage*, vol. 45, no. 2, pp. 490–499, Apr. 2009, ISSN: 1053-8119. DOI: `10.1016/j.neuroimage.2008.12.002`.

[26] L. Jw, "Symposium synopsis," *Spasticity: Disordered Motor Control*, pp. 487–489, 1980, Publisher: Year Book Medical. [Online]. Available: `https://cir.nii.ac.jp/crid/1570572699783785088` (visited on 08/04/2024).

[27] T. C. Bourke, A. M. Coderre, S. D. Bagg, S. P. Dukelow, K. E. Norman, and S. H. Scott, "Impaired corrective responses to postural perturbations of the arm in individuals with subacute stroke," *Journal of Neuroengineering and Rehabilitation*, vol. 12, Jan. 2015. DOI: `10.1186/1743-0003-12-7`.

[28] R. D. Trumbower, J. M. Finley, J. B. Shemmell, C. F. Honeycutt, and E. J. Perreault, "Bilateral impairments in task-dependent modulation of the long-latency stretch reflex following stroke," *Clinical Neurophysiology*, vol. 124, no. 7, pp. 1373–1380, Jul. 2013. DOI: `10.1016/j.clinph.2013.01.013`.

[29] J. G. McPherson, A. H. Stienen, J. M. Drogos, and J. P. Dewald, "Modification of Spastic Stretch Reflexes at the Elbow by Flexion Synergy Expression in Individuals With Chronic Hemiparetic Stroke," *Archives of Physical Medicine and Rehabilitation*, vol. 99, no. 3, pp. 491–500, Mar. 2018, ISSN: 0003-9993. DOI: `10.1016/j.apmr.2017.06.019`.

[30] J. A. Pruszynski, I. Kurtzer, T. P. Lillicrap, and S. H. Scott, "Temporal evolution of "automatic gain-scaling"," *Journal of Neurophysiology*, vol. 102, no. 2, pp. 992–1003, Aug. 2009, ISSN: 0022-3077. DOI: `10.1152/jn.00085.2009`.

[31] L.-Q. Zhang, S. G. Chung, Y. Ren, L. Liu, E. J. Roth, and W. Z. Rymer, "Simultaneous characterizations of reflex and nonreflex dynamic and static changes in spastic hemiparesis," *Journal of Neurophysiology*, vol. 110, no. 2, pp. 418–430, Jul. 2013, ISSN: 1522-1598. DOI: `10.1152/jn.00573.2012`.

[32] J. G. McPherson, A. H. Stienen, B. D. Schmit, and J. P. Dewald, "Biomechanical parameters of the elbow stretch reflex in chronic hemiparetic stroke.," *Experimental brain research*, vol. 237, no. 1, pp. 121–135, Jan. 2019, ISSN: 0014-4819. DOI: `10.1007/s00221-018-5389-x`.

[33] J. A. Burne, V. L. Carleton, and N. J. O'Dwyer, "The spasticity paradox: Movement disorder or disorder of resting limbs?" *Journal of Neurology, Neurosurgery, and Psychiatry*, vol. 76, no. 1, pp. 47–54, Jan. 2005, ISSN: 0022-3050. DOI: `10.1136/jnnp.2003.034785`.

[34] M. Mirbagheri, H. Barbeau, and R. Kearney, "Intrinsic and reflex contributions to human ankle stiffness: Variation with activation level and position," *Experimental Brain Research*, vol. 135, no. 4, pp. 423–436, Dec. 2000, ISSN: 0014-4819, 1432-1106. DOI: `10.1007/s002210000534`.

[35] E. Toft, T. Sinkjær, and S. Andreassen, "Mechanical and electromyographic responses to stretch of the human anterior tibial muscle at different levels of contraction," *Experimental Brain Research*, vol. 74, no. 1, pp. 213–219, Jan. 1989, ISSN: 1432-1106. DOI: `10.1007/BF00248294`.

[36] L. Gomez-Cuaresma, D. Lucena-Anton, G. Gonzalez-Medina, F. J. Martin-Vega, A. Galan-Mercant, and C. Luque-Moreno, "Effectiveness of Stretching in Post-Stroke Spasticity and Range of Motion: Systematic Review and Meta-Analysis," *Journal of Personalized Medicine*, vol. 11, no. 11, p. 1074, Oct. 2021, ISSN: 2075-4426. DOI: `10.3390/jpm11111074`.

[37] S. Li and G. E. Francisco, “The Use of Botulinum Toxin for Treatment of Spasticity,” *Handbook of Experimental Pharmacology*, vol. 263, pp. 127–146, 2021, ISSN: 0171-2004. DOI: `10.1007/164_2019_315`.

[38] I. S. Corry, A. P. Cosgrove, E. G. Walsh, D. McClean, and H. K. Graham, “Botulinum toxin A in the hemiplegic upper limb: A double-blind trial,” *Developmental Medicine and Child Neurology*, vol. 39, no. 3, pp. 185–193, Mar. 1997, ISSN: 0012-1622. DOI: `10.1111/j.1469-8749.1997.tb07408.x`.

[39] J. C. van den Noort *et al.*, “European consensus on the concepts and measurement of the pathophysiological neuromuscular responses to passive muscle stretch,” *European Journal of Neurology*, vol. 24, no. 7, 981–e38, Jul. 2017, ISSN: 1468-1331. DOI: `10.1111/ene.13322`.

[40] R. W. Bohannon and M. B. Smith, “Interrater reliability of a modified Ashworth scale of muscle spasticity,” eng, *Physical Therapy*, vol. 67, no. 2, pp. 206–207, Feb. 1987, ISSN: 0031-9023. DOI: `10.1093/ptj/67.2.206`.

[41] N. N. Ansari, S. Naghdi, S. Hasson, M. H. Azarsa, and S. Azarnia, “The Modified Tardieu Scale for the measurement of elbow flexor spasticity in adult patients with hemiplegia,” *Brain Injury*, vol. 22, no. 13-14, pp. 1007–1012, Jan. 2008, ISSN: 0269-9052. DOI: `10.1080/02699050802530557`.

[42] N. N. Ansari, S. Naghdi, H. Moammeri, and S. Jalaie, “Ashworth Scales are unreliable for the assessment of muscle spasticity,” *Physiotherapy Theory and Practice*, vol. 22, no. 3, pp. 119–125, Jan. 2006, ISSN: 0959-3985. DOI: `10.1080/09593980600724188`.

[43] S. M. Aloraini, J. Gäverth, E. Yeung, and M. MacKay-Lyons, “Assessment of spasticity after stroke using clinical measures: A systematic review,” *Disability and Rehabilitation*, vol. 37, no. 25, pp. 2313–2323, 2015, ISSN: 1464-5165. DOI: `10.3109/09638288.2015.1014933`.

[44] A. D. Pandyan, G. R. Johnson, C. I. Price, R. H. Curless, M. P. Barnes, and H. Rodgers, “A review of the properties and limitations of the Ashworth and modified Ashworth Scales as measures of spasticity,” *Clinical Rehabilitation*, vol. 13, no. 5, pp. 373–383, Oct. 1999, ISSN: 0269-2155. DOI: `10.1191/026921599677595404`.

[45] E. D. Oña Simbaña, P. Sánchez-Herrera Baeza, A. Jardón Huete, and C. Balaguer, “Review of Automated Systems for Upper Limbs Functional Assessment in Neurorehabilitation,” *IEEE Access*, vol. 7, pp. 32 352–32 367, 2019, Conference Name: IEEE Access, ISSN: 2169-3536. DOI: `10.1109/ACCESS.2019.2901814`.

[46] X. Guo, R. Wallace, Y. Tan, D. Oetomo, M. Klaic, and V. Crocher, “Technology-assisted assessment of spasticity: A systematic review,” *Journal of Neuroengineering and Rehabilitation*, vol. 19, no. 1, p. 138, Dec. 2022, ISSN: 1743-0003. DOI: `10.1186/s12984-022-01115-2`.

[47] M. S. Ju, J. J. J. Chen, H. M. Lee, T. S. Lin, C. C. Lin, and Y. Z. Huang, “Time-course analysis of stretch reflexes in hemiparetic subjects using an on-line spasticity measurement system,” *Journal of Electromyography and Kinesiology*, vol. 10, no. 1, pp. 1–14, Feb. 2000. DOI: `10.1016/s1050-6411(99)00018-8`.

[48] A. Starsky, S. Sangani, J. McGuire, B Logan, and B. Schmit, “Reliability of biomechanical spasticity measurements at the elbow of people poststroke,” *ARCHIVES OF PHYSICAL MEDICINE AND REHABILITATION*, vol. 86, no. 8, pp. 1648–1654, Aug. 2005, ISSN: 0003-9993. DOI: `10.1016/j.apmr.2005.03.015`.

[49] C. S. ter Welle, “Quantification of post-stroke joint impedance using perturbations - A Systematic Review,” *Unpublished*, Mar. 2024.

[50] L. L. van der Velden, M. A. C. de Koff, G. M. Ribbers, and R. W. Selles, “The diagnostic levels of evidence of instrumented devices for measuring viscoelastic joint properties and spasticity; a systematic review,” *Journal of NeuroEngineering and Rehabilitation*, vol. 19, no. 1, p. 16, Feb. 2022, ISSN: 1743-0003. DOI: `10.1186/s12984-022-00996-7`.

[51] A. C. Schouten, W. Mugge, and F. C. T. van der Helm, “NMClab, a model to assess the contributions of muscle visco-elasticity and afferent feedback to joint dynamics,” *Journal of Biomechanics*, vol. 41, no. 8, pp. 1659–1667, Jan. 2008, ISSN: 0021-9290. DOI: `10.1016/j.jbiomech.2008.03.014`.

[52] R. E. Kearney, R. B. Stein, and L. Parameswaran, “Identification of intrinsic and reflex contributions to human ankle stiffness dynamics,” *IEEE transactions on bio-medical engineering*, vol. 44, no. 6, pp. 493–504, Jun. 1997, ISSN: 0018-9294. DOI: `10.1109/10.581944`.

[53] F. C. T. van der Helm, A. C. Schouten, E. de Vlugt, and G. G. Brouwn, “Identification of intrinsic and reflexive components of human arm dynamics during postural control,” *Journal of Neuroscience Methods*, vol. 119, no. 1, pp. 1–14, Sep. 2002, ISSN: 0165-0270. DOI: `10.1016/S0165-0270(02)00147-4`.

[54] A. C. Schouten, E. de Vlugt, J. J. van Hilten, and F. C. T. van der Helm, “Quantifying Proprioceptive Reflexes During Position Control of the Human Arm,” *IEEE Transactions on Biomedical Engineering*, vol. 55, no. 1, pp. 311–321, Jan. 2008, Conference Name: IEEE Transactions on Biomedical Engineering, ISSN: 1558-2531. DOI: `10.1109/TBME.2007.899298`.

[55] W. Mugge, D. A. Abbink, A. C. Schouten, J. P. A. Dewald, and F. C. T. v. d. Helm, “A rigorous model of reflex function indicates that position and force feedback are flexibly tuned to position and force tasks,” *Experimental brain research*, vol. 200, no. 3-4, pp. 325–340, 2010, Publisher: Springer, ISSN: 0014-4819. DOI: `10.1007/s00221-009-1985-0`.

[56] L. Galiana, J. Fung, and R. Kearney, “Identification of intrinsic and reflex ankle stiffness components in stroke patients,” *Experimental Brain Research*, vol. 165, no. 4, pp. 422–434, Sep. 2005. DOI: `10.1007/s00221-005-2320-z`.

[57] A. Klomp, E. de Vlugt, J. H. de Groot, C. G. M. Meskers, J. H. Arendzen, and F. C. T. van der Helm, “Perturbation velocity affects linearly estimated neuromechanical wrist joint properties,” *Journal of Biomechanics*, vol. 74, pp. 207–212, Jun. 2018, ISSN: 1873-2380. DOI: `10.1016/j.jbiomech.2018.04.007`.

[58] F. Doemges and P. M. Rack, “Task-dependent changes in the response of human wrist joints to mechanical disturbance,” *The Journal of Physiology*, vol. 447, pp. 575–585, Feb. 1992, ISSN: 0022-3751. DOI: `10.1113/jphysiol.1992.sp019019`.

[59] L. Q. Zhang and W. Z. Rymer, “Simultaneous and nonlinear identification of mechanical and reflex properties of human elbow joint muscles,” *IEEE transactions on bio-medical engineering*, vol. 44, no. 12, pp. 1192–1209, Dec. 1997, ISSN: 0018-9294. DOI: `10.1109/10.649991`.

[60] L.-Q. Zhang, G. Nuber, J. Butler, M. Bowen, and W. Z. Rymer, “*In vivo* human knee joint dynamic properties as functions of muscle contraction and joint position,” *Journal of Biomechanics*, vol. 31, no. 1, pp. 71–76, Nov. 1997, ISSN: 0021-9290. DOI: `10.1016/S0021-9290(97)00106-1`.

[61] L. L. van der Velden *et al.*, “Development of a single device to quantify motor impairments of the elbow: Proof of concept,” *Journal of NeuroEngineering and Rehabilitation*, vol. 19, no. 1, p. 77, Jul. 2022, ISSN: 1743-0003. DOI: `10.1186/s12984-022-01050-2`.

[62] J. G. Alcid, C. S. Ahmad, and T. Q. Lee, “Elbow anatomy and structural biomechanics,” *Clinics in Sports Medicine*, vol. 23, no. 4, pp. 503–517, vii, Oct. 2004, ISSN: 0278-5919. DOI: `10.1016/j.csm.2004.06.008`.

[63] B. Bigland-Ritchie and J. J. Woods, “Changes in muscle contractile properties and neural control during human muscular fatigue,” *Muscle & Nerve*, vol. 7, no. 9, pp. 691–699, 1984, ISSN: 0148-639X. DOI: `10.1002/mus.880070902`.

[64] J. Diong, K. C. Kishimoto, J. E. Butler, and M. E. Héroux, “Muscle electromyographic activity normalized to maximal muscle activity, not to Mmax, better represents voluntary activation,” *PLOS ONE*, vol. 17, no. 11, e0277947, Nov. 2022, ISSN: 1932-6203. DOI: `10.1371/journal.pone.0277947`.

[65] C. P. Nicolozakes, M. H. Sohn, E. M. Baillargeon, D. B. Lipps, and E. J. Perreault, “Stretch reflex gain scaling at the shoulder varies with synergistic muscle activity,” *Journal of Neurophysiology*, vol. 128, no. 5, pp. 1244–1257, Nov. 2022, ISSN: 1522-1598. DOI: `10.1152/jn.00259.2022`.

[66] J. Vlach, “Introduction to the theory and design of active filters,” *Proceedings of the IEEE*, vol. 70, pp. 314–314, Mar. 1982, Conference Name: Proceedings of the IEEE. DOI: `10.1109/PROC.1982.12302`.

[67] F. D. Farfán, J. C. Politti, and C. J. Felice, “Evaluation of EMG processing techniques using Information Theory,” *BioMedical Engineering OnLine*, vol. 9, p. 72, Nov. 2010, ISSN: 1475-925X. DOI: `10.1186/1475-925X-9-72`.

[68] M. van de Ruit *et al.*, “System identification: A feasible, reliable and valid way to quantify upper limb motor impairments,” *Journal of NeuroEngineering and Rehabilitation*, vol. 20, no. 1, p. 67, May 2023, ISSN: 1743-0003. DOI: `10.1186/s12984-023-01192-x`.

[69] A. L. Pando, H. Lee, W. B. Drake, N. Hogan, and S. K. Charles, “Position-dependent characterization of passive wrist stiffness,” *IEEE transactions on bio-medical engineering*, vol. 61, no. 8, pp. 2235–2244, Aug. 2014, ISSN: 1558-2531. DOI: `10.1109/TBME.2014.2313532`.

[70] A. C. Schouten, E. D. Vlugt, and F. C. T. van der Helm, “Design of perturbation signals for the estimation of proprioceptive reflexes,” *IEEE transactions on bio-medical engineering*, vol. 55, no. 5, pp. 1612–1619, May 2008, ISSN: 0018-9294. DOI: `10.1109/TBME.2007.912432`.

[71] M. M. Mirbagheri, K. Settle, R. Harvey, and W. Z. Rymer, “Neuromuscular abnormalities associated with spasticity of upper extremity muscles in hemiparetic stroke,” *Journal of Neurophysiology*, vol. 98, no. 2, pp. 629–637, Aug. 2007, ISSN: 0022-3077. DOI: `10.1152/jn.00049.2007`.

[72] S. S. SHAPIRO and M. B. WILK, “An analysis of variance test for normality (complete samples)†,” *Biometrika*, vol. 52, no. 3-4, pp. 591–611, Dec. 1965, ISSN: 0006-3444. DOI: `10.1093/biomet/52.3-4.591`.

[73] P. Welch, “The use of fast Fourier transform for the estimation of power spectra: A method based on time averaging over short, modified periodograms,” *IEEE Transactions on Audio and Electroacoustics*, vol. 15, no. 2, pp. 70–73, Jun. 1967, Conference Name: IEEE Transactions on Audio and Electroacoustics, ISSN: 1558-2582. DOI: `10.1109/TAU.1967.1161901`.

[74] J. Schuurmans, E. de Vlugt, A. C. Schouten, C. G. M. Meskers, J. H. de Groot, and F. C. T. van der Helm, “The monosynaptic Ia afferent pathway can largely explain the stretch duration effect of the long latency M2 response,” en, *Experimental Brain Research*, vol. 193, no. 4, pp. 491–500, Mar. 2009, ISSN: 1432-1106. DOI: `10.1007/s00221-008-1647-7`. [Online]. Available: `https://doi.org/10.1007/s00221-008-1647-7` (visited on 07/31/2024).

[75] I. L. Kurtzer, “Long-latency reflexes account for limb biomechanics through several supraspinal pathways,” *Frontiers in Integrative Neuroscience*, vol. 8, p. 99, Jan. 2015, ISSN: 1662-5145. DOI: `10.3389/fnint.2014.00099`. [Online]. Available: `https://www.ncbi.nlm.nih.gov/pmc/articles/PMC4310276/` (visited on 07/31/2024).

[76] H. van der Krogt *et al.*, “Comprehensive neuromechanical assessment in stroke patients: Reliability and responsiveness of a protocol to measure neural and non-neural wrist properties,” *Journal of Neuroengineering and Rehabilitation*, vol. 12, Mar. 2015. DOI: `10.1186/s12984-015-0021-9`.

[77] A. Geletu, “Solving Optimization Problems using the Matlab Optimization Toolbox - a Tutorial,” Dec. 2007.

[78] M. Kraska, *Encyclopedia of Research Design*. SAGE Publications, Inc., 2010, ISBN: 978-1-4129-6128-8. DOI: `10.4135/9781412961288`. [Online]. Available: `https://methods-sagepub-com.tudelft.idm.oclc.org/reference/encyc-of-research-design` (visited on 08/01/2024).

[79] S. W. Greenhouse and S. Geisser, “On methods in the analysis of profile data,” *Psychometrika*, vol. 24, no. 2, pp. 95–112, Jun. 1959, ISSN: 1860-0980. DOI: `10.1007/BF02289823`.

[80] J. W. Mauchly, “Significance Test for Sphericity of a Normal n-Variate Distribution,” *The Annals of Mathematical Statistics*, vol. 11, no. 2, pp. 204–209, Jun. 1940, Publisher: Institute of Mathematical Statistics, ISSN: 0003-4851, 2168-8990. DOI: `10.1214/aoms/1177731915`.

[81] V. Singh, R. K. Rana, and R. Singhal, “Analysis of repeated measurement data in the clinical trials,” *Journal of Ayurveda and Integrative Medicine*, vol. 4, no. 2, pp. 77–81, 2013, ISSN: 0975-9476. DOI: `10.4103/0975-9476.113872`.

[82] E. Park, M. Cho, and C.-S. Ki, “Correct Use of Repeated Measures Analysis of Variance,” *The Korean Journal of Laboratory Medicine*, vol. 29, no. 1, pp. 1–9, Feb. 2009, Publisher: The Korean Society for Legal Medicine. DOI: `10.3343/kjlm.2009.29.1.1`.

[83] A. Klomp, J. H. de Groot, E. de Vlugt, C. G. M. Meskers, J. H. Arendzen, and F. C. T. van der Helm, “Perturbation amplitude affects linearly estimated neuromechanical wrist joint properties,” *IEEE transactions on bio-medical engineering*, vol. 61, no. 4, pp. 1005–1014, Apr. 2014, ISSN: 1558-2531. DOI: `10.1109/TBME.2013.2290022`.

[84] T. R. Nichols and C. M. J. I. Huyghues-Despointes, “Muscular Stiffness,” in *Encyclopedia of Neuroscience*, M. D. Binder, N. Hirokawa, and U. Windhorst, Eds., Berlin, Heidelberg: Springer, 2009, pp. 2515–2519, ISBN: 978-3-540-29678-2. DOI: `10.1007/978-3-540-29678-2_3687`.

[85] T. R. Nichols and J. C. Houk, “Improvement in linearity and regulation of stiffness that results from actions of stretch reflex,” *Journal of Neurophysiology*, vol. 39, no. 1, pp. 119–142, Jan. 1976, Publisher: American Physiological Society, ISSN: 0022-3077. DOI: `10.1152/jn.1976.39.1.119`.

[86] R. C. van ’t Veld, E. H. F. van Asseldonk, H. van der Kooij, and A. C. Schouten, “Disentangling acceleration-, velocity-, and duration-dependency of the short- and medium-latency stretch reflexes in the ankle plantarflexors,” *Journal of Neurophysiology*, vol. 126, no. 4, pp. 1015–1029, Oct. 2021, Publisher: American Physiological Society, ISSN: 0022-3077. DOI: `10.1152/jn.00704.2020`.

[87] R. B. Stein and R. E. Kearney, “Nonlinear behavior of muscle reflexes at the human ankle joint,” *Journal of Neurophysiology*, vol. 73, no. 1, pp. 65–72, Jan. 1995, ISSN: 0022-3077. DOI: `10.1152/jn.1995.73.1.65`.

[88] M. P. Vlaar and A. C. Schouten, “System identification for human motion control,” English, in *Conference Record - IEEE Instrumentation and Measurement Technology Conference*, IEEE, May 2015, pp. 600–605. DOI: `10.1109/I2MTC.2015.7151336`.

[89] L. L. Van der Velden *et al.*, “Reliability and Validity of a New Diagnostic Device for Quantifying Hemiparetic Arm Impairments: An Exploratory Study,” *Journal of Rehabilitation Medicine*, vol. 54, jrm00283, May 2022, ISSN: 1651-2081. DOI: `10.2340/jrm.v54.12`.

A

Controller SEP

As used in previous research [61, 89], the SEP controller consisted of 4 control modes:

- **Voluntary active motion of the test-subject.** Only an anti-cogging controller is embedded in the Simulink to counteract the motor-cogging effect, allowing smooth rotation of the elbow joint in a voluntary motion.
- **Ramp-and-hold (RH) rotations of the elbow.** A position control mode is embedded in the Simulink model. A Proportional-Integral-Derivative (PID) controller is used, with an algorithm providing the option for either a $6\frac{deg}{sec}$ or a $100\frac{deg}{sec}$ RH-motion.
- **Maximum voluntary torque experiment.** The same PID controller as for the RH-motion is used, but with the reference rotation kept constantly at a 90-degree bend of the elbow.
- **Multisine torque perturbations.** No position controller is used, but a multisine torque signal is sent to the motor driver directly.

For the current experiments, a position controller able to perform a multisine rotational perturbation of the elbow joint was developped, as this was not yet present in the Simulink controller algorithm. This section describes the efforts to tune the control of the SEP to attain a flat power spectrum for multisine perturbations up to $10Hz$, of 2°-amplitude.

Two different options for control were considered:

- PID-controller implemented in the Simulink model, converting a position (or rotation angle) error to a desired motor torque sent to the HIWIN motor driver.
- Putting the HIWIN motor driver itself in velocity control mode, only providing a target velocity signal.

A.1. PID controller in Simulink

A PID controller previously designed for the RH-motion consisted of gains 4, 5, and 0.1, for the P-gain, I-gain and D-gain respectively. The large I-gain resulted in the desired controller behaviour in the RH-experiments but hindered adequate control in the multisine tracking. Without the I-gain, the relatively low P- and D-gain resulted in a decreasing power spectrum at higher frequencies, as shown in figure A.1.

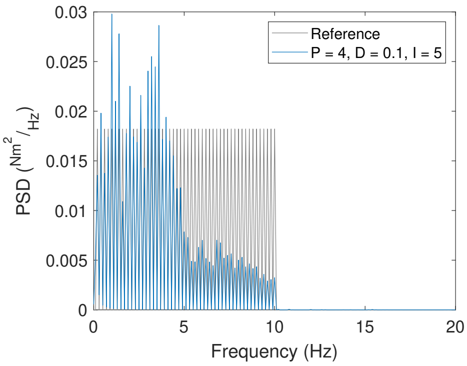

Figure A.1: PSD of actual perturbation signal as a result of a $0.2 - 10Hz$ multisine reference perturbation, for the initial SEP controller.

To increase power at higher frequencies two changes were implemented:

- An increased P-gain for higher controller stiffness.
- An increased D-gain to achieve adequate controller stability margins in the presence of high control stiffness.
- A feedforward component for D-gain, allowing feedforward control with the noise-less reference signal velocity.

These changes resulted in the controller shown in figure A.2.

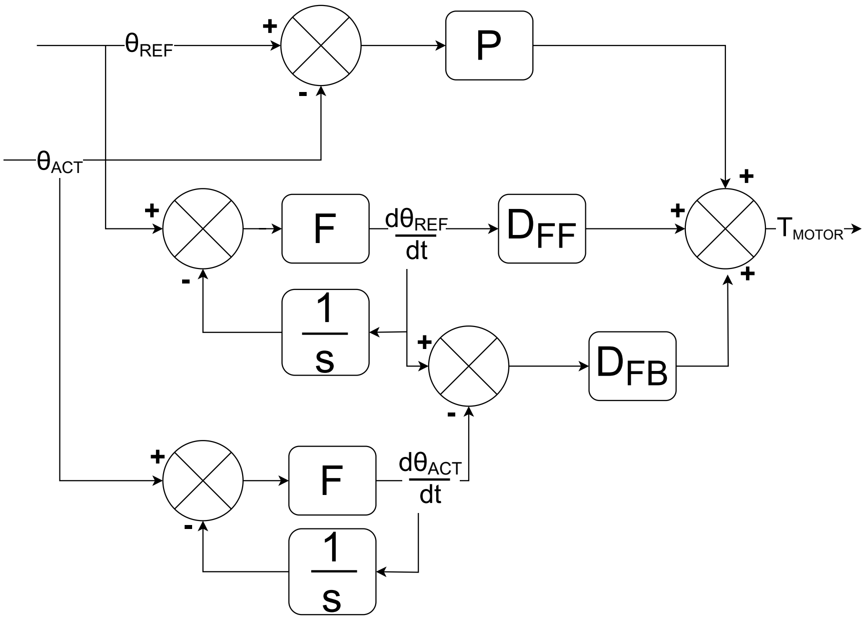

Figure A.2: A Proportional Derivative (PD)-controller converting a rotation angle error and the derivative thereof to a target torque, combined with feed forward derivative control.

The effect of the increased stiffness of the controller is visible in figure A.3a. The PSD at high frequencies increases, but the peak PSD at the new closed-loop resonance frequency increases as well. As also visible in figure A.3a, increasing the D-feedback gain reduces this peak.

However, the measured rotation angle signal sent from the motor encoder to the controller PC contained is slightly delayed and coarsly discretized. This caused inconsistencies in the derivative of the rotation angle signal, used for the derivative action. Therefore, feedback D-gain could not be further increased beyond ~ 0.25 before causing instability.

The addition of feed-forward D-gain allowed more derivative action uninfluenced by the noisy and discretised encoder signal. It also caused extra power for tracking signals with a high velocity without causing instability, as both seen by the increased power at high frequency in figure A.3b.

While this controller could be considered adequate, this method required intensive tuning to reach a stable controller. Furthermore, the stability margins remained small due to the inability to further increase damping. This resulted in the fact that any additional stiffness of the participants arm in the SEP-device, which is required for multiple trials, caused instability of the closed loop system. Tuning the control-parameters for every participant and every different activation level was not desired. Therefore, a different control strategy was employed.

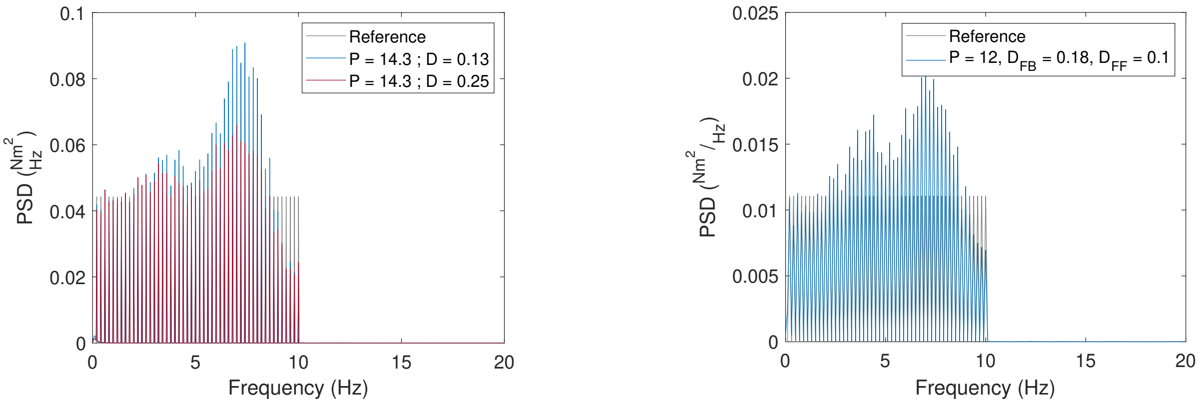

(a) The effect of increased stiffness and increased feedback damping on controller performance.

(b) The effect of increased feedforward damping on controller performance.

Figure A.3: Comparisons of PSDs of actual and reference perturbation signal. Showing the effect of different controller parameters.

A.2. HIWIN internal velocity control

The HIWIN motor drive features an internal PI-controller as well, converting a desired velocity input to a necessary motor torque using the HIWIN software. The internal velocity controller of the HIWIN has a more direct input of the motor encoder, less discretized and delayed, resulting in a smoother velocity signal for control. The internal HIWIN controller could thus be tuned stiffer, while retaining adequate stability through increased damping. This allowed adequate reference signal tracking even in the presence of a human joint resisting the perturbation.

Within the Simulink model, the derivative of the reference multisine perturbation was calculated and sent to the HIWIN controller. This derivative was calculated as a filter state of a first order LP-filter. The filter coefficient of the LP-filter was set high, at 100, to allow high frequency variations in velocity signal to be sent to the HIWIN controller.

Furthermore, as a velocity controller is susceptible to drift, a drift correction term was added. This consists of a multiplication of the rotation angle error with a gain, which gets added to the desired velocity. Tuning of the drift correction resulted in a rotation angle error gain of 2. The final controller configuration is shown in figure A.4.

The final controller performance for tracking a $10\ Hz$ bandwidth perturbation signal, while the SEP is loaded with a stiff arm, is shown in figure A.5. This performance appeared adequate for tracking the desired signal for the current experiments.

A.3. Conclusion

The final used controller is an internal velocity controller of the HIWIN driver, which tracks a velocity signal consisting of the differentiated reference rotation and a drift correction term.

Controller performance significantly increased compared to the initial controller settings, with the final controller set-up proving adequate for the current experiments. However, for further experiments and more demanding rotational perturbation signals, a more advanced control scheme is needed. This could be achieved with a high resolution rotary encoder and more advanced control schemes.

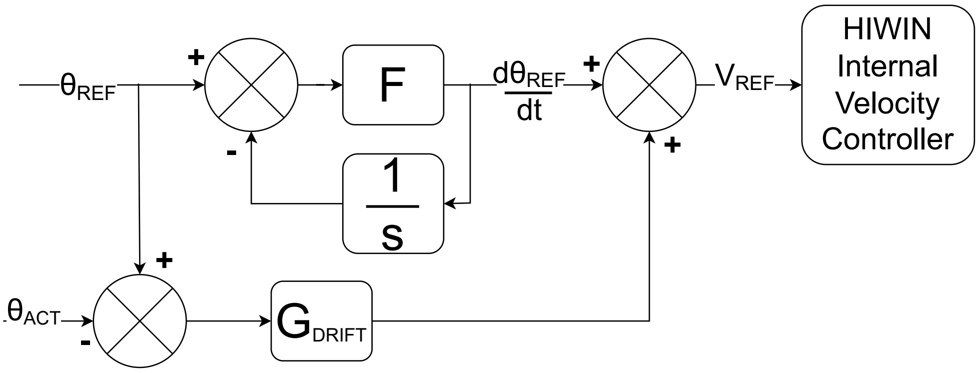

Figure A.4: The controller set-up making use of the HIWIN internal velocity controller.

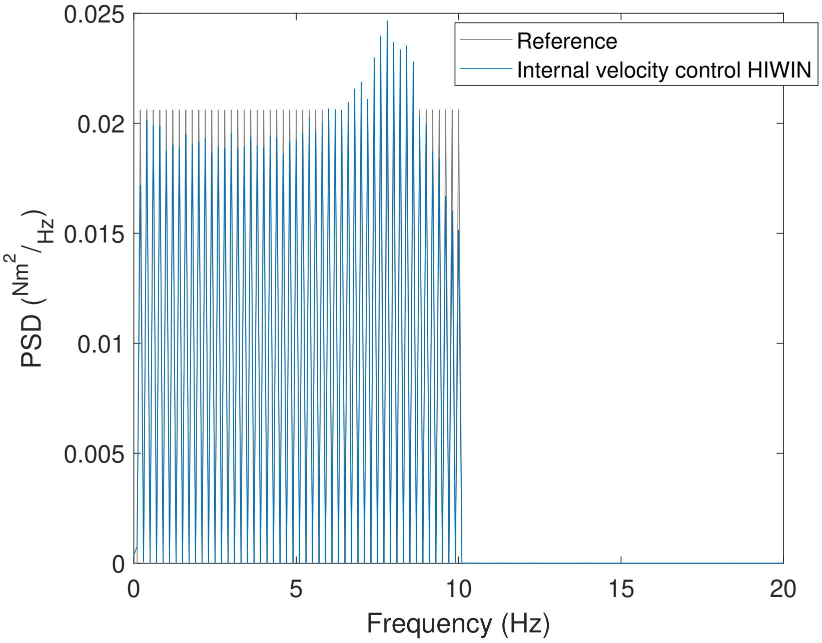

Figure A.5: A comparison of the PSDs of actual and reference perturbation signal, showing the final performance of the tuned internal HIWIN velocity controller.

B

Perturbation velocities in related research

OL-SID research uses a range of different perturbation types and velocities, which are theorised to affectthe nonlinear reflex response. Table B.1 shows an overview based on related literature of different perturbation types and the used velocity content. Optimal velocities for reflex induction are presented and an indication of whether an increased or decreased velocity is theorized to suppress reflexes is given. As a measure of average velocity over a perturbation, the Root Mean Square (RMS) of perturbation velocity is used. The small differences in velocity between articles using the same perturbation type were neglected, displaying one estimate of the average velocity content per type of perturbation.

For the multisine perturbations studies, as no explicit investigation of the effect of perturbation velocity on reflex response was performed, the average and maximum velocity of perturbation were not reported. These were estimated by regenerating the described perturbation signal in Matlab and calculating velocity through numerical differentiation.

Table B.1: Velocity content of different types of perturbation signals, taken from OL-SID literature.

Perturbation type	Avg. velocity	Max. velocity	Reflex reduction at ... velocities
Long RH stretches [47, 48]	$\sim 1.5\frac{rad}{s}$	$\sim 1.5\frac{rad}{s}$	Lower
Short RH stretches [57]	$\sim 0.5\frac{rad}{s}$	$\sim 0.5\frac{rad}{s}$	Higher
PRBS [34, 52, 56, 71]	$\sim 0.2\frac{rad}{s}$	$\sim 2\frac{rad}{s}$	Higher
Multisine [31, 33, 59]	$\sim 0.8\frac{rad}{s}$	$\sim 2.5\frac{rad}{s}$	Higher

C

Experimental protocol

C.1. Preparing experiment

The following steps are taken in preparation of the experiment. These ensure proper participant informed consent, adequate data saving and a safe testing environment.

- Turn on the SEP laptop and SEP at least 30 minutes before start of the experiment.
- Ensure the end-stops of the SEP are set at a 10 degree amplitude from the 170 degree centre position.
- Ensure both foam supports to relieve elbow and wrist discomfort are in place on the SEP.
- Ensure the emergency button is connected to the SEP device.
- Provide the participant with the printed experiment information and the informed consent file.
- Explain the experiment, allow for participant questions, request the participant to sign the consent form and store the signed consent safely.
- Assign a KEY to the participant and store this only within the KEY decipher file.
- Create a folder on the data transfer device (USB-stick) for the participant titled ’data_KEY’.
- Ensure adequate storage space on the laptop and correct date- and time-settings.

C.2. Setting up the experiment

C.2.1. Attaching EMG

- Find and mark electrode placement sites on the biceps brachii and triceps brachii muscle belly of the participant.
- Clean the placement sites with alcohol.
- Stick 1 EMG-electrode on the biceps brachii and 1 EMG-electrode on the triceps brachii of the participant. Place electrodes in line with muscle fibre direction.
- Stick the reference electrode on the elbow of the participant.
- Connect the EMG-electrodes and reference electrode to the amplifier.
- Connect the amplifier to the 2 BNC analogue input channels of the SEP.

C.2.2. Positioning subject in the SEP

- Station a stable and non-rolling seat next to the SEP for the participant and position the torso of the participant next to the centre of rotation of the elbow on the SEP.
- Adjust the height of the SEP to ensure approximately 80 degrees of shoulder abduction when the elbow and underarm are supported by the SEP.
- Strap the emergency button around the leg of the participant.
- Place the underarm of the patient on the device, with the medial epicondyle of the elbow on the centre of rotation of the SEP and the wrist in the clamp distal of the underarm support. Tighten the wrist clamp as tight as possible without causing discomfort to the participant.

C.2.3. Setting up the software

- Start the DLS-manager through the Linux command prompt.
- Set-up the data saving folder in the command prompt.
- Start the SEP interface program in TestManager.
- Set the virtual endstops of the SEP to 155-185 in the TestManager interface.
- Set the ’Filter gain’ and ’Drift gain’ as seen in figure A.4 to 100 and 2 respectively.
- Start the motor drive in the TestManager interface.

C.3. The MVC experiment

- Start the motor in the TestManager interface.
- Start MVC experiment in the TestManager interface.
- Ask participant to flex their elbow joint as at maximum effort for 5 seconds.
- Set MVC biceps level in the TestManager interface.
- Ask participant to relax their elbow joint for 5 seconds.
- Ask participant to fully extend their elbow joint for 5 seconds.
- Set MVC triceps level in the TestManager interface.
- Ask participant to fully relax their elbow joint for 5 seconds.
- Set baseline activation level in the TestManager interface.

C.4. The perturbation experiment

C.4.1. Initiating experiment

- Start motor in the TestManager interface.
- Choose and set perturbation signal from the six signals described in table 2.1, through selecting the correct column in the TestManager interface.
- Choose and set activation level in the TestManager interface.
- Reset driver state.
- Start a measurement in the DLS software.
- Start experiment in the TestManager interface.

Saving experiment data

- Stop experiment in the TestManager interface.
- Stop data logging in the DLS software.
- Save data from through running the data-saving script in the command window.

D

Device report SEP

INSPECTION REPORT FOR DEVICES TO BE USED IN CONNECTION WITH HUMAN SUBJECT RESEARCH

This report should be completed for every experimental device that is to be used in interaction with humans and that is not CE-certified or used in a setting where the CE certification no longer applies[1].

The first part of the report has to be completed by the researcher and/or a responsible technician.

Then, the safety officer (Heath, Security and Environment advisor) of the faculty responsible for the device has to inspect the device and fill in the second part of this form. An actual list of safety-officers is provided on this webpage.

Note that in addition to this, all experiments that involve human subjects have to be approved by the Human Research Ethics Committee of TU Delft. Information on ethics topics, including the application process, is provided on the HREC website.

Device identification (name, location): Shoulder Elbow Perturbator (SEP)
Located in F-1-180 in the ME faculty.

Configurations inspected[2]: NA

Type of experiment to be carried out on the device:[3] Human experiments with simple motor control tasks for the upper extremity.

Name(s) of applicants(s): Mark van de Ruit

Job title(s) of applicants(s): Assistant professor BmechE

(Please note that the inspection report should be filled in by a TU Delft employee. In case of a BSc/MSc thesis project, the responsible supervisor has to fill in and sign the inspection report.)

Date: 09/04/2024

Signature(s):

---

[1] Modified, altered, used for a purpose not reasonably foreseen in the CE certification

[2] If the devices can be used in multiple configurations, otherwise insert NA

[3] e.g. driving, flying, VR navigation, physical exercise, ...

Setup summary

The SEP (fig. 1), produced by Hankamp Rehab B.V., is a device used for perturbation of the elbow joint. The device requires strapping the under-arm to a splint. The splint then gets rotated around the elbow joint by a torque-motor, that is controlled through EtherCAT software, with the controller built in a MATLab Simulink environment.

The height of the splint, and thus the elbow joint during evaluation, is variable. The participant can lift their elbow through shoulder abduction while splinted to the device. The amount of loading support for this abduction can be varied through an adjustable spring mechanism.

Previously, the SEP was approved for usage in the Erasmus MC and Rijndam Revalidatie Centrum for assessing the elbow joint impedance of patients with upper motor neuron lesion. The approval was given by the Medical Ethical Committee of the Erasmus MC, among other things based on the device description in the IMDD of the SEP. This IMDD contains a full device description (**Appendix 1**), risk assessment (**Appendix 2**) and risk mitigation strategy (**Appendix 3**). The most relevant device aspects and risks for the current experiment are explicitly listed in this device report.

The approval was given for usage of the SEP in 3 control conditions:

- Position control. A PID controller in the software converts a positional input signal to a motor torque. This motor torque is applied to the human arm.
- Torque control. A torque signal is directly exerted by the torque motor to the human arm.
- Free motion, controlled by the participant. The device is turned on, but no torque is applied to the participant's arm.

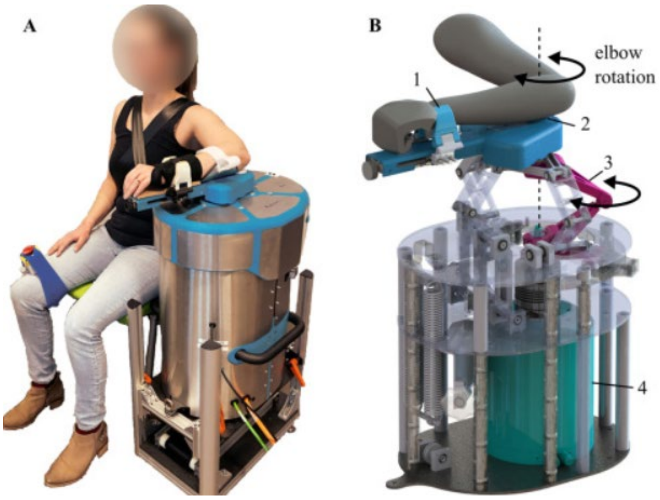

Figure 1: The SEP-device, A) in use, B) internal mechanics. Taken from [van der Velden et al. 2022]

Participants can be asked to keep specific shoulder abduction levels in combination with an elbow flexion angles or torque, while the device rotates the elbow joint. During this, the angular rotation of the elbow and the elbow torque are measured. This allows for the assessment of motor control of the elbow joint.

The experiments with the SEP at the TU Delft will involve healthy participants, that is; participants without neurological injury or current injuries of the elbow joint according to self-report.

The SEP is located in the corner of the 'NeuroMuscular Control laboratory' with enough wall clearance to safely rotate the splint with the attached arm of the participant. The device is placed securely on the floor and cannot accidentally move or shift due to its' weight.

Safety mechanisms:

The device has multiple implemented safety stops:

- *Software* - Rotation limits: Virtual end-stops limiting rotation of the splint past a certain pre-set angle are present.
- *Software* - Force limits: When a certain limit torque is needed to rotate the split, further rotation of the splint is halted. This limit torque can be adjusted for different experiments.
- *Software* Velocity limits: Within the position control, a rate limiter for rotation speed is set up.
- *Hardware* - Mechanical stops limiting rotation of the splint. These can be set at a chosen rotation angle.
- *Electrical* - There is an emergency button attached to the device. This emergency button remains within reach of both the participant and the researcher at all times. When pressed, the power supply to the torque motor is halted.

Device inspection

(to be filled in by the AMA advisor of the corresponding faculty)

Name: Maarten Lugt

Faculty: Mechanical Engineering

The device and its surroundings described above have been inspected. During this inspection I could not detect any extraordinary risks.

(Briefly describe what components have been inspected and to what extent (i.e. visually, mechanical testing, measurements for electrical safety etc.)

The device has been shown, including all safety measures. Discussed that an additional layer of foam (or other soft material) will be included in the wrist-pads.

Date: 29-04-2024

Signature:

Inspection valid until[4]: 29-04-2027

Note: changes to the device or set-up, or use of the device for an experiment type that it was not inspected for require a renewed inspection

---

[4] Indicate validity of the inspection, with a maximum of 3 years

Risk checklist

Please fill in the following checklist and consider these hazards that are typically present in many research setups. If a hazard is present, please describe how it is dealt with.
Also, mention any other hazards that are present.

Hazard type	**Present**	**Hazard source**	**Mitigation measures**
Mechanical (sharp edges, moving equipment, etc.)	X	The rotating splint to which the participant's arm is attached, could rotate too far or too fast, causing discomfort, pain or injury to the participant.	Multiple safety stops are present within the software to prevent too fast, painful or too far rotation: - Rotation limits - Force limits - Velocity limits
Electrical	X	Due to electrical malfunction, sensor malfunction or software malfunction, the safety stops that are built into the software could fail. This could lead to over-rotation of the elbow joint.	In case of a malfunction of the virtual safety stops, there are set mechanical end-stops to prevent over-rotation of the elbow joint.
Electrical	X	Motor malfunction, running out of control.	If the motor runs out of control, the low-level controller goes into a corresponding ‘error state’. The motor can then coast. Furthermore, an emergency button is present to halt the power supply to the motor at all times.
Structural failure	X	The mechanical end-stops can break if the splint is rotated with a very high force.	The software's built-in torque limit should prevent excessive force on the end-stops. In the case of both software end-stops and mechanical end-stops failing, there is a described emergency button attached to the device.
Other: Human factor	X	Virtual end-stops can be set incorrectly by the researcher, due to insufficient knowledge of flexion and extension angle definitions.	The set mechanical end-stops can resist over-rotation of the elbow. These can be used more intuitively. Furthermore, the input rotation signal will not contain large rotation angles.
Other: Human factor	X	The mechanical end-stops can be set incorrectly or forgotten by the researcher.	The setting of the end-stops is taken up into the protocol. End-stops are not removed in between trials to reduce the chance of forgetting to replace them.

			Furthermore, the input rotation signal will not contain large rotation angles.
Touch Temperature	-		
Electromagnetic radiation	-		
Ionizing radiation	-		
(Near-)optical radiation (lasers, IR-, UV-, bright visible light sources)	-		
Noise exposure	-		
Materials (flammability, offgassing, etc.)	-		
Chemical processes	-		
Fall risk	-		
Other:			
Other:			
Other:			

E

Participant information

Participant information elbow perturbation study

Dear participant,

You are invited to participate in the study called ‘System identification of the elbow joint with the “Shoulder Elbow Perturbator” (SEP) device’. This is a study conducted by Karien ter Welle (master student Mechanical Engineering), supervised by Arno Stienen (Assistant professor BmechE department at the TU Delft) and Mark van de Ruit (Assistant professor BmechE department at the TU Delft).

Study objective

This study is looking at a way to better understand the impedance of elbow joints by using a technique called system identification (SI) in the frequency domain. Joint impedance generally describes the resistance of a joint to an external perturbation. When people have damage to certain nerves in their upper body, like after a stroke, it can affect their joint stiffness and their reflex responses to joint movement. The SEP device uses perturbation of the elbow joint and measurements of the response to perturbation to identify this changed joint impedance. This study aims to validate the usage of the SEP device to perform such system identification in healthy participants. Eventually, this could lead to clinical usage of this device for diagnostics in patients with upper motor neuron lesions.

What is expected of you?

During the session of approximately 60 minutes of work, you will undergo positional perturbations of the elbow joint during different experimental conditions. The positional perturbations will be a multi-sinusoidal signal, which means that they will feel like a random oscillation of your elbow joint. Within all experimental conditions, it is requested that you attempt to **not resist the perturbation**.

During the experiment, your arm will be strapped into the SEP-device, shown in figure 1. The fixation of your arm within the device should be as firm as possible without causing discomfort. While you are seated next to the device, your strapped-in arm will be perturbed by the SEP.

The experiment consists of three different phases:

- In the first experiment phase no perturbation will be used. Instead, you are asked to generate as much force as possible in the elbow flexion direction, while strapped into the device.
- In the second experiment phase you will rest your arm fully supported on the SEP device and attempt to fully relax your arm. Perturbations with different multisinusoidal signals will take place and measurements of your response will be taken.
- In the third experiment phase you will be asked to generate different levels of elbow flexion, while the perturbation takes place. It is requested to not resist the perturbation, but instead maintain a steady elbow flexion level at all times. The flexion level of the elbow will be provided to you through visual feedback, such that you can maintain the required level of flexion during the experiment. The experiment will be repeated for different required levels of elbow flexion.

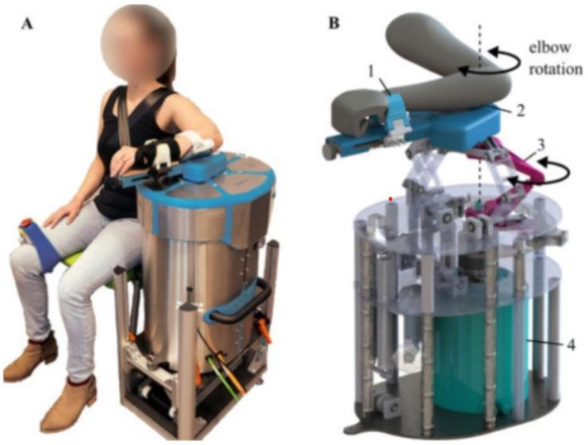

Figure 1: The SEP device in use (left) and a mechanical drawing of the SEP device (right) taken from [van der Velden et al., 2022]

<u>What data will be acquired?</u>

During the first phase of the experiment, the maximum flexion force that you can generate will be saved as data. During the perturbation trials, the torque signal that you exert on the device in the presence of the perturbation will be saved as data. The positional perturbation signal will be saved as well. These two signals together will be analyzed to determine your joint's impedance response to the perturbation. Furthermore, EMG-measurements will be taken of two muscles responsible for stretching and flexing the elbow. EMG measurements are measurements of the electrical activity of muscles and can be used to detect muscle activity. These measurements are taken non-invasively with three conductive stickers on your arm.

<u>What happens to the data?</u>

Your data will be anonymised with a unique number, thereby dissociating the data from directly identifiable information such as your name. After one week, the document linking your EMG, torque or position data to your name will be deleted. This means that upon request, you can only have your data deleted in the first week after the experiment, as after this period it will be untraceable. The data will be used for research that may result in publication in an international scientific journal.

To reduce the possibility that your age and gender lead to your re-identification, your exact age will not be stored. Instead, you will be assigned to an ‘age-group’ (e.g. 18-25, 25-35 etc.). Your age group and gender will be stored together with the EMG-, torque- and position data, to use for further research.

<u>What are the risks associated with this study?</u>

This device perturbes your elbow-joint by moving the under-arm. In case of a device malfunction the possibility arises of overstretching the elbow joint. However, the device has multiple safety mechanisms built-in to prevent this overstretching from happening:

- Virtual end-stops within the software, shutting down the motors at certain rotation angles of the joint.

- Mechanical end-stops within the device, not allowing the device to rotate the elbow joint further than the mechanical end-stop location.
- A safety button in reach of both you and the researcher at all times during the experiment. Pressing this safety button shuts down the motors immediately

If you are experiencing elbow pain or currently have an elbow injury, the perturbations could lead to serious discomfort or even pain. Therefore, in the case of an elbow injury you are not allowed to participate in this study.

EMG measurements are without risk. Such measurements have been performed on patients in hospitals and in research settings for years, with no known harmful effects.

F

Consent form

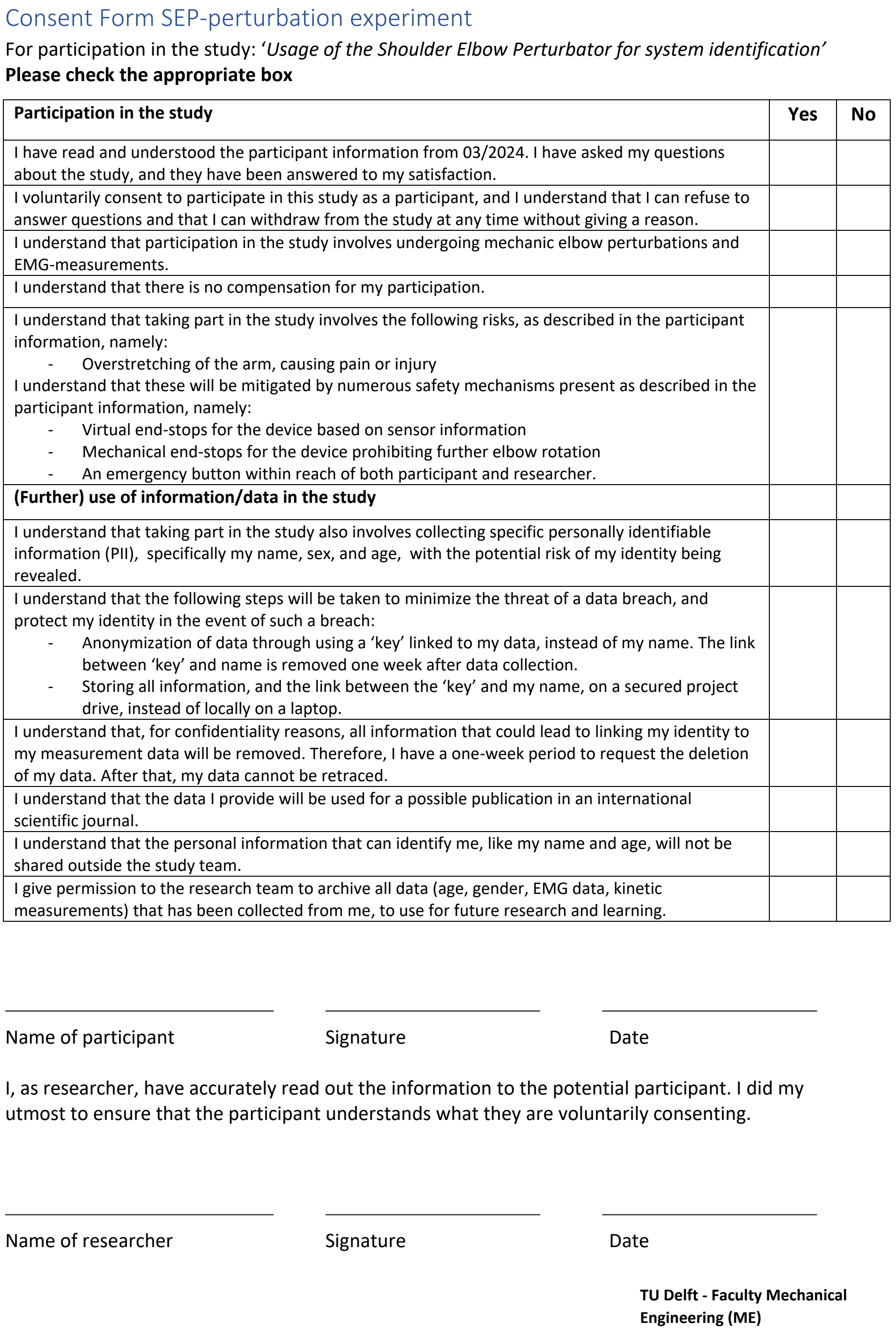

Consent Form SEP-perturbation experiment

For participation in the study: ‘*Usage of the Shoulder Elbow Perturbator for system identification’*

Please check the appropriate box

Participation in the study	**Yes**	**No**
I have read and understood the participant information from 03/2024. I have asked my questions about the study, and they have been answered to my satisfaction.		
I voluntarily consent to participate in this study as a participant, and I understand that I can refuse to answer questions and that I can withdraw from the study at any time without giving a reason.		
I understand that participation in the study involves undergoing mechanic elbow perturbations and EMG-measurements.		
I understand that there is no compensation for my participation.		
I understand that taking part in the study involves the following risks, as described in the participant information, namely: - Overstretching of the arm, causing pain or injury I understand that these will be mitigated by numerous safety mechanisms present as described in the participant information, namely: - Virtual end-stops for the device based on sensor information - Mechanical end-stops for the device prohibiting further elbow rotation - An emergency button within reach of both participant and researcher.		
(Further) use of information/data in the study		
I understand that taking part in the study also involves collecting specific personally identifiable information (PII), specifically my name, sex, and age, with the potential risk of my identity being revealed.		
I understand that the following steps will be taken to minimize the threat of a data breach, and protect my identity in the event of such a breach: - Anonymization of data through using a ‘key’ linked to my data, instead of my name. The link between ‘key’ and name is removed one week after data collection. - Storing all information, and the link between the ‘key’ and my name, on a secured project drive, instead of locally on a laptop.		
I understand that, for confidentiality reasons, all information that could lead to linking my identity to my measurement data will be removed. Therefore, I have a one-week period to request the deletion of my data. After that, my data cannot be retraced.		
I understand that the data I provide will be used for a possible publication in an international scientific journal.		
I understand that the personal information that can identify me, like my name and age, will not be shared outside the study team.		
I give permission to the research team to archive all data (age, gender, EMG data, kinetic measurements) that has been collected from me, to use for future research and learning.		

Name of participant   Signature   Date

I, as researcher, have accurately read out the information to the potential participant. I did my utmost to ensure that the participant understands what they are voluntarily consenting.

Name of researcher   Signature   Date

TU Delft - Faculty Mechanical Engineering (ME)

G

Intitial and boundary values for fitting

Table G.1 shows the used initial values and upper and lower boundaries used in minimising the error function in the fitting procedure (eq. 2.12), with the ’lsqnonlin’ solver in MATLAB. The used inertia, stiffness and damping initial and boundary values were the same for the model consisting of intrinsic and reflexive impedance (IR-model) and the model consisting of only intrinsic impedance (I-model). The k_v parameter was only fit in the IR-model.

Table G.1: Table of the initial values and upper and lower boundaries used for minimising the error function in equation 2.12 with the ’lsqnonlin’ solver, for both the I- and IR-model.

Parameter	Initial value	Lower boundary	Upper Boundary
Interia $\frac{Nm \cdot s^2}{rad}$	0.2	0	1
Stiffness (k_{int}**)** $\frac{Nm}{rad}$	10	0	100
Damping (b_{int}**)** $\frac{Nm \cdot s}{rad}$	0.5	0	2
Reflex gain (k_v) $\frac{Nm \cdot s}{rad}$	0.5	0	2

H

Estimation of the bandwidth of infinite contact dynamics

Using the block scheme depicted in figure 2.3a, the transfer function from θ_{pert} to θ_{elbow} can be derived. As long as the contact impedance is adequately stiff, the transfer function between these two should equal ~ 1.

θ_{elbow} is derived as follows:

$$\theta_{elbow} = \frac{T_{handle} \cdot H_{INT}}{1 + H_{REF} \cdot H_{INT}}. \tag{H.1}$$

Substituting the relation

$$T_{Handle} = (\theta_{pert} - \theta_{elbow}) \cdot H_{CON}, \tag{H.2}$$

into equation H.1, gives:

$$\theta_{elbow} = \frac{\theta_{pert} \cdot H_{CON} \cdot H_{INT}}{1 + H_{REF} \cdot H_{INT}} - \frac{\theta_{elbow} \cdot H_{CON} \cdot H_{INT}}{1 + H_{REF} \cdot H_{INT}}, \tag{H.3}$$

resulting in

$$(1 + \frac{H_{CON} \cdot H_{INT}}{1 + H_{REF} \cdot H_{INT}}) \cdot \theta_{elbow} = \frac{H_{CON} \cdot H_{INT}}{1 + H_{REF} \cdot H_{INT}} \cdot \theta_{pert}. \tag{H.4}$$

This can be further derived to an expression of relation between θ_{pert} and θ_{elbow}:

$$\begin{aligned} \frac{\theta_{pert}}{\theta_{elbow}} &= \frac{1 + \frac{H_{CON} \cdot H_{INT}}{1 + H_{REF} \cdot H_{INT}}}{\frac{H_{CON} \cdot H_{INT}}{1 + H_{REF} \cdot H_{INT}}} \\ &= \frac{1 + H_{REF} \cdot H_{INT}}{H_{CON} \cdot H_{INT}} + 1 \\ &= \frac{\frac{1}{H_{INT}} + H_{REF}}{H_{CON}} + 1 \end{aligned} \tag{H.5}$$

Using the models described by equations 2.10 and 2.11 for H_{INT} and H_{REF} respectively, equation H.5 can be changed to:

$$\frac{\theta_{pert}}{\theta_{elbow}} = \frac{m \cdot s^2 + (b_{int} + k_v) \cdot s + k_{int}}{H_{CON}} + 1 \tag{H.6}$$

where s is the Laplace operator and m, b_{int}, k_{int}, and k_v are the inertia, intrinsic damping, intrinsic stiffness and reflex gain respectively. As previous research with the SEP did not include a k_v parameter, it is set to 0 for the current analysis. An estimation of the other parameters can be taken from previous research by van de Ruit *et al.* [68], resulting in values of $0.11\frac{Nm\cdot s^2}{rad}$, $2\frac{Nm\cdot s}{rad}$, and $50\frac{Nm}{rad}$ for m, b_{int}, and k_{int} for the activated elbow joint.

The contact dynamics of the SEP, H_{CON}, was also modelled in the same research, as an impedance function of:

$$H_{CON} = 4 \cdot s + 340. \tag{H.7}$$

Combining equations H.6 and H.7 and filling in all numerical values gives:

$$\frac{\theta_{pert}}{\theta_{elbow}} = \frac{0.11 \cdot s^2 + 6 \cdot s + 390}{4 \cdot s + 340} \tag{H.8}$$

As the transfer function from θ_{pert} to θ_{elbow} is the inverse of equation H.8, the final transfer function equals.

$$\frac{\theta_{elbow}}{\theta_{pert}} = \frac{4 \cdot s + 340}{0.11 \cdot s^2 + 6 \cdot s + 390} \tag{H.9}$$

When assessing the contact dynamics as a low pass filter, the bandwidth can be determined through numerical solving of

$$|H_{\theta_E \theta_P}| = 0.707, \tag{H.10}$$

where $H_{\theta_E \theta_P}$ is the FRF from θ_{pert} to θ_{elbow}, as depicted in equation H.9, and 0.707 is a common magnitude value used for determining filter cut-off frequencies. Numerically solving H.10 with $s = j \cdot \omega$ results in a cut-off frequency 'ω_c'of $13.9Hz$.

It must however be noted that the transfer function never has the value of 1, but rather takes the value of $\frac{340}{390} = 0.87$ at the low frequency limit.

I

EMG signal - Bessel filter versus moving Root Mean Square

To ensure the reliability of the first order Bessel filter in assessing online EMG-data, a comparison to the often-used moving RMS filter was performed. The moving RMS filter used a moving window of 1-second duration, so a length of 1000 samples. Figure I.1 shows a comparison between the Bessel and RMS filtered signals, during a MVC experiment and a perturbation trial.

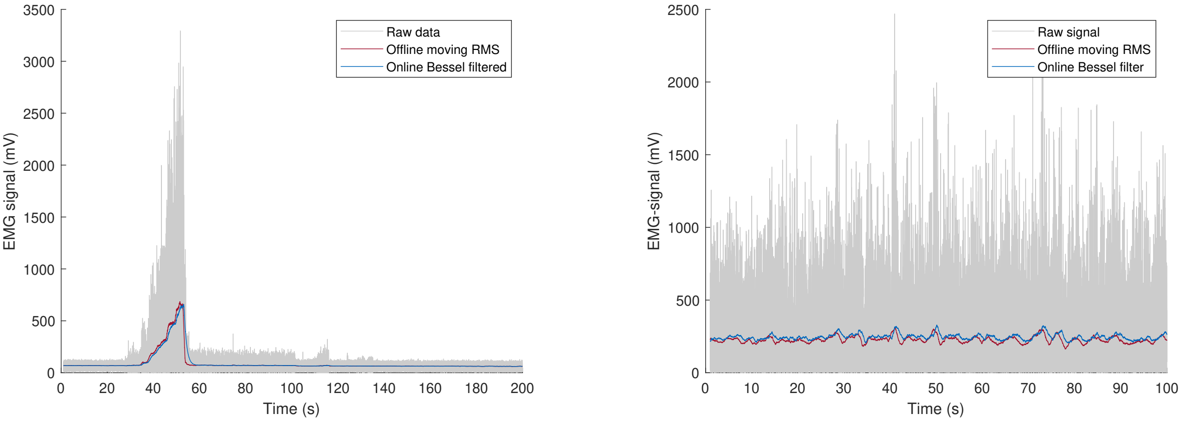

(a) Example of both filters for an MVC trial.

(b) Example of both filters for a 30% MVC trial.

Figure I.1: Visual comparison between the offline Root Mean Square (RMS) filter and online first order Bessel filter.

For 7 participants, both the offline and online filtered Bessel EMG data was available, allowing quantitative comparison between the online Bessel filter and offline moving RMS filter. This was evaluated by comparing the different 'rest' and 'MVC' EMG signal levels found when using the different filters. Table I.1 shows the estimated MVC and relax activation level using the online Bessel filter and offline moving RMS filter, as an indication of the magnitude of differences caused by different filter usage. The average of absolute difference between filters is small, at only 5% of measured signal magnitude in MVC, and 0.44% in rest.

Table I.1: Difference in MVC EMG-signal, between Bessel filtered and moving average filter, for 7 subjects with raw EMG data available. An average of the absolute percentual deviation is provided.

Bessel MVC (mV)	RMS (mV)	Difference	Bessel Relax (mV)	RMS Relax (mV)	Difference
791.5	721.5	-9.7%	28.4	28.6	-0.5%
344.7	330.8	-4.2%	83.5	83.3	+0.2%
1145.5	1135.5	+0.9%	20.0	20.1	-0.6%
520.5	581.4	-11.7%	36.2	35.9	+0.9%
535.4	558.8	-4.4%	45.2	45.3	-0.3%
659.4	663.9	0.7%	62.2	62.0	+0.4%
307.0	316.6	-3.1%	50.8	50.7	+0.2%
		AVG $= 4.9\%$			**AVG** $= 0.44\%$

J

EMG signal - Normalization and drift

During the experiment, the EMG signal measured during full relaxation drifted. This drift was corrected by resetting the 'relax' normalisation value in between trials. Table J.1 shows used values for normalization per participant, and gives an indication of the relative magnitude of EMG drift compared to the full EMG-signal normalisation range.

Table J.1: EMG signal at rest and during MVC, used as normalisation range, together with the drift in the EMG signal that was corrected during the experiment. Drift is also depicted as a percentage of the total EMG-signal normalised range between rest and MVC.

MVC (mV)	**Relax (mV)**	**Range (mV)**	**Drift (mV)**	**Drift percentage (-)**
535	50.5	485	33	6.8%
939	44	895	0	0%
540	73	467	34	7.3%
307	88	219	67	30.7%
330	45	285	58	20.4%
659	25	634	25	3.9%
381	60	321	43	13.4%
622	21	601	0	0%
540	40	500	0	0%
593	47	546	20	3.7%
721	33	688	0	0%
520	35	485	0	0%
902	57	845	0	0%
264	50	214	21	9.8%
577	57	520	68	13.1%
567	40	527	0	0%
AVG $= 562$	**AVG** $= 47.9$	**AVG** $= 514.5$	**AVG** $= 23.1$	**AVG** $= 6.8\%$

K

EMG signal - Normal distributions

Figure K.1 shows the distribution of muscle activation across trials for at three different target activation levels. The 0% MVC target activation shows two outliers at large negative activation values. Since negative activation values are physiologically impossible, these are attributed to uncorrected EMG signal drift. This drift occurred because the manual correction by the examiner was performed only between trials, allowing some EMG drift during the long trials. These two outliers were removed for assessing normality of distribution as they were known false measurements.

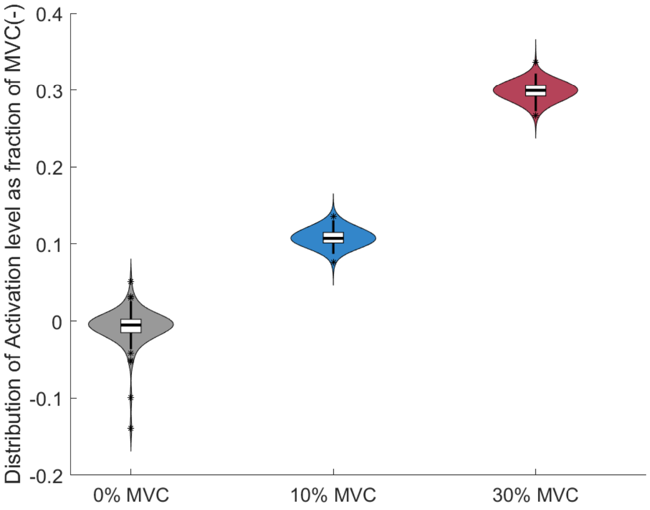

Figure K.1: Violin plots of the distribution of activation levels over different trials and participants. Activation levels are given as fraction of MVC.

Normality of the distribution was assessed using the Shapiro-Wilk test. As three activation levels were analysed, the critical value was set at $\alpha = 0.05/3 = 0.0167$ through a Bonferroni correction. A p-value smaller than this critical value indicates that the null-hypothesis that the data is normally distributed should be rejected. As shown in table K.1, this was the case for none of the different target activation levels.

Table K.1: Outcome of the Shapiro-Wilk test for normality of the muscle activation for different participants, at different target activation levels. Critical p-value for normality was set at $\alpha = 0.0167$.

Target activation	P-value Shapiro-Wilk test	Normality (1= normal, 0= not normal)
0% MVC	0.022	1
10% MVC	0.72	1
30% MVC	0.091	1

L

EMG signal - Trial exclusion

The exclusion for trials based on activation level as explained in section 2.6.1 is visualised in figure L.1. A total of 14 trials was excluded for the average activation deviating more than $2 \cdot SD$ from the group average. Additionally, 18 trials were excluded for activation deviating more than $3 \cdot SD$ from group average for longer than 5 seconds. For the 0% MVC trials, only the upper boundaries were used for exclusion.

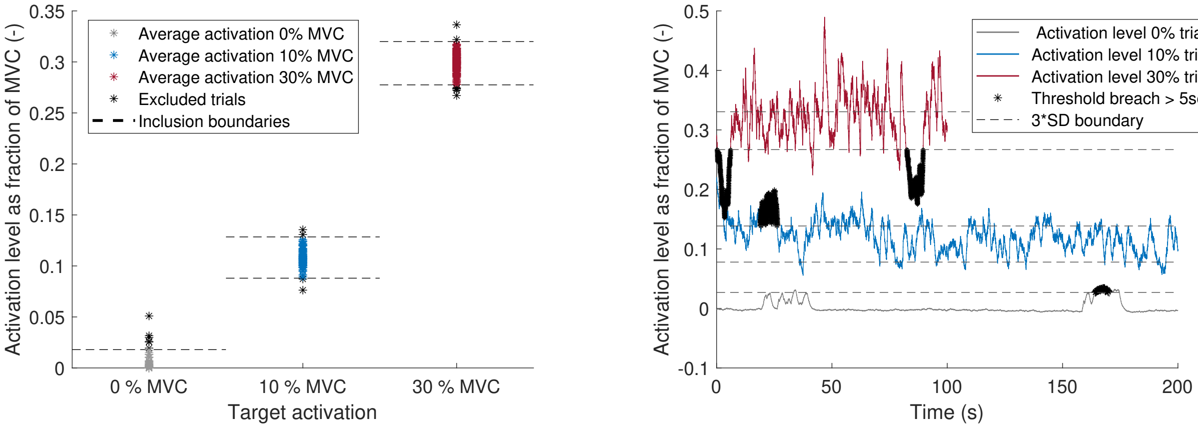

(a) Excluded trials based on the avg. EMG level deviating more than $2 \cdot SD$ from group average (or more than $2 \cdot SD$ above 0 for the 0% MVC trials).

(b) Example of 3 excluded trials (0%, 10%, and 30%) excluded based on deviating more than $3 \cdot SD$ from group average for more than 5 seconds.

Figure L.1: Visualisation of the two trial exclusion criteria based on EMG signal.

M

Tracking analysis

Figure M.1 shows a visual representation of tracking of a desired angular perturbation of the elbow joint by the SEP controller. Table M.1 quantifies the tracking performance in the time domain, providing RMSE values between the reference perturbation signal and the actual achieved elbow angle. Table M.2 shows the quantified tracking performance in the frequency domain. The frequency response function between the reference and actual achieved elbow joint angle would equal 1 at all perturbed frequencies for perfect tracking. The overshoot at $\sim 7Hz$ and subsequent drop at the highest frequencies are quantified as the average maximum and minimum values of the FRF magnitude, averaged across different participants.

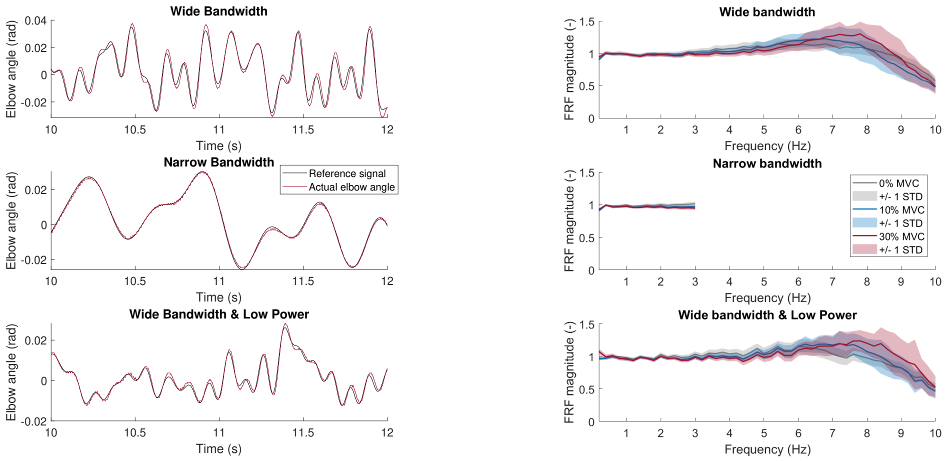

(a) Reference signal tracking in the time domain for an exemplary trial at 30% MVC.

(b) Average FRF from reference to actual joint angle for an exemplary trial at 30% MVC.

Figure M.1: Performance in desired perturbation signal tracking of the SEP controller, both in time and frequency domain.

Table M.1: Average [$\pm SD$] Root Mean Square Error (RMSE) in degrees, between reference and actual perturbation angle.

	0% MVC	**10%** MVC	**30% MVC**
WB	0.11 [±0.04]	0.15 [±0.05]	0.16 [±0.05]
NB	0.03 [±0.006]	0.04 [±0.008]	0.05 [±0.01]
WB LP	0.06 [±0.01]	0.07 [±0.02]	0.07 [±0.02]

Table M.2: Max. and min. [$\pm SD$] magnitude of the Frequency Response Function (FRF) from reference to actual perturbation angle.

		0% MVC	**10% MVC**	**30% MVC**
WB	*Max FRF mag.*	1.21 [±0.10]	1.36 [±0.16]	1.42 [±0.19]
	Min FRF mag.	0.58 [±0.08]	0.48 [±0.08]	0.48 [±0.12]
NB	*Max FRF mag.*	1.02 [±0.02]	1.00 [±0.02]	1.00 [±0.02]
	Min FRF mag.	0.90 [±0.01]	0.90 [±0.01]	0.92 [±0.02]
WB LP	*Max FRF mag.*	1.21 [±0.11]	1.33 [±0.15]	1.40 [±0.17]
	Min FRF mag.	0.52 [±0.07]	0.46 [±0.09]	0.51 [±0.17]

N

Estimation of impedance of the unloaded SEP

Figure N.1 shows the FRF of the SEP identified without any loading (no arm condition), with the different perturbation signals. The parameter values for fitting an inertia-stiffness-damping model to the FRFs are shown in table N.1. It can be seen that the impedance is not the same when identified with different perturbation signals. Coherence is relatively high for the SEP without load, indicating the reduced torque noise in the signal compared to the trials with a human elbow joint.

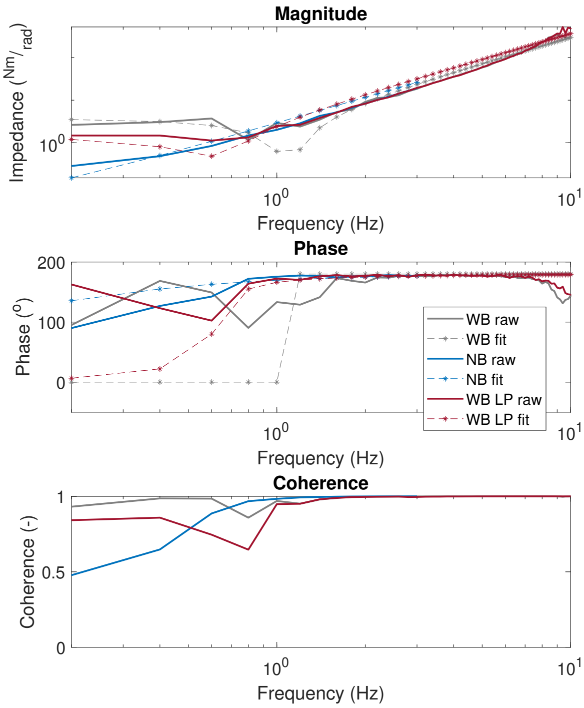

Figure N.1: Estimation of the impedance of the unloaded SEP. Showing magnitude and phase of the FRF and the coherence between input rotation and output torque. The fitted impedance models to these FRFs (inertia, stiffness, damping) are shown in the dotted lines.

Table N.1: Parameter values obtained when fitting model to the unloaded SEP FRF, consisting of inertia, stiffness, and damping.

	WB	**NB**	**WB LP**
$I(\frac{Nm\cdot s^2}{rad})$	0.076	0.074	0.093
$B(\frac{Nm\cdot s}{rad})$	0.00	0.081	0.092
$K(\frac{Nm}{rad})$	3.36	0.014	1.34

O

Exemplary fits of the IR-model

Figures O.1, O.2, and O.3 show an example of the fitting procedure of the IR-model for different signals at 0%, 10%, and 30% respectively. For further insight, the intrinsic and reflexive component of the IR-model are separated. It can be observed that as activation level increases, the reflex component of the impedance model increases as well.

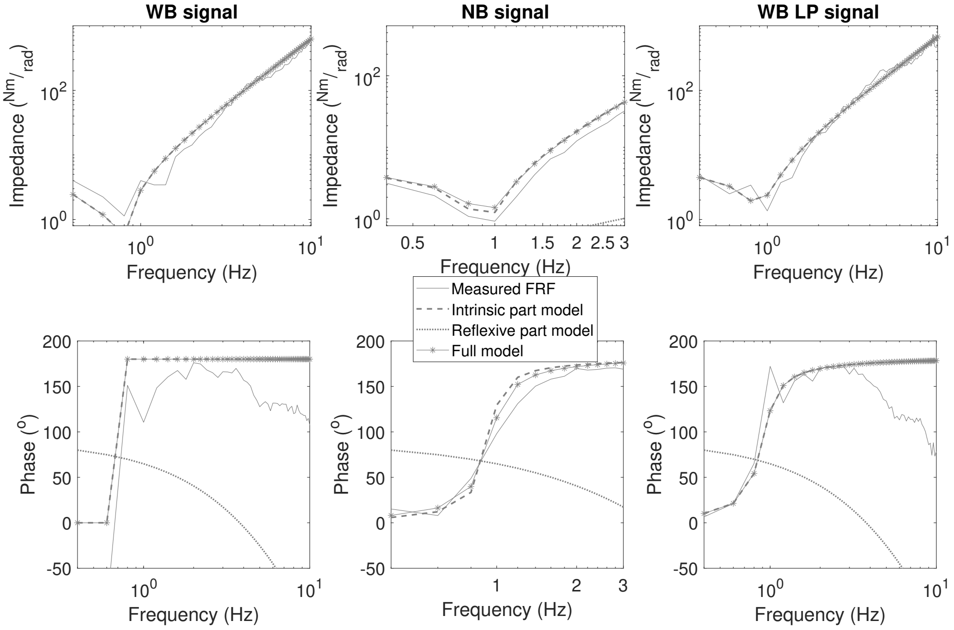

Figure O.1: Exemplary fit of the IR-model for different perturbation types at 0% MVC activation level.

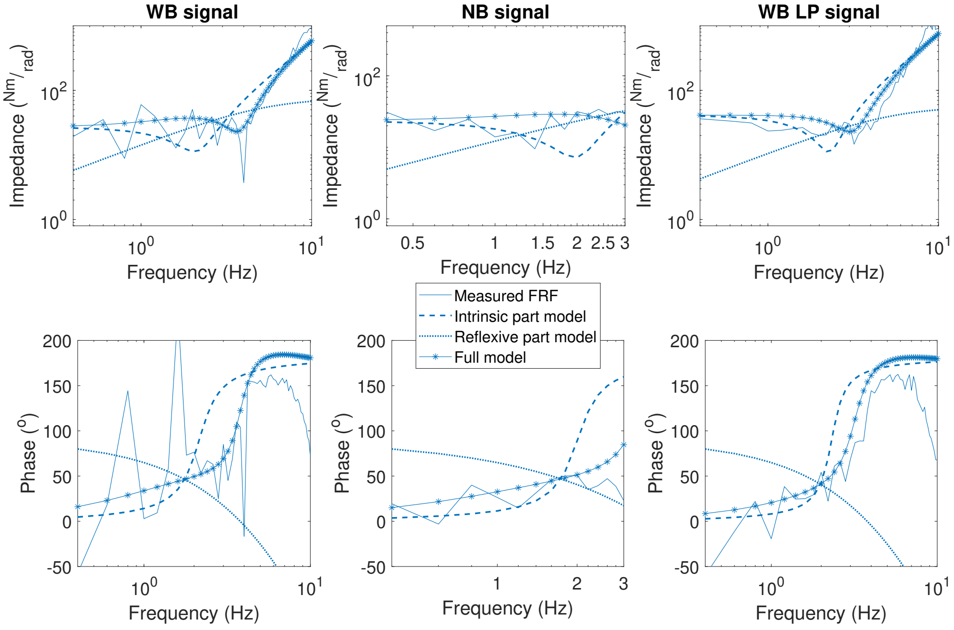

Figure O.2: Exemplary fit of the IR-model for different perturbation types at 10% MVC activation level.

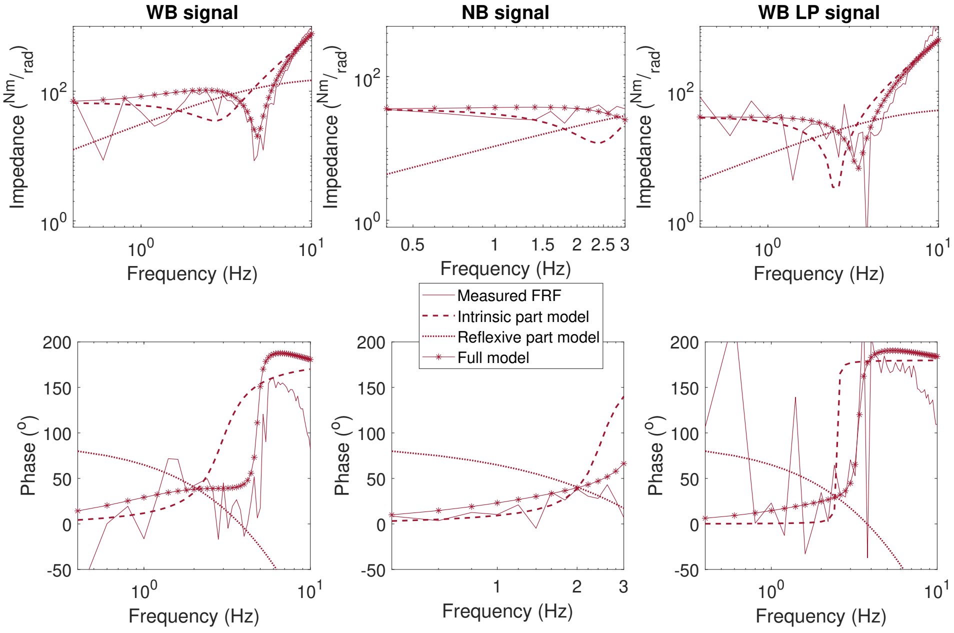

Figure O.3: Exemplary fit of the IR-model for different perturbation types at 30% MVC activation level.

P

Average fits of the I- and IR-model

Figures P.1, P.2, and P.3 show the average model fits of 0%, 10%, and 30% MVC trials respectively, for different perturbation signals. A comparison is made between the I-model and IR-model fits. It can be observed that as activation level increases, the I-model and IR-model fits start to deviate.

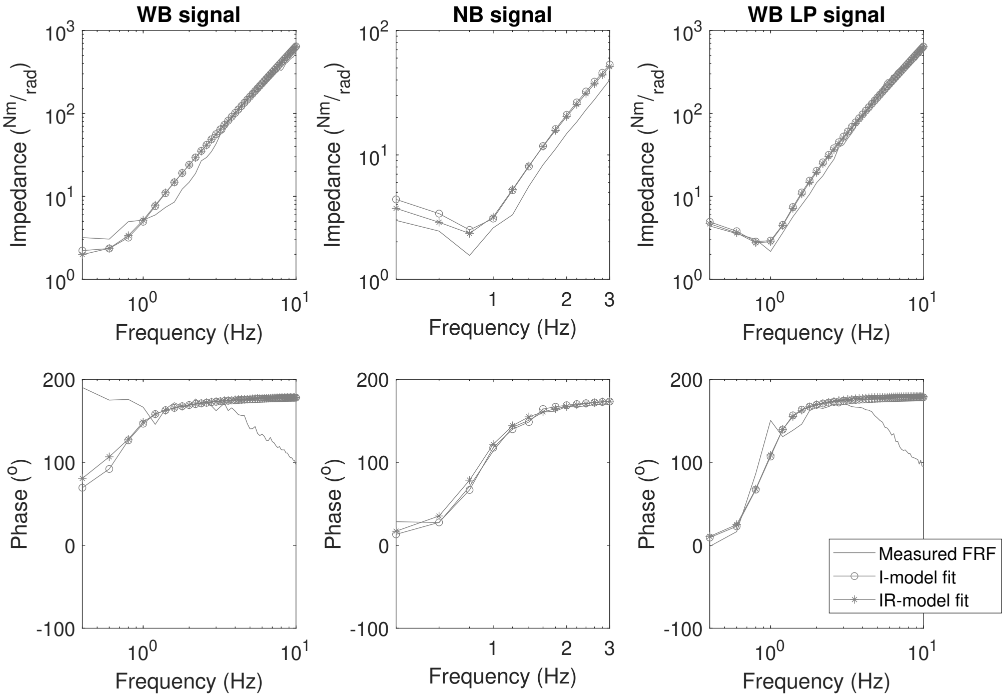

Figure P.1: Average fits for the I- and IR-model for 0% MVC trials for different perturbation types.

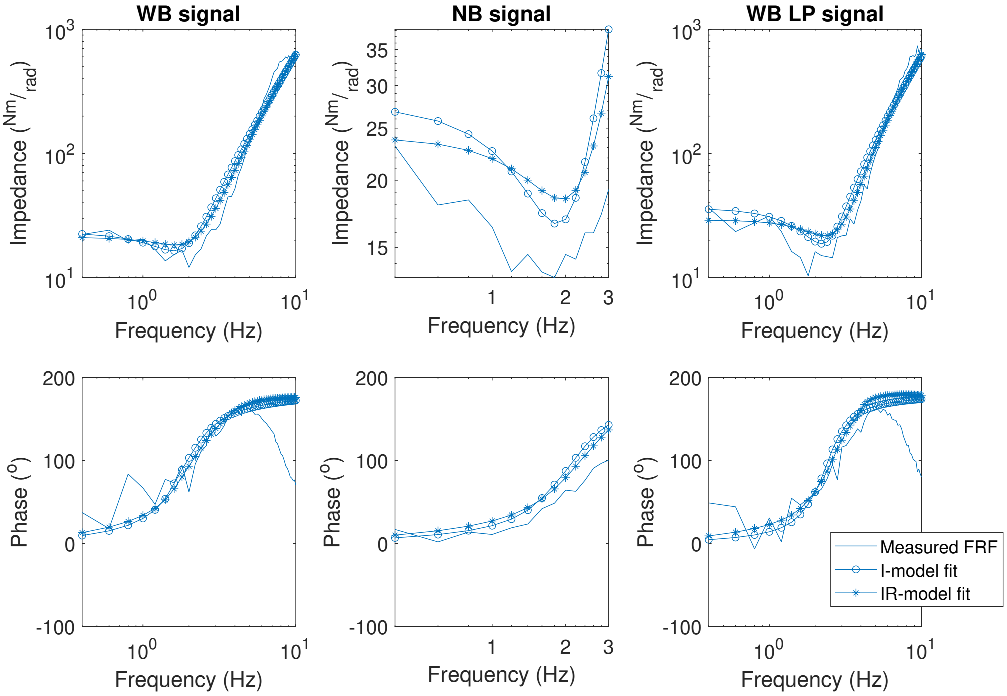

Figure P.2: Average fits for the I- and IR-model for 10% MVC trials for different perturbation types.

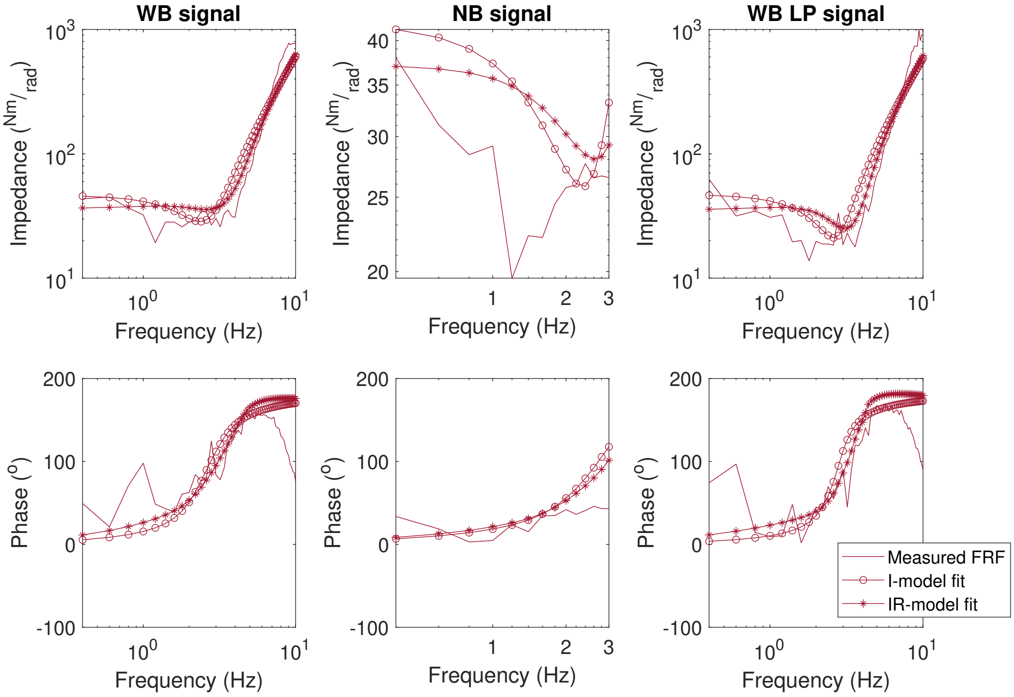

Figure P.3: Average fits for the I- and IR-model for 30% MVC trials for different perturbation types.

Q
Model fit in time domain

Figure Q.1 shows an exemplary fit of the modelled torque to the measured torque for the I- and IR-model for different perturbation signals for 30% MVC activation. Only slight differences can be identified in the fits, consistent with the small changes in VAF shown in 3.1. The largest difference can be seen for the NB-perturbations.

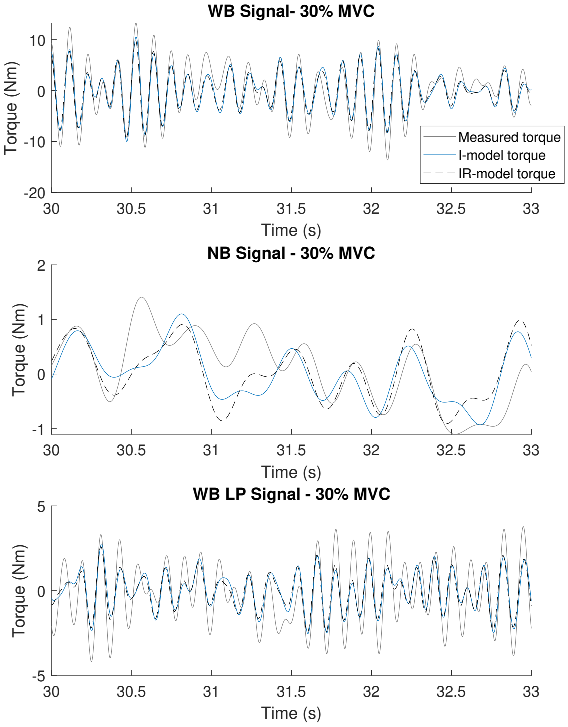

Figure Q.1: Exemplary comparison of the measured and modelled torque in the time domain, for trials at a 30% MVC activation level with different perturbation types.

R

Fitted parameters - Statistical comparison of two signal realisations

Tables R.1, R.2, and R.3 show the p-value outcomes of the t-test comparison between the two different realisations of the same signal (sig.1&2, sig.3&4, and sig.5&6, as described in sec. 2.4). As described in section 2.7 the critical value was set at $\alpha = 0.0167$. A p-value below this critical value would imply a rejection of the null hypothesis that there is no difference between the fitted parameters for the different signal types. This was the case in none of the comparisons. As no damping parameter was fit for the NB perturbation, these results are missing in table S.2.

Table R.1: P-values for the t-test comparing intrinsic stiffness fitted for impedance identified with the two different realisations of the same signal. Critical value was set at $\alpha = 0.0167$.

	0% MVC	10% MVC	30% MVC
WB	0.30	0.46	0.68
NB	0.22	0.98	0.03
WB LP	0.03	0.81	0.71

Table R.2: P-values for the t-test comparing intrinsic damping fitted for impedance identified with the two different realisations of the same signal. Critical value was set at $\alpha = 0.0167$.

	0% MVC	10% MVC	30% MVC
WB	0.20	0.08	0.28
NB	-	-	-
WB LP	0.69	0.76	0.72

Table R.3: P-values for the t-test comparing reflex gain fitted for impedance identified with the two different realisations of the same signal. Critical value was set at $\alpha = 0.0167$.

	0% MVC	10% MVC	30% MVC
WB	0.44	0.74	0.04
NB	0.06	0.04	0.27
WB LP	0.50	0.08	0.95

S

Fitted parameters - Normal distribution

Figure S.1 shows the distribution of the different fitted parameters for all trials in a violin plot, combining distribution density overlayed with a boxplot.

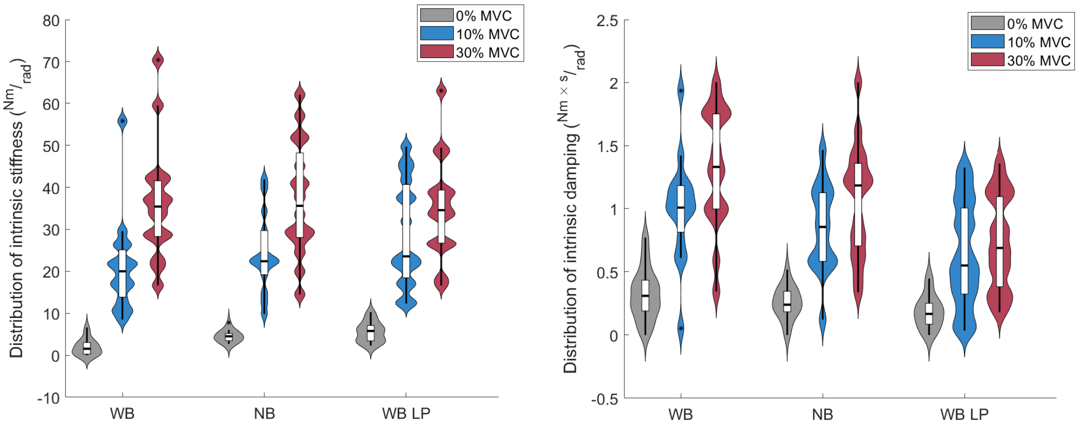

(a) Violin plot showing the distribution of k_{int} for different perturbation signals and activation levels.

(b) Violin plot showing the distribution of k_{int} for different perturbation signals and activation levels.

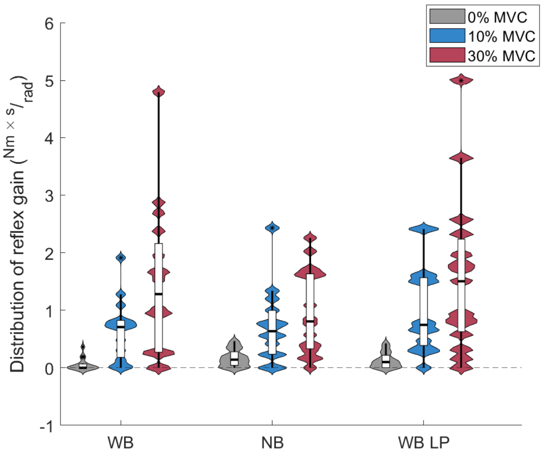

(c) Violin plot showing the distribution of k_{int} for different perturbation signals and activation levels.

Figure S.1: Distribution densities combined with boxplots, showing the fitted intrinsic parameters for the different perturbation signal types and activation levels.

Tables S.1, S.2, and S.3 show the p-value outcomes of the Shapiro-Wilk test for normality. As discussed in section 2.7, the critical value was determined at $\alpha = 0.0167$. A p-value below this critical value would imply a rejection of the null hypothesis that the fit values for a parameter for a specific activation level and perturbation type is normally distributed across participants. This was the case for k_{int} at the WB 10% MVC trial, and for k_v at the WB 0% MVC trial. Looking at the violin plots in S.1 it appears the former is caused by one extreme outlier and the latter by the fact that a excessively large part of the distribution is centred at $k_v = 0$ which reduces the normality of the distribution.

Table S.1: P-values for the assessment of a normal distribution for k_{int} with the Shapiro-Wilk test. Critical value was set at $\alpha = 0.0167$.

	0% MVC	**10% MVC**	**30% MVC**
WB	0.04	0.005	0.14
NB	0.32	0.31	0.89
WB LP	0.41	0.18	0.65

Table S.2: P-values for the assessment of a normal distribution for b_{int} with the Shapiro-Wilk test. Critical value was set at $\alpha = 0.0167$.

	0% MVC	**10% MVC**	**30% MVC**
WB	0.87	0.33	0.41
NB	0.95	0.90	0.89
WB LP	0.37	0.62	0.46

Table S.3: P-values for the assessment of a normal distribution for k_v with the Shapiro-Wilk test. Critical value was set at $\alpha = 0.0167$.

	0% MVC	**10% MVC**	**30% MVC**
WB	$2 \cdot 10^{-5}$	0.21	0.10
NB	0.14	0.07	0.15
WB LP	0.03	0.11	0.13

T

Statistical analysis

Table T.1 shows the results of the Mauchly test for sphericity and the RM-ANOVA. As indicated in section 2.7 the critical value for the Mauchly test was $\alpha = 0.0167$. If the resulting p-value was below this critical value, the sphericity assumption was violated. In these cases, a Greenhouse Geisser correction factor was calculated, with which the p-value for the RM-ANOVA was corrected. The critical value for the RM-ANOVA was set at $\alpha = 0.05$. The RM-ANOVA results show statistical significance for the effect of activation level on all parameters for all perturbation types.

Table T.2 shows the results of the post hoc analysis, performed to investigate specific effects of activation level increments on fitted parameters. The post hoc analysis consisted of a one-tailed t-test with Bonferonni correction resulting in a critical value of $\alpha = 0.0167$. Almost all activation level increments showed significant increase of the fitted parameters, except for k_{int} and b_{int} for the 10% MVC to 30% MVC increment for the WB LP perturbation, and k_v for the 10% MVC to 30% MVC increment for the NB perturbation.

Table T.1: Results of the Mauchly test for sphericity, and the Repeated Measures (RM) ANOVA. Critical value for the Mauchly test was set at $\alpha = 0.0167$. Critical value for the RM ANOVA was set at $\alpha = 0.05$.

		p-value Mauchly	**Greenhouse Geisser correction**	**F test statistic RM-ANOVA**	**p-value RM-ANOVA**
WB	k_{int}	0.21	-	72.15	$8.95 \cdot 10^{-12}$
	b_{int}	0.31	-	47.68	$9.74 \cdot 10^{-10}$
	k_v	0.0062	0.65	14.39	$6.6 \cdot 10^{-4}$
NB	k_{int}	0.44	-	70.85	$2.99 \cdot 10^{-11}$
	b_{int}	0.015	0.68	46.27	$3.75 \cdot 10^{-7}$
	k_v	0.87	-	13.36	$1.02 \cdot 10^{-4}$
WB LP	k_{int}	0.18	-	36.52	$2.81 \cdot 10^{-8}$
	b_{int}	0.081	-	21.98	$2.58 \cdot 10^{-6}$
	k_v	0.032	0.69	16.01	$3 \cdot 10^{-4}$

Table T.2: Results of the post hoc one-tailed t-test for all fitted parameters, all perturbation signal types and all activation level increments. A Bonferonni correction was applied resulting in a critical value of $\alpha = 0.0167$.

		0% vs. 10%		**0% vs 30%**		**10% vs 30%**	
		Mean diff. [95% CI]	p-value	Mean diff. [95% CI]	p-value	Mean diff. [95% CI]	p-value
WB	k_{int}	19.21 [12.81-25.43]	$7.03 \cdot 10^{-6}$	34.36 [27.22-41.49]	$1.76 \cdot 10^{-8}$	13.60 [9.28-17.93]	$4.69 \cdot 10^{-6}$
	b_{int}	0.71 [0.48-0.94]	$6.04 \cdot 10^{-6}$	1.00 [0.76-1.24]	$1.32 \cdot 10^{-7}$	0.29 [0.11-0.47]	$1.8 \cdot 10^{-3}$
	k_v	0.59 [0.29-0.90]	$4.9 \cdot 10^{-4}$	1.39 [0.72-2.07]	$2.7 \cdot 10^{-4}$	0.88 [0.21-1.54]	$7.0 \cdot 10^{-3}$
NB	k_{int}	19.50 [14.57-24.44]	$5.46 \cdot 10^{-7}$	32.72 [25.94-39.49]	$1.71 \cdot 10^{-8}$	12.06 [6.47-17.64]	$2.2 \cdot 10^{-4}$
	b_{int}	0.61 [0.42-0.79]	$2.93 \cdot 10^{-6}$	0.82 [0.59-1.04]	$5.63 \cdot 10^{-7}$	0.20 [0.08-0.32]	$1.5 \cdot 10^{-3}$
	k_v	0.54 [0.18-0.90]	$3.2 \cdot 10^{-3}$	0.80 [0.43-1.17]	$1.5 \cdot 10^{-4}$	0.34 [-0.01-0.70]	0.029
WB LP	k_{int}	23.60 [17.08-30.12]	$9.65 \cdot 10^{-7}$	29.87 [23.18-36.55]	$7.92 \cdot 10^{-8}$	6.58 [-2.78-15.94]	0.076
	b_{int}	0.46 [0.25-0.67]	$1.81 \cdot 10^{-4}$	0.55 [0.36-0.74]	$1.05 \cdot 10^{-5}$	0.07 [-0.06-0.19]	0.12
	k_v	0.89 [0.51-1.27]	$8.57 \cdot 10^{-5}$	1.47 [0.73-2.22]	$4.2 \cdot 10^{-4}$	0.75 [0.13-1.36]	0.01

U

Fitting results allowing for negative k_v

In the primary fitting analysis, the lower bound for the parameter k_v is set at 0. This implies that the stretch-reflexes are only 'excitory', thus causing a resistance force based due to a stretching of the muscle spindles. It prohibits the 'inhibitory' stretch reflex, where a stretch of the spindles would cause a decrease in force or even a force in the stretch direction. This inhibitory stretch reflex is not physiologically common, but it is interesting to observe the behavior of the fitted parameters when this negative k_v value is allowed.

Figure U.1 shows the resulting fit values for k_v when the lower parameter bound is set at -5 $\frac{Nm \cdot s}{rad}$ instead of 0. It can be observed that the trend of increase in k_v with increased activation level does not change compared to the primary analysis (fig. U.1b). However, there are a lot of negative k_v values present in the individual fits (fig. U.1a), even causing negative average k_v values for the 0% MVC activation level (fig. U.1b).

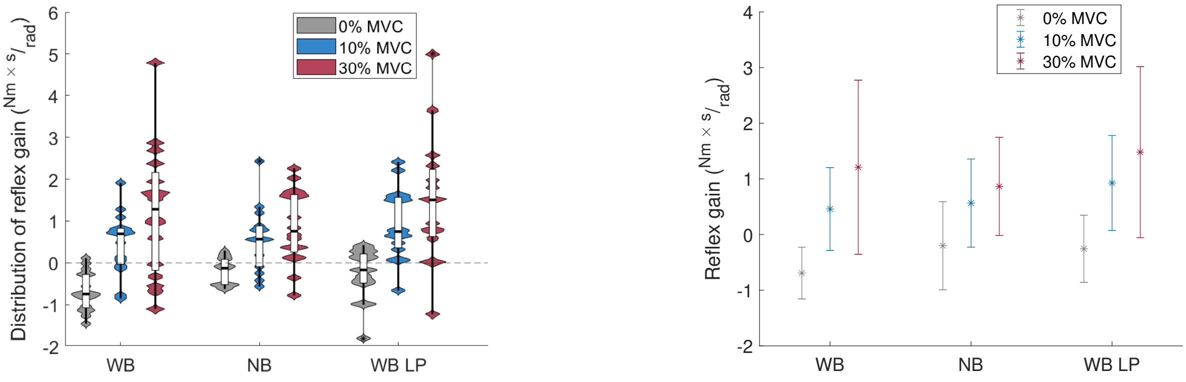

(a) Violin plot.

(b) Mean and SD.

Figure U.1: Distribution visualisations for k_v when the parameter is allowed to take on a negative value.

Figure U.2 shows what a fit with a negative k_v value looks like in a 0% and 30% MVC trial. As the magnitude is insensitive to sign, the magnitude of the reflexive part of the model, is comparable to the fits of the primary analysis. However, the phase shows a $\sim 180°$ difference to that of the fits with positive k_v. This causes the intrinsic and reflexive impedance to be out of phase before the natural frequency, causing a subtraction of the reflexive impedance from the intrinsic impedance, and in phase after the natural frequency, causing an addition of the reflexive impedance. This is opposite to what is observed when fitting with a positive k_v.

For 0% MVC a negative reflex gain is somewhat comprehensible. The very low impedance at the full relax trials can be mimicked by the model using inhibitory reflex responses. Lowering the intrinsic stiffness or adding a negative k_v have a similar effect, thus the slightly unpredictable fitting procedure can result in either of these outcomes.

For the 30% MVC trial in figure U.2 the negative k_v is harder to explain. It appears that the added reflex gain does not necessarily improve the fit. One possibility is a local minimum of the fitting solver algorithm, as the initial k_v value starts close to 0 and could thus converge to a negative value. Furthermore, the measured FRF shows large variance from frequency to frequency, in both the phase and magnitude. This erratic fluctuation makes the fit more unpredictable, as it could converge to either the higher values or the lower values of the measured FRF.

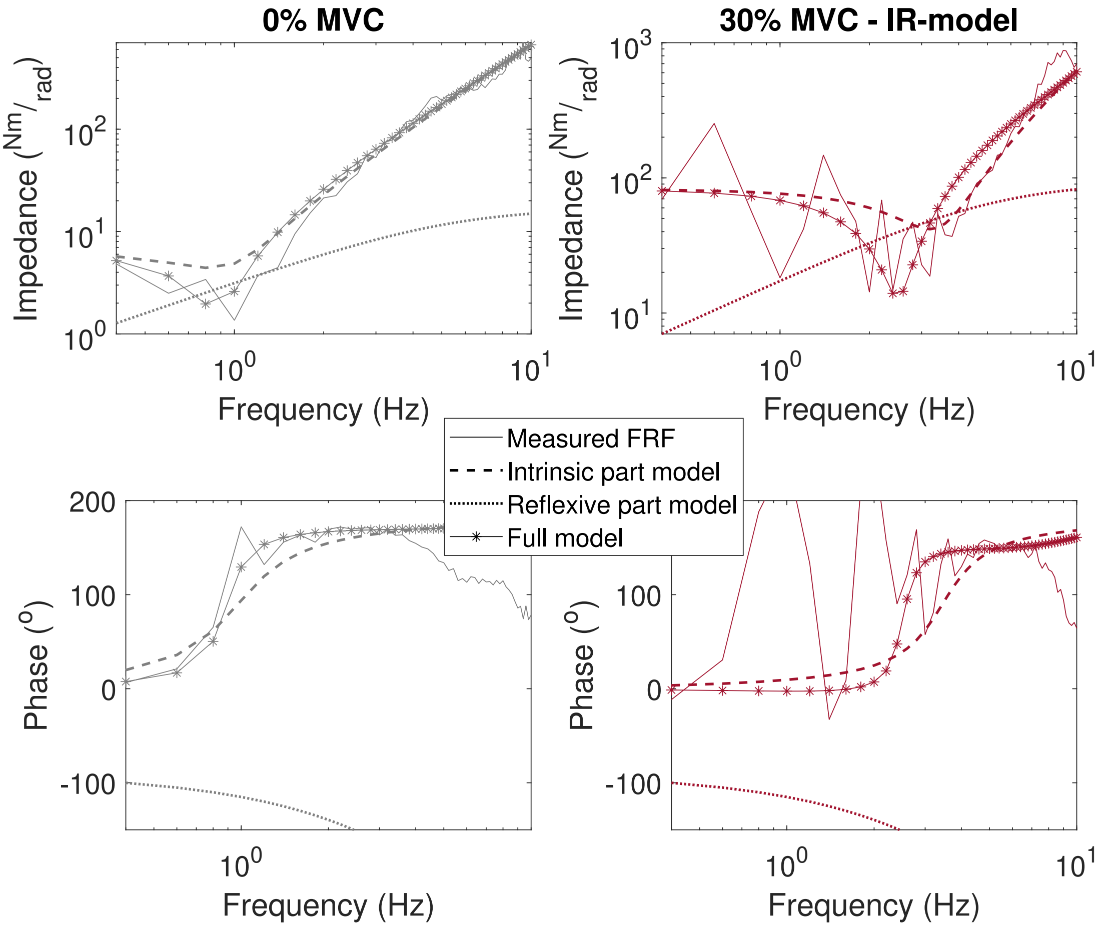

Figure U.2: A 0% and 30% fit with negative values of k_v.

These findings stress the importance of two things. First, that an effort must be made to achieve more consistent fitting procedures. Partly by reducing the variance in the measured FRFs and partly through more insight into the effect of different initial values and boundaries, solver settings, and cost-functions on the final parameter values. Second, that the used model must be carefully considered with respect physiological reality. Adding a parameter that lacks physiological explanation may lead to inaccurate fitting results, as this parameter might yield incorrect values to align with the frequency response function (FRF). The choice to only allow 'excitory' stretch reflexes is in line with most literature on the stretch reflex, especially combined with the current task instruction. Therefore, the choice to use $k_v = 0$ as a lower bound can be considered sensible.

V

PSDs at low frequencies

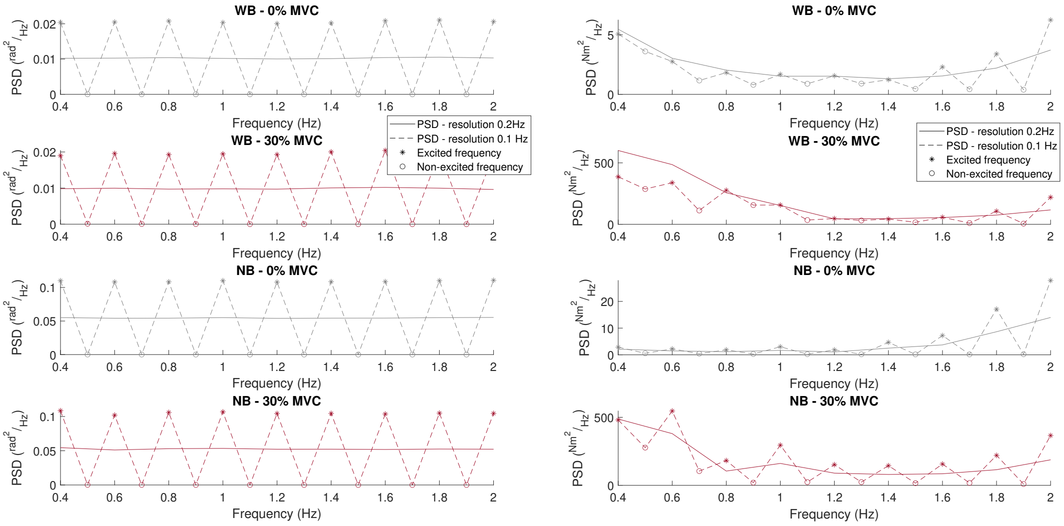

(a) PSD of joint angle at low frequencies at 2 different resolutions. **(b)** PSD of joint torque at low frequencies at 2 different resolutions.

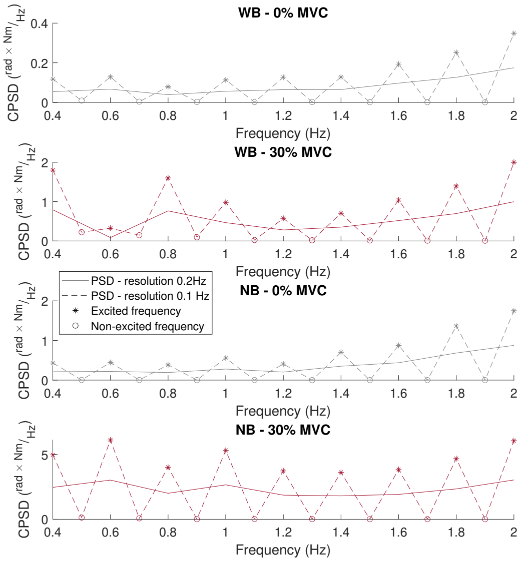

(c) Cross PSD of joint angle and torque at low frequencies at 2 different resolutions.

Figure V.1: (Cross) PSDs for joint angle and torque at low frequencies region $(0 - 2Hz)$.

The figure V.1 shows the (cross-)PSDs for the joint angle input and torque output signals at 2 resolutions, the one used for impedance estimation ($0.2Hz$ increments) and one of doubled resolution ($0.1Hz$ increments). Within these figures, an explanation for low coherence at low frequencies can be identified. First, figure V.1a shows a clean PSD for the joint angle. The $0.1\ Hz$ frequency resolution PSD shows no power at the unexcited frequencies in perturbation. Looking at figure V.1b, the difference between power at excited and not excited frequencies is small and inconsistent at the high resolution PSD. This indicates noise in the signal, at both the excited and unexcited frequencies in the perturbation. The increase of noise is clearly visible at lower frequencies and is higher at increased activation level. It is also relatively larger for the WB perturbation than the NB perturbation.

Looking at the cross-PSD which is used in impedance estimation, the noise at the unexcited frequencies is cancelled out, as the position signal does not contain power at those frequencies However, the noise is also present at the excited frequencies, resulting in some inconsistencies visible for the Cross PSD as well. This inconsistency is best seen at the WB 30% MVC trial, where at the lowest few frequencies the PSD appears almost random. This relatively large noise in the torque signal compared to actual torque output signal related to the perturbation, results in the low observed coherence at low frequencies.

W

Mathmatical coherence analysis

W.1. Open Loop coherence

Looking at the blockscheme in 2.3 depicting open loop system identification, the output T_{meas} as dependent on perturbation θ_{pert} and noise N can be derived in the frequency domain as follows:

$$T_{meas}(f) = H_{ELB}(f) \cdot \theta_{pert}(f) + N(f) \tag{W.1}$$

Using the definition of (cross-)power spectral density:

$$S_{xy} = E\{X(f) \cdot Y(-f)\}, \tag{W.2}$$

equation W.1 can be converted to a relation between PSDs through multiplication with the complex conjugate of the perturbation angle fourier transform, $\theta *_{pert} (-f)$:

$$S_{\theta T} = H_{ELB} \cdot S_{\theta\theta} + S_{\theta N}. \tag{W.3}$$

Similarly, multiplication with the complex conjugate $N * (-f)$ gives:

$$S_{TN} = H_{ELB} \cdot S_{\theta N} + S_{NN}. \tag{W.4}$$

and multiplication with $T *_{meas} (-f)$ gives:

$$S_{TT} = H_{ELB} \cdot S_{T\theta} + S_{TN}, \tag{W.5}$$

If the noise is assumed uncorrelated with the perturbation signal, $S_{\theta N} = S_{N\theta} = 0$. Substitution of equation W.3 and W.4 into equation W.5, then gives:

$$S_{TT} = H_{ELB}^2 \cdot S_{\theta\theta} + S_{NN}. \tag{W.6}$$

The coherence, calculated with the (cross-)PSDs of the input and output signal, then becomes:

$$\begin{aligned} \gamma^2 &= \frac{|S_{\theta T}|^2}{S_{\theta\theta} \cdot S_{TT}} \\ &= \frac{|H_{ELB} \cdot S_{\theta\theta}|^2}{(H_{ELB}^2 + S_{\theta\theta} + S_{NN}) \cdot S_{\theta\theta}} \\ &= \frac{1}{1 + \frac{S_{NN}}{|H_{ELB}|^2 S_{\theta\theta}^2}} \end{aligned} \tag{W.7}$$

This coherence is clearly dependent on H_{ELB}, with the limit of γ^2 going to zero if $|H_{ELB}|$ approaches 0.

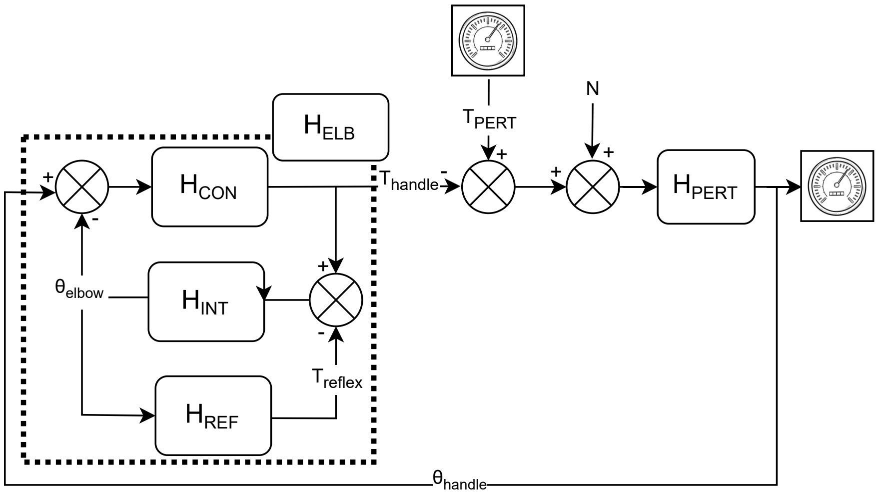

Figure W.1: Blockscheme of a Closed Loop System Identification (CL-SID) setup.

W.2. Closed Loop coherence

For the CL-SID blockscheme depicted in figure W.1, the measured output $\theta_{handle}(f)$ can be derived dependent on the input $T_{pert}(f)$ and noise $N(f)$:

$$\theta_{handle}(f) = H_{PERT}(f) \cdot T_{pert}(f) + H_{PERT}(f) \cdot N(f) - \theta_{handle}(f) \cdot H_{ELB}(f) \cdot H_{PERT}(f). \tag{W.8}$$

Similar multiplications can be performed as in the OL-SID coherence analysis, between equation W.8 and the complex conjugates: $N*(-f)$, $\theta*_{handle}(-f)$, and $T*_{pert}(-f)$. Again making use of the PSD definition W.2, results in three definitions for $S_{\theta\theta}$, $S_{T\theta}$, and $S_{N\theta}$.

$$\begin{aligned} S_{\theta\theta} &= H_{PERT} \cdot S_{\theta T} + H_{PERT} \cdot S_{\theta N} - S_{\theta\theta} \cdot H_{ELB} \cdot H_{PERT} \\ &= \frac{H_{PERT} \cdot S_{\theta T} + H_{PERT} \cdot S_{\theta N}}{1 + H_{ELB} \cdot H_{PERT}}, \end{aligned} \tag{W.9}$$

$$\begin{aligned} S_{T\theta} &= H_{PERT} \cdot S_{TT} + H_{PERT} \cdot S_{TN} - S_{T\theta} \cdot H_{ELB} \cdot H_{PERT} \\ &= \frac{H_{PERT} \cdot S_{TT} + H_{PERT} \cdot S_{TN}}{1 + H_{ELB} \cdot H_{PERT}}, \end{aligned} \tag{W.10}$$

and

$$\begin{aligned} S_{N\theta} &= H_{PERT} \cdot S_{NT} + H_{PERT} \cdot S_{NN} - S_{N\theta} \cdot H_{ELB} \cdot H_{PERT} \\ &= \frac{H_{PERT} \cdot S_{NT} + H_{PERT} \cdot S_{NN}}{1 + H_{ELB} \cdot H_{PERT}}. \end{aligned} \tag{W.11}$$

Again the perturbation ($T_{pert}(f)$ and noise ($N(f)$) can be assumed uncorrelated resulting in $S_{TN} = S_{NT} = 0$. Equation W.9, through substitution of equation W.11 and W.10, then becomes:

$$S_{\theta\theta} = \frac{H^2_{PERT} \cdot S_{TT} + H^2_{PERT} \cdot S_{NN}}{(1 + H_{ELB} \cdot H_{PERT})^2}. \tag{W.12}$$

Filling in $S_{T\theta}$ and $S_{\theta\theta}$ into the definition of coherence gives:

$$\begin{aligned}
\gamma^2 &= \frac{|S_{\theta T}|^2}{S_{\theta\theta} \cdot S_{TT}} \\
&= \frac{\left| \dfrac{H_{PERT} \cdot S_{TT}}{1 + H_{PERT} \cdot H_{ELB}} \right|^2}{\dfrac{H_{PERT}^2 \cdot S_{TT} + H_{PERT}^2 \cdot S_{NN}}{(1 + H_{ELB} \cdot H_{PERT})^2} \cdot S_{TT}} \\
&= \frac{H_{PERT}^2 \cdot S_{TT}^2}{H_{PERT}^2 \cdot S_{TT}^2 + H_{PERT}^2 \cdot S_{NN} \cdot S_{TT}} \\
&= \frac{S_{TT}}{S_{TT} + S_{NN}}
\end{aligned} \tag{W.13}$$

This coherence is independent of the arm impedance. Indirectly, the PSD of the torque disturbance S_{TT} is dependent on the total impedance of the arm and perturbator if the amplitude must remain limited during the experiments. However, if a flat power spectrum for S_{TT} is used, the low impedance at low frequencies does not directly cause a low coherence at those frequencies.

X

Data analysis for a 100s measurement

Figure X.1 shows the average impedance magnitude, phase, and coherence calculated for both 200 s and 100 s of data. Note that the 100 s of data is copied from the first half of the 200 s data. It is visible that all FRF and coherence estimates are very similar, with the exception of low-frequency phase for the 0% MVC trials and WB signal. At these low frequencies, the signal-to-noise ratio is low, causing larger need for adequate averaging to reduce the effect of noise on the PSDs. The phase is especially sensitive to noise, as with small imaginary or real parts of the FRF, a sign switch can occur quickly when noise is added, causing a 180-degree phase shift. As observed from figure X.2 the similarity in impedance functions is also seen in the fitted IR-model parameters. A similar trend can be observed when using the 100 s date, as when using the 200 s data.

However, when looking at individual participants, the differences increase. Table X.1 shows the average percentual deviation of the impedance magnitude, averaged across all frequencies and across all participants. As the magnitude differs largely per frequency, a choice was made to normalise the differences with respect to the absolute magnitude at that frequency. Table X.2 shows the average deviation in phase averaged over all frequencies and participants.

While differences impedance remain small, the effect on the fitted parameters is large. As fitting behavior remains unpredictable, small deviations in impedance magnitude or phase can cause large deviations in fitted parameters per individual. Tables X.3, X.4, and X.5 show large percentual deviations when assessing the absolute difference between the 100 s and 200 s analysis per participant and then averaging these. It must be noted that these percentages quickly attain high values if the original parameter fit was close to 0, as is the case for most 0% MVC trials. However, it is apparent that while the overall average effects are not highly influenced by changing the measurement time, the individual fits are.

Table X.1: Average percentual differences between magnitude of joint impedance for the 100 s and 200 s analysis.

	0% MVC	10% MVC	30% MVC
WB	7.3%	11.4%	11.1%
NB	4.4%	10%	12.5%
WB LP	4.8%	11.8%	14.5%

Table X.2: Average differences between phase of joint impedance for the 100 s and 200 s analysis.

	0% MVC	10% MVC	30% MVC
WB	8.0	7.7	7.7
NB	2.6	6.6	6.0
WB LP	4.6	6.4	11.2

Table X.3: Averaged percentual differences between fitted intrinsic stiffness for the 100 s and 200 s measurement.

	0% MVC	10% MVC	30% MVC
WB	70.8%	29.4%	23.2%
NB	7.3%	8.5%	11.2%
WB LP	25.3%	15.8%	27.3%

Table X.4: Averaged percentual differences between fitted intrinsic stiffness for the 100 s and 200 s measurement.

	0% MVC	10% MVC	30% MVC
WB	61.9%	25.1%	14.4%
NB	41.4%	23.8%	14.8%
WB LP	58.1%	36.2%	29.1%

Table X.5: Averaged percentual differences between fitted reflex gain for the 100 s and 200 s measurement.

	0% MVC	10% MVC	30% MVC
WB	54.1%	47.2%	50.3%
NB	48.7%	37.8%	28.6%
WB LP	56.7%	42.1%	28.7%

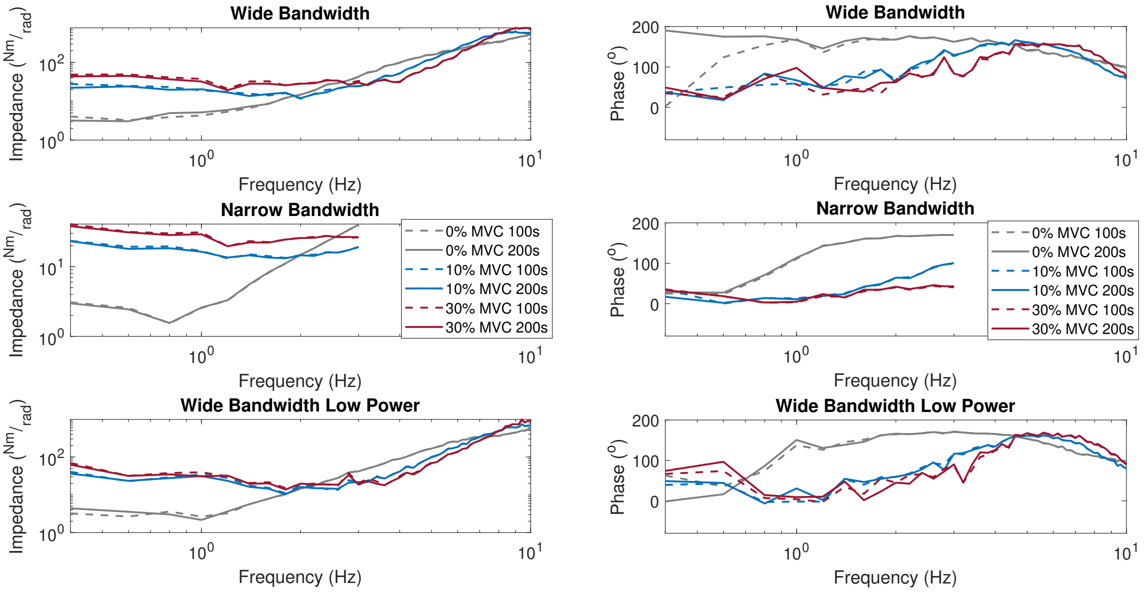

(a) Average magnitude.

(b) Average phase.

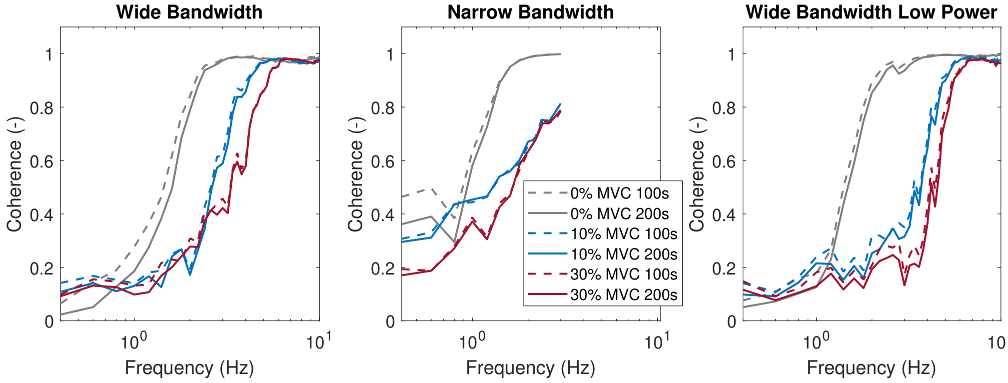

(c) Average coherence.

Figure X.1: Average impedance magnitude, phase, and coherence for different signals at different activation levels, comparing a 100 s and 200 s analysis.

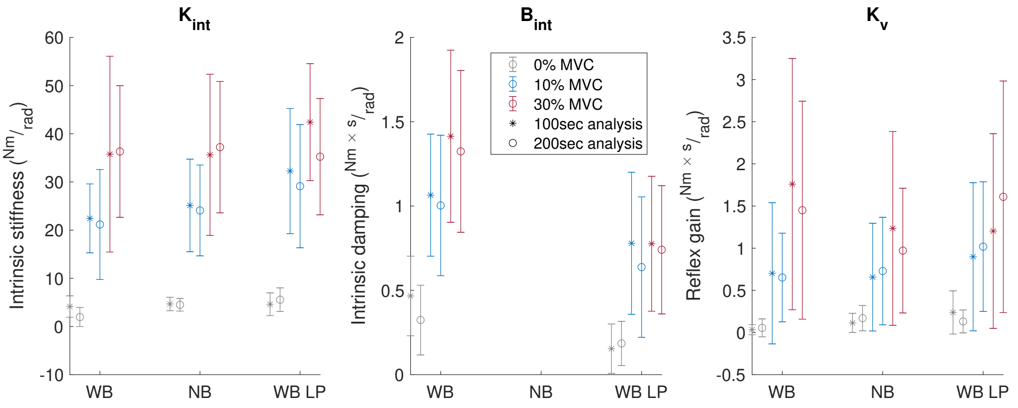

Figure X.2: Average fitted IR-model parameters for the 100 s and 200 s analysis.